University of Nevada, Reno

Machine Learning Techniques Applied to the Nevada

Geothermal Play Fairway Analysis

A thesis submitted in partial fulfillment of the requirements for

the degree of Master of Science in Geophysics

by

Connor Macrossie Smith

Dr. James E. Faulds/Thesis Advisor

August 2021

N

We recommend that the dissertation
prepared under our supervision by

entitled

be accepted in partial fulfillment of the
requirements for the degree of

Advisor

Committee Member

Committee Member

Committee Member

Graduate School Representative

David W. Zeh, Ph.D., Dean
Graduate School

Abstract

This study introduces machine learning techniques to the Nevada geothermal play

fairway analysis (PFA), which provided geothermal potential maps for 96,000 km^2 of

west-central to eastern Nevada. The motivation for this project is to support the

evaluation of geothermal resource potential and the exploration for undiscovered blind

geothermal systems in the Great Basin region of Nevada. The previous PFA study

succeeded in utilizing the weighted combination of various geologic, geophysical, and

geochemical features, indicative of permeability and heat, to both generate detailed

geothermal favorability maps and identify several new blind geothermal systems.

However, the project faced key limitations and challenges, including robust statistical

analyses for the estimation of weights of influence for individual parameters, some

incomplete datasets, and a limited number of training sites.

To mitigate these challenges, this study incorporates new data developments and

innovative machine learning techniques. Data developments include new training data

and translating both the play fairway datasets (original and enhanced) and newly

available datasets into a form compatible with machine learning techniques. Following

the evaluation of various supervised and unsupervised machine learning techniques with

the available data, two primary approaches were selected based on their performance and

functionality. These techniques include 1) supervised probabilistic Bayesian artificial

neural networks to produce detailed geothermal potential maps with confidence intervals,

and 2) unsupervised principal component analysis paired with k-means clustering to both

identify spatial patterns in geologic and geophysical feature sets and create new combined feature inputs.

The comparative analyses of two principal sets of geological and geophysical input features highlight the potential that machine learning techniques offer to improve on the PFA. The analysis of feature set one, which comprises a set of regional permeability and heat data, illustrates a promising design for supervised Bayesian neural networks modeling to improve on the original regional permeability modeling in the PFA. Results from this feature set are selected to organize spatial patterns for the major structural-hydrologic domains within the study area, including the Walker Lane, western Great Basin, central Nevada seismic belt, and carbonate aquifer. The analysis of feature set two, which includes the same regional feature layers as in feature set one with the addition of local permeability features, illustrates how a model design may find a balance between disparate data types to produce predictive favorability maps that yield similar results to the original fairway map from the PFA. Information presented in this study related to the spatial patterns of elevated geothermal potential may have promising implications for future geothermal exploration efforts in the Great Basin region of Nevada and beyond.

Acknowledgments

Table of Contents

List of Tables

List of Figures

Chapter I. Introduction

Geothermal energy is a relatively untapped clean and sustainable resource derived from the heat of the Earth. The Great Basin region of western North America is a world class geothermal province with more than 1,200 MWe of installed capacity from ~28 power plants (B. Ayling, personal communication, 2021). However, studies indicate far greater potential for both conventional hydrothermal and enhanced geothermal (EGS) systems in the region (e.g., Williams et al., 2009).

Historically, most conventional hydrothermal geothermal systems have been discovered and developed through drilling in the vicinity of surficial geothermal features (e.g., fumaroles, hot springs, paleo-geothermal deposits) or accidentally by developers seeking fossil fuel, mineral, or water resources. Today, the primary limiting factor for further geothermal development of conventional hydrothermal systems is the blind nature of many of these resources. Most geothermal systems in the Great Basin are controlled by Quaternary normal faults and generally reside near the margins of actively subsiding basins. Geothermal fluids commonly up-well along basin-bounding faults, flow into permeable subsurface sediments in the basin, and thus do not always daylight directly along faults. Thermal springs may emanate many kilometers away from the deeper source, or thermal groundwater may remain hidden with no surface manifestations (Richards and Blackwell, 2002). Blind systems are thought to comprise most geothermal resources in the Great Basin region (Coolbaugh et al., 2007). Thus, techniques are needed

both to identify the structural settings that allow geothermal systems to form (e.g., Curewitz and Karson, 1997; Faulds et al., 2006; Faulds and Hinz, 2015) and to determine which areas may harbor subsurface hydrothermal fluid flow.

The geothermal play fairway analysis (PFA) exploration concept, adapted from the petroleum industry (Doust, 2010), involves the integration of geologic, geophysical, and geochemical parameters indicative of geothermal activity to identify the most likely locations for significant geothermal fluid flow (i.e., play fairways) (e.g., Faulds et al., 2015, 2016; Shervais et al., 2016; Forson et al.,2016; Lautze et al., 2017; Siler et al., 2017; Wannamaker et al., 2017; Craig, 2018; McConville et al., 2017). This includes the evaluation of the relative favorability of known, undeveloped geothermal systems, as well as assessing the probability of a particular area for hosting undiscovered blind systems.

A PFA of a large part of Nevada leveraged logistic regression, weights of evidence, and other statistical measures as a type of machine learning (ML) technique (Faulds et al., 2015). A set of features, each gauged by a perceived weight of influence, were combined to estimate geothermal potential and succeeded in both generating detailed geothermal favorability maps, as well as in identifying several new blind geothermal systems (Faulds et al., 2018, 2019; Craig, 2018). However, the project faced key limitations and challenges, including robust statistical analyses for the estimation of weights of influence for individual parameters, some incomplete datasets, and a limited number of training sites. In this thesis, new data development efforts and innovative ML

algorithms are incorporated to mitigate key challenges and enhance the PFA methodology (e.g., Faulds et al., 2020a; Brown et al., 2020; Smith et al., 2021).

During the data development stage of this project, efforts focused on maximizing an inventory of training data samples and preparing datasets for compatibility with machine learning techniques. The initial modeling efforts focused mainly on a supervised problem of classifying geothermal favorability, whereby Bayesian artificial neural network modeling showed significant promise (e.g., Blundell et al., 2015). However, due to the inherent complexity and biases in the data and the problem of classifying geothermal favorability, the need to perform an unsupervised exploratory data analysis by leveraging dimensionality reduction methods combined with cluster analysis became clear. In particular, principal component analysis (e.g., Wold et al., 1987) is employed together with k-means clustering (e.g., Hartigan and Wong., 1979). This method was selected due to its capacity to parameterize complex feature and label relationships in reduced dimensions. Furthermore, principal component analysis offers the opportunity to evaluate generating new reduced input features for the supervised modeling efforts.

This thesis presents the major outcomes of new data developments and the application of machine learning modeling with two prioritized feature sets. Results include favorability maps from Bayesian artificial neural network modeling and cluster plots and maps from principal component analysis combined with k-means clustering. Finally, a comparative analysis of each of these techniques demonstrates their promise in guiding future practical assessments of new geothermal prospects.

1.1 Great Basin Geothermal Systems

Globally, most geothermal systems are associated with magmatism and located in magmatic arcs, rifts, or hotspots, whereas volcanism within the Great Basin region of the western USA largely ceased between 10 and 3 Ma (Christiansen and McKee, 1978). Except for a few magmatic geothermal systems along the western and eastern margins (e.g., Coso, Long Valley, and Roosevelt), geothermal systems in the Great Basin region are amagmatic and thus lack a mid to upper crustal magmatic heat source (Faulds et al., 2019). Instead, regional extension has significantly thinned the crust and lithosphere and induced a relatively high geothermal gradient throughout the Great Basin (Blackwell et al., 2010). These factors make the Great Basin as one of the largest geothermal provinces on Earth, significantly larger than geothermal provinces in Iceland, New Zealand, and western Turkey combined, with a regional potential that may exceed 30,000 MWe (Faulds et al., 2010).

Permeability in many geothermal systems around the world is structurally controlled, with faults and interconnected networks of faults and fractures serving as pathways for circulating fluids (e.g., Curewitz and Karson, 1997; Rowland and Sibson 2004; Faulds et al. 2006, 2011). A survey of the ~ 450 known geothermal systems in the extensional and transtensional domains of the Great Basin region has shown that a handful of specific structural geometries (Figure 1.1) control the location of geothermal upwelling in nearly all systems (Faulds et al. 2006, 2011; Jolie et al. 2021). Most Great Basin geothermal systems, especially those ≥130°C, reside in normal fault terminations, fault intersections, step-overs in normal fault systems, and extensional accommodation

zones, as opposed to the main fault segments (e.g., Curewitz and Karson, 1997; Faulds et al., 2006; Faulds and Hinz, 2015). Fault architectures that characterize these structural settings are commonly manifested in the surface topography as 1) major steps in range-front faults (step-overs); 2) interbasinal highs (accommodation zones); 3) mountain ranges consisting of relatively low, discontinuous ridges (horsetail fault terminations and accommodation zones); and 4) lateral terminations of mountain ranges (horsetail fault terminations) (Faulds et al., 2006, 2011).
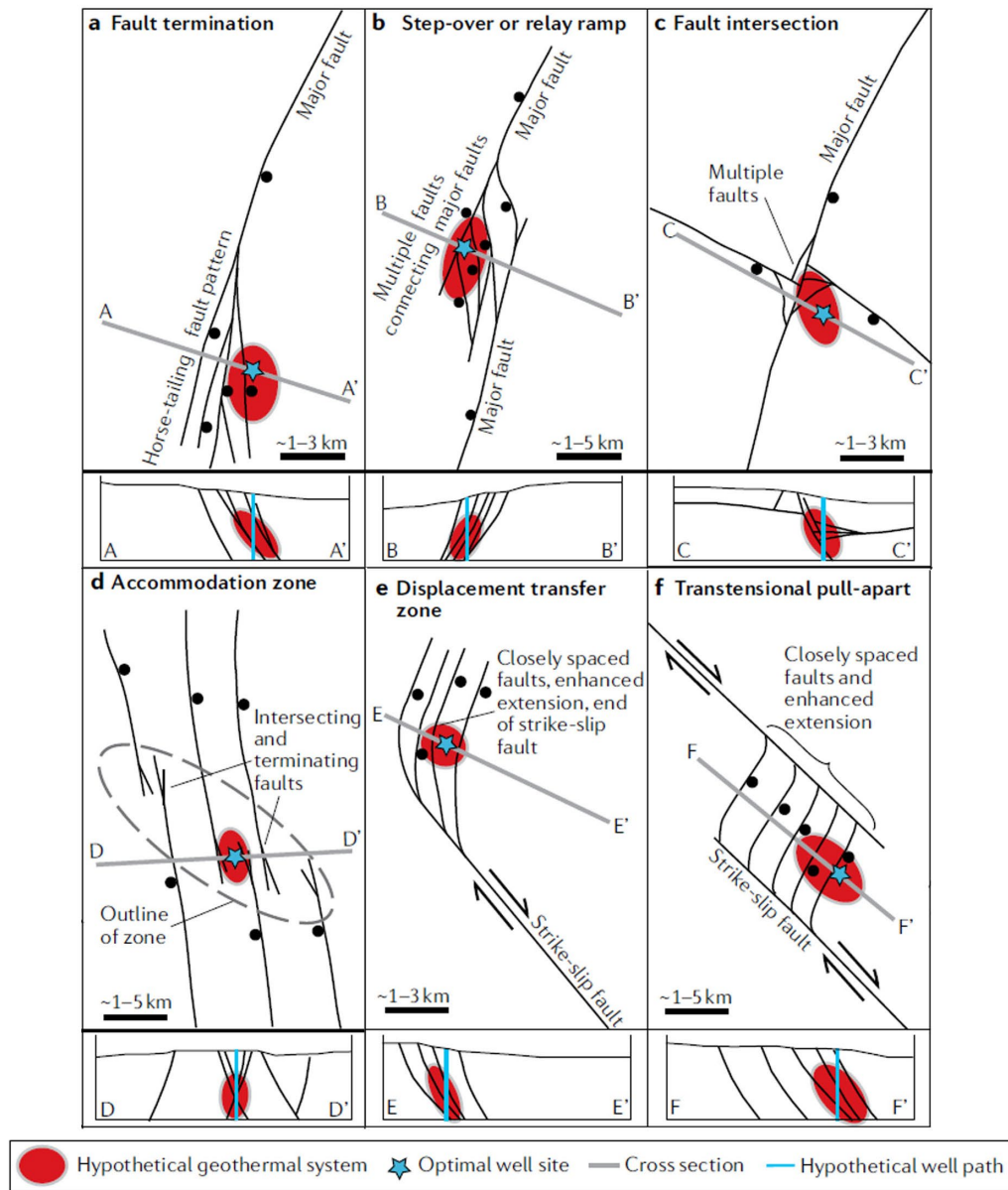
Figure 1.1. *Characteristic structural settings for geothermal systems in the Nevada Great Basin region. Red shaded areas mark approximate locations of hypothetical geothermal upwellings in map view and in cross section. Blue stars and lines illustrate hypothetical optimal well sites and well paths, respectively. Double arrows indicate the orientation of the maximum horizontal stress. Structures a-d host nearly 90% of the known geothermal systems in the Nevada Great Basin region (Modified from Jolie et al., 2021).*

Identification of these settings provides a method for guiding geothermal exploration. Additionally, the combination of multiple favorable structural settings at a single locality has been shown to be a significant control for the known higher-temperature systems of the region (Faulds et al., 2013). However, relevant geological and geophysical features are also required to identify undiscovered favorable structural settings and determine which structures have the highest potential for hosting geothermal plays.

1.2 The Nevada PFA

The Nevada PFA was applied across a broad swath (~96,000 km^2) of the Great Basin region, extending from west-central to eastern Nevada and included ~86 active known geothermal systems and ~10 geologic, geophysical, and geochemical features that factor into assessing geothermal favorability (Faulds et al., 2017). The Nevada PFA workflow (Figure 1.2) involved a mixture of numerical, categorical, and ordinal feature values, each tied to geographic positions in the study area with varying degrees of resolution. The primary product of the regional analysis is the fairway model (Figure 1.3), which provides dynamic predictions over multiple scales (local, intermediate, and regional) and is very target rich, with numerous favorable locations identified in a variety of settings through the study area. Construction of the predictive fairway model utilized sets of features from four key geologic factors applicable to geothermal exploration: 1) local permeability; 2) intermediate permeability 3) regional permeability; and 4) heat. Features incorporated into local permeability are ascribed to ~375 structural setting ellipses inside

the study area based on the type of structure, certainty and quality of the structure, Quaternary slip rates, age of Quaternary faulting (recency), and slip and dilation tendency. The location of Quaternary faults comprised intermediate permeability. Regional permeability included earthquake distribution, age of Quaternary faults, slip rates on Quaternary faults, geodetic strain rate, and horizontal gravity gradient. Heat was represented by the inferred temperatures at 3 km depth.

The linking of parameters was performed by multiplying each by a unique weight, then combining the weighted parameters into a linear summation. The weights used in the workflow were derived using a combination of statistics, including 1) Bayesian-based weights-of-evidence and logistic regression (red numbers in Figure 1.2) through the analysis of 34 benchmark sites of known, relatively high temperature geothermal systems (≥130°C) in the study area, and 2) expert judgment (black numbers in Figure 1.2) due to known limitations of some datasets and small number of training sites. The workflow also integrated direct evidence of heat from wells and geothermometers to delineate an overall favorability model, as well as degree of exploration features to develop an exploration opportunities model.

The PFA phase 1 report (Faulds et al., 2015a) describes, among other things, the selection of benchmarks and workflow of analyzing each dataset from data input, initial data set modeling (e.g., interpolation), statistical evaluation against benchmarks, selection of weighting values for the play fairway model, and error analysis. Data and results from the three phases of the project are readily accessible in the public domain through the Geothermal Data Repository (GDR, Geothermal Data Repository (openei.org)) or

Nevada Bureau of Mines and Geology archives (NBMG,

http://nbmg.unr.edu/Geothermal).
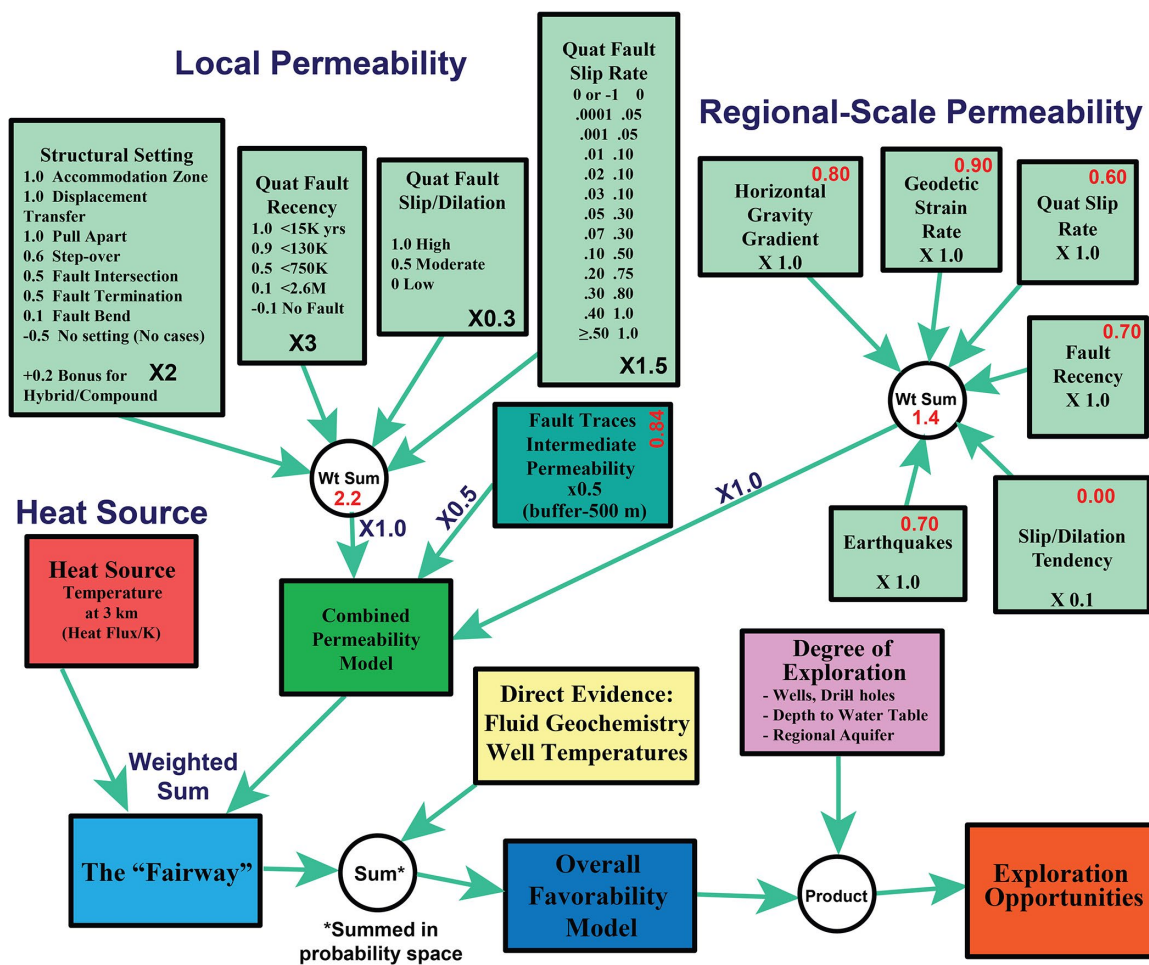
Figure 1.2. *The Nevada PFA workflow. Note the mixture of numerical (regional-scale permeability) and categorical/ordinal features (intermediate and local permeability), each tied to geographic positions on a map with varying scales of resolution (modified from Faulds et al., 2017). Red numbers indicate relative weights determined from weights of evidence. Black numbers indicate expert driven weights used in the analysis.*
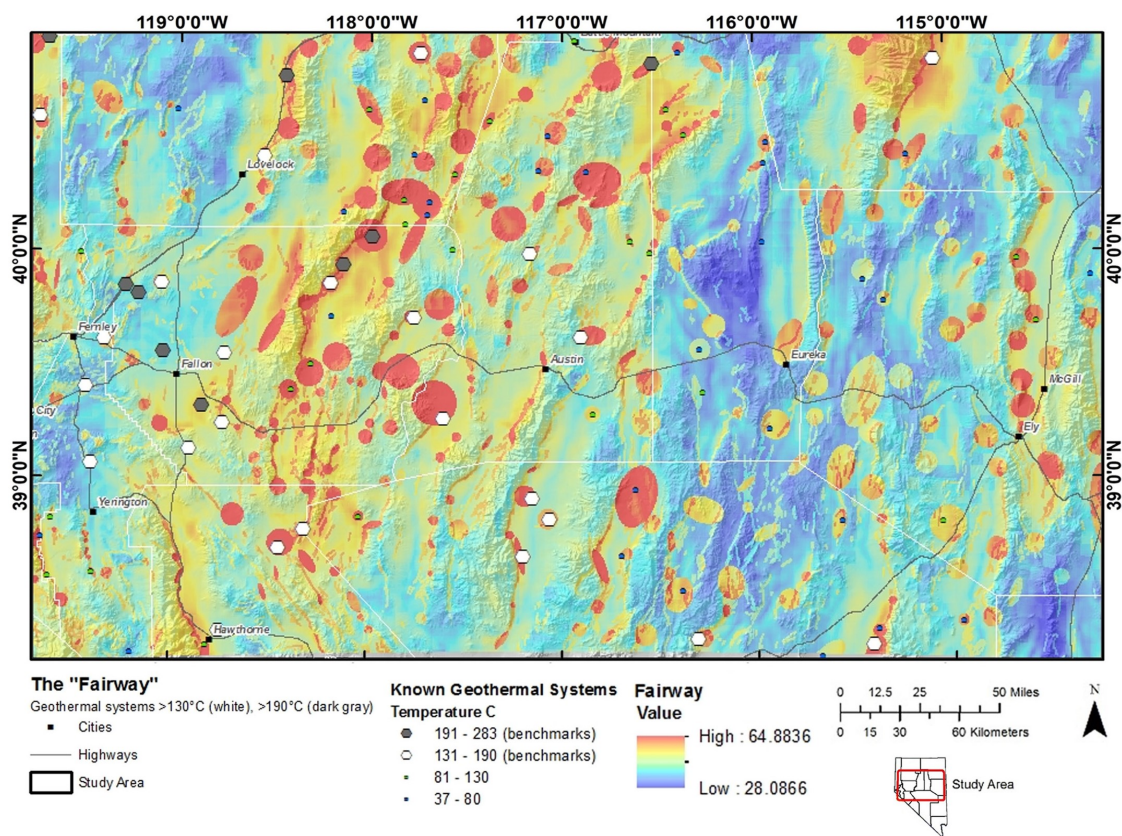
Figure 1.3. *The play fairway favorability model. Plotted within the study area are fairway prediction values (not normalized) ranging from a low ~28 to a high of ~ 65. Known geothermal systems comprising 34 relatively high-temperature (>130°C) benchmarks are shown in dark gray and white hexagons (modified from Faulds et al., 2017).*

Notably, the Nevada play fairway study area spans a regional strain gradient, a range of crystalline to carbonate basement lithologies, and multiple structural-hydrologic domains (Faulds et al., 2015a, 2015b). From east to west in the Nevada PFA study area, major domains include the Walker Lane, western Great Basin, central Nevada seismic belt, and carbonate aquifer (Figure 1.4). The Walker Lane is a northwest-trending belt of largely transtensional dextral shear (Stewart, 1988; Faulds and Henry, 2008) that

accommodates ~20% of the right-lateral motion between the Pacific and North American plates (Dixon et al., 1995, 2000; Hammond et al., 2009; Kreemer et al., 2012). This domain hosts the highest strain rates in the study area, a higher density of earthquakes, and noticeably lower fault slip and dilation tendency relative to the rest of the study area. The central Nevada seismic belt is a north-northeast trending region of high crustal strain rates marked by strong historical earthquakes (e.g., Caskey et al., 2004). Along with high magnitude earthquake and strain signals, this domain hosts many faults with relatively recent offsets. The western Great Basin domain consists of two sub regions to the west and east of the central Nevada seismic belt and hosts relatively moderate to high strain rates of crustal extension with some dextral transtensional motion and high slip and dilation tendency values. The eastern part of the study area is dominated by a regionally extensive carbonate aquifer, a relatively cool and deep aquifer system that occupies most of the eastern Great Basin (Brooks et al., 2014). Crustal strain recorded in geodetic studies in this area is generally significantly less compared to the western Great Basin (Hammond et al., 2009). Within the carbonate aquifer domain, there are notable areas of recent faulting in the north half, and relatively high earthquake density and low to moderate heatflow in the south. Additionally, most of this region is at a higher average elevation than the western domains.
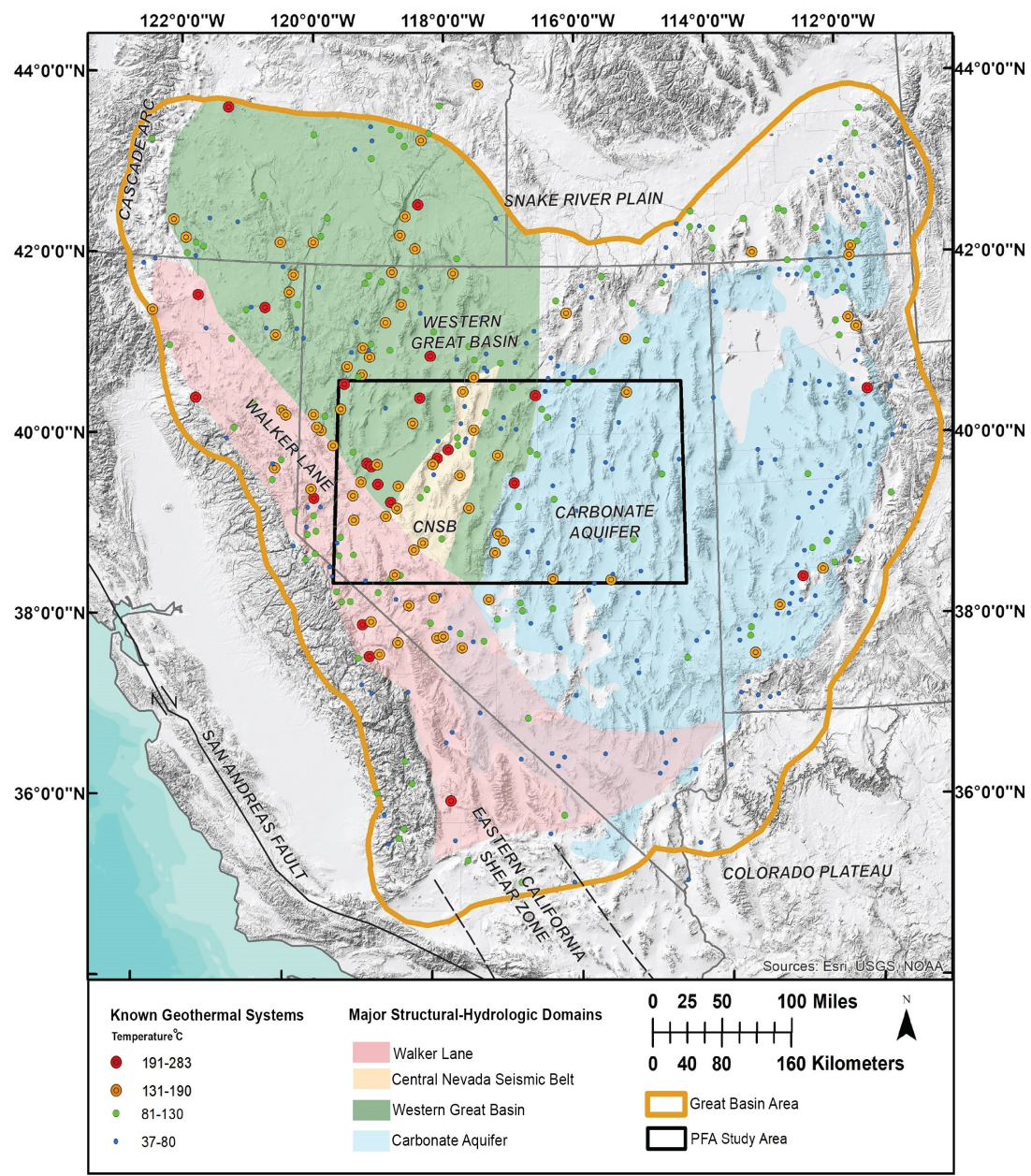
Figure 1.4. *Map of high-temperature geothermal systems of the Great Basin region and major structural-hydrologic domains. The Great Basin region is outlined in orange with active known geothermal systems displayed as circles (red >191˚C, orange 131-191˚C, green 81-130˚C, blue 37-80˚C). The play fairway study area is shown in the black rectangular outline.*

1.3 Machine Learning Efforts

Machine learning is a field of artificial intelligence (AI) that studies computer algorithms that improve automatically through experience (Mitchell, 1997). Over the last decade, machine learning has become an essential tool in data science, engineering, medical research, and most applied sciences. In Earth science machine learning techniques have been applied to earthquake detection (Perol et al., 2018), geologic mapping (Cracknell and Reading, 2014), mineral prospecting (Rodriguez-Galiano et al., 2015), and many other applications that require observations, commonly spatially registered to geographic coordinates, and making inferences about an unknown or unseen characteristic. Such observations may include predicting a numerical quantity or probability, recognizing a particular structure or category, or to build a new classification or taxonomy.

This thesis explores a joint evaluation of supervised and unsupervised machine learning algorithms to improve on the Nevada PFA. Supervised learning involves training a model for predictive tasks through an appropriate learning algorithm that is optimized to associate pairs of measurable features and labels by providing it with many examples. With unsupervised learning, no training examples are used, instead, an algorithm is given a set of data and tasked with evaluating feature patterns and relationships. This study utilized 1) supervised learning techniques for classification of geothermal favorability mapping, where an algorithm is provided a set of examples, such that geological and geophysical features are known to be either associated or not associated (i.e., positive or negative labels) with a viable geothermal system; and 2) unsupervised learning techniques for exploratory data analysis, where a dimensionality reduction algorithm is

able to reduce large matrices of geologic and geophysical input features into new simpler

representations, such that hidden structures in the data are readily identified, and the

reduced data may easily be clustered (Table 1).

Table 1. Principal learning techniques introduced in this study.

Learning Method	Task	Algorithm	Application
Unsupervised	Dimensionality Reduction	Principal Component Analysis (PCA)	Exploratory Data Analysis
	Clustering	K-Means	
Supervised	Classification	Artificial Neural Network (ANN)	Predictive Modeling
	Regression		

Addressing the supervised modeling problem builds on recent advances with

artificial neural networks (ANN), including either fully-connected or convolutional deep

neural networks (e.g., Goodfellow et al., 2018). However, with unsupervised modeling

inspiration is drawn from similar studies (Lindsey et al., 2018; Pepin 2019; Vesselinov et

al., 2020), which utilized dimensionality reduction methods paired with clustering

algorithms to characterize signatures of permeability and heat at known geothermal

systems.

Introducing these methods first involves evaluating model designs to select

approaches that best fit the data. These efforts focus on finding a balance between

feeding large numbers of geologic and geophysical features into a machine learning

model and letting the model determine the relations versus engineering the complete

hypothesis and algorithm by hand. The former, while unbiased and allowing data to guide

results, can be prone to over-fitting where a model effectively memorizing labeled

training data and is prone to a reduction in the capability for generalizing a solution with

unlabeled data. The latter runs the risk of extreme bias, leading to underfitting such that

important links among features may not be recognized. Also, the algorithms developed in

the hand-engineered approach may not be appropriate for new data types or to new

realms of application. Where possible, it is best to identify a suitable balance and move

toward 'big data' machine learning applications to accommodate the growing assemblage

of geoscience data. However, this requires addressing key data challenges (listed below)

inherent to the Nevada play fairway study.

> A small number and potential imbalance of training examples: Although
known geothermal systems occur in large well documented trends, the spatial
extent of the ~34 benchmark sites used for statistical weight derivations in the
PFA accounts for less than 1% of the study area and represents a relatively
small training set. Additionally, many supervised learning techniques require
a balanced inventory of positive and negative training samples. Small
numbers of samples and imbalanced data can lead to over-fitting. Any training
set should be comprehensive enough to include characteristics seen in all
relevant data outside the training set. If a supervised model can accurately
predict *out of sample* training data, the model is well generalized.

➢ Variable data types and heterogenous distributions: Input features carrying important information represent a mixture of numerical values (real numbers such as heatflow or horizontal gravity gradient) and categorical variables (e.g., structural setting type). The easiest to understand are continuous numerical features, whereas categorical feature need to be replaced by a numbering scheme to be effectively integrated, because both the supervised and unsupervised machine learning techniques being applied are fundamentally algebraic computations. Finally, datasets may not have the same resolution nor the same degree of certainty, and missing data should be attributed by procedures such as averaging nearby points, inserting a constant, or filling with an appropriate random sample distribution.

➢ Complex feature and label relationships: Given the variety in the multi-sensor data, the expected structure in each input feature layer differs greatly. Yet, it is the co-occurrence of a number of these structures that commonly indicates geothermal favorability (i.e., a low magnetic anomaly on its own can be meaningless, but when associated with a favorable structural setting and gravity gradient signature, these multiple lines of direct and indirect evidence suggest the presence of a potential drilling target). It is best to develop models based on the physical relationships between geological/geophysical features and labels of favorability. Furthermore, the "black-box" nature and relative absence of geological knowledge in data-driven applications undermines the reliability of predictive results (Karpatne et al., 2018). That is why

incorporating such "expert" knowledge into the hypotheses is important, especially to counter having a small number of examples to optimize a supervised model and in ensuring proper integration and weighting of large feature set matrices.

A major focus throughout this study has been on properly adapting the machine learning techniques to mitigate these data issues. These efforts (discussed below) include data development and a comparative analysis of various modeling designs and data inputs.

1.4 Contributions

My thesis research was part of a large multi-disciplinary and multi-institutional project focused on applying machine learning techniques to identifying hidden geothermal systems in the Great Basin region. As such, it involved contributions from many team members. During the data development and machine learning modeling stages of this project, major contributions were provided by fellow project members from the United States Geological Survey (USGS), Massachusetts Institute of Technology (MIT), Hi-Q Geophysics, and Great Basin Center for Geothermal Energy (GBCGE) in the Nevada Bureau of Mines and Geology at the University of Nevada, Reno. Data compilation in ArcGIS largely involved efforts from members of the USGS (Jacob DeAngelo, Drew Siler, and Eric Burns), as well as members of the Great Basin Center for Geothermal Energy (Bridget Ayling, Elijah Mlawsky, and Mark Coolbaugh). Data translation efforts

in Python and ArcGIS were made by the USGS group and Stephen Brown with MIT. Training site development in ArcGIS was a major focus of my research and relied on key insights from Mark Coolbaugh and James Faulds of the Great Basin Center for Geothermal Energy. During machine learning modeling efforts, developing and applying supervised learning techniques in Python using TensorFlow, Keras, and PyTorch relied primarily on efforts from the MIT group (Stephen Brown, Michael Fehler, and Chen Gu), myself, and the Hi-Q Geophysics group (John Queen and Sven Treitel). Developing and applying unsupervised learning techniques in Python using Scikit Learn was initiated by Stephen Brown and John Queen and later became a major focus of my research. Stephen Brown, John Queen, Sven Treitel, and many other project members provided key insights for the unsupervised learning efforts. Finally, synthesizing the major tasks of the project and performing a comparative analysis of the results was a key task of my thesis research, which benefited directly from discussions with our entire project group, quarterly reports, and papers from my collaborators (Faulds et al., 2020a, Brown et al., 2020).

Chapter II. Methods

This chapter provides background information on data development, supervised learning with artificial neural networks, and unsupervised learning based on dimensionality reduction paired with cluster analysis.

2.1 Data Development

Datasets considered in this study (Table 2) include the original and recently refined features from the PFA study, as well as several new datasets. Some of these data are numerical (such as density), and others are categorical (such as type). The numerical features are represented as continuous real numbers known at 1,728,000 grid points with 250-m spacing. These include all six geophysical features, as well as elevation, slip and dilation tendency, and heatflow. Categorical features (Quaternary fault locations, local permeability features, fluid geochemistry, and paleo-geothermal features) may be binary (e.g., Quaternary fault locations represented as binary 1or 0 features), ordinal (e.g., local permeability features assigned a number by the experts ranking their perceived importance), or nominal (ignoring numerical values and looking at variable types, e.g., paleo-geothermal feature types). In order to use these disparate data types effectively together in a machine learning algorithm, it is best to place them on an equal footing numerically by either preprocessing or other manipulations. For this study, categorical features are converted to continuous numerical representations by converting the space around a feature (e.g., fault) to a distance (Figure 2.1), or a density representation by using a Gaussian filter (Figure 2.2).

Table 2. Datasets considered in the study. Thirteen geologic feature layers and six geophysical layers are included.

Geological Features	Geophysical Features

Location, age, and slip rates of Quaternary faults	Earthquake density
Local Permeability features within structural ellipses (Favorable structural setting type, Local Quaternary fault recency, Local Quaternary fault slip/dilation tendency)	Geodetic strain rate
*Slip and dilation tendency constrained by regional stress	*Horizontal gravity gradient
**Heat flow (replacing Temperature at 3 km depth)	**Horizontal gravity gradient max spot density
*Fluid geochemistry – Geothermometry	**Horizontal magnetic gradient
**Paleo-geothermal features (sinter, travertine, and tufa deposits)	**Horizontal magnetic gradient max spot density
**Elevation (DEM with 30-meter spatial resolution)	

*Refined dataset   **New dataset

QuaternaryFault-Traces → QuaternaryFault-Distance
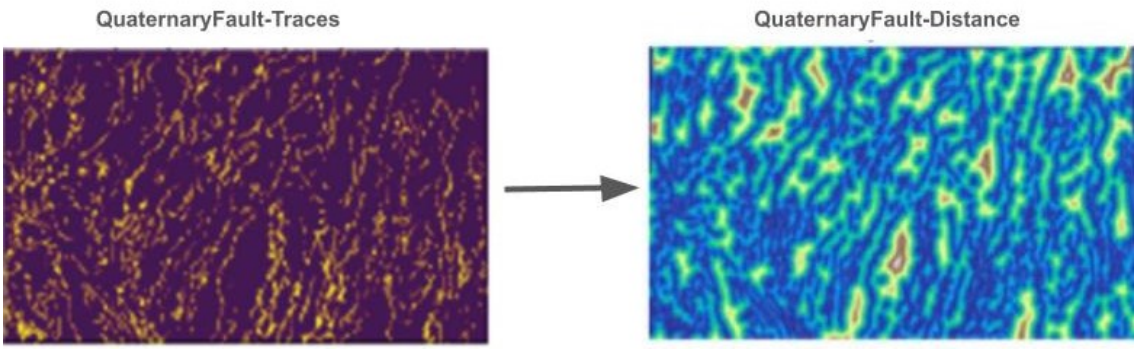
Figure 2.1. *Example of the conversion of a categorical feature to a continuous numerical feature by distance. The fault trace map on the left is a categorical feature representing a matrix of 1's and 0's where 1's overlay the location of identified Quaternary fault traces. These fault traces can be transformed to a continuous numerical feature by calculating the Manhattan distance to the nearest fault shown on the right.*
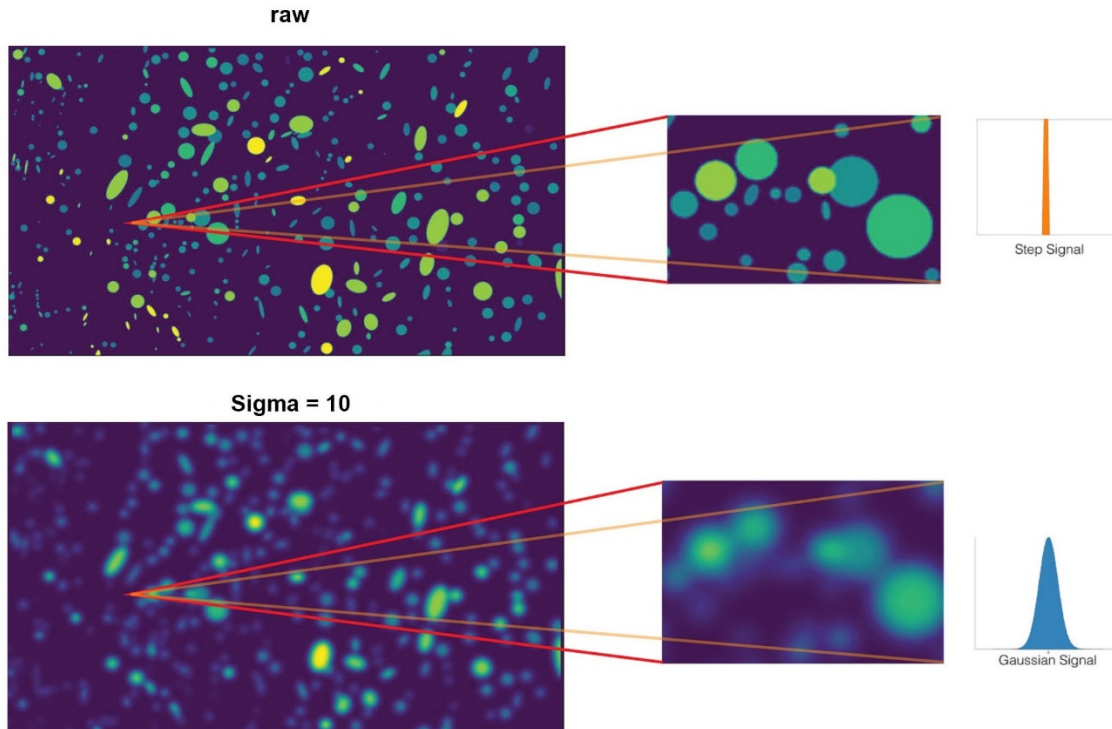
Figure 2.2. *Example of the conversion of a categorical feature to a continuous numerical feature by density. The map on top shows structural setting types, where categories are labeled only within the ellipses. These categories have been given a value representing significance by experts as a numerical scale. These structural settings can be transformed to a continuous numerical feature by calculating their density as shown on the bottom (using a Gaussian filter with sigma =10). This transformation creates a new representation for each ellipse, from a signal a few pixels wide (top) to a probability distribution signal (bottom).*

Considerable effort went into understanding the influence of each dataset. Of all the categorical data examined, local permeability factors were the most relevant. Local

permeability was used as the highest weighted feature set in terms of predicting

geothermal favorability in the original play fairway analysis. A key issue with including

local permeability is that the numerical assignment of these features is labeled only

within ellipses, and these values impart an expert bias on the solution. This study

explored circumventing this bias by introducing a distance transformation to the center of

a structure, but a challenge identified with this transformation is that it devalues the area

between neighboring structures. Thus, numerical assignments of local permeability

factors were included using a density transformation (as seen in Figure 2.2).

Alongside numerical transformations, the values of each input feature are

standardized to allow comparison between strongly contrasting magnitudes using the

standard score scaler transformation:

$$z = \frac{x - \bar{x}}{s_x} \tag{1}$$

where x is the feature to be transformed, $\bar{x}$ is the sample mean, s_x is the sample standard

deviation, and z is the transformed feature. The standard score scaler transforms any

sample distribution to a corresponding feature with a mean of zero and a standard

deviation of one, while retaining rank information.

Modeling efforts experimented with various sets of features and transformations

for both categorical and numerical data types. In total 20 data layers were selected and

are divided into four major groups (Figure 2.3): 1) a base set composed of numerical

geologic and geophysical features pertaining to intermediate and regional permeability,

as well as heat; 2) gravity and magnetic alternates of the horizontal gradient (2A), and the

horizontal gradient with a weighted kernel density function using a 4 km radius on points of maximum gradient (2B); 3) local permeability alternates of features with density transformations (3A), and the distance from the center of a structural setting (3B); and 4) geochemistry data of paleo-geothermal deposits and geochemistry temperature values. These groups are then organized into different feature sets to evaluate the results of different feature combinations in model performance and behavior. Following detailed analyses with various feature combinations, two principal feature sets (Table 3) were

selected for a comparative analysis below.

GROUP 1: BASE SET

Q-Fault Distance | Geodetic Strain Rate | Q-Fault Slip Rate | Q-Fault Recency

Earthquakes | Q-Fault Slip & Dilation Tendency | Heatflow | DEM-30m

GROUP 2: GRAVITY AND MAGNETIC ALTERNATES

Horizontal Gravity Gradient | Horizontal Magnetic Gradient

HGG- Density | HMG- Density

2A) HORIZONTAL GRADIENT

2B) HORIZONTAL GRADIENT MAXSPOT DENSITY

GROUP 3: LOCAL PERMEABILITY ALTERNATES

Local Structrual Setting | Local Q-Fault Recency

Local Q-Fault Slip & Dilation Tendency | Local Q-Fault Slip Rate

Favorable Structural Setting Distance

3B) DISTANCE TO LOCAL CENTER

3A) LOCAL DENSITY

GROUP 4: GEOCHEMISTRY

Silica Sinter Distance | Tufa or Travertine Distance | Geochemistry Temperature

Figure 2.3. Color contoured map groups of features used in this study. Warmer colors represent higher numerical values. Maps are divided into groups, which are distributed into different feature sets (Table 3).

Table 3. Feature sets explored in the study.

Set 1	Set 2
➢ Group 1: Base Set ➢ Group 2A: Horizontal Gradient	➢ Group 1: Base Set ➢ Group 2A: Horizontal Gradient ➢ Group 3A: Local Density

2.1.1 Training Sites

For optimal benefits, machine learning techniques commonly employ a much larger number of training data than the 34 benchmark sites used in the initial PFA study. Additionally, many supervised learning techniques require a balanced inventory of positive and negative training samples. Small numbers of samples and imbalanced data can lead to over-fitting and a corresponding reduction in the capability for generalization (i.e., the ability to accurately predict the labels of datasets not used in the training process).

In this study training data were maximized from the regional data inventory (Figure 2.4). Training data include 83 positive sites from known geothermal systems

(≥39°C) and 62 negative sites from relatively deep and cool wells (mostly from oil and gas exploration, available from the Nevada Bureau of Mines and Geology oil and gas well database (Nevada Bureau of Mines and Geology (unr.edu); Hess et al., 2011). Appendix A includes metadata for both positive and negative training sites. Using a broader temperature range (≥39°C), additional positive geothermal sites became available. In the case of negative sites, criteria were established to select from a relatively large number (>250) of relatively deep (>1 km) oil and gas wells in the region that have temperature gradients less than the regional average.

In the criteria for negative sites, the distribution and depth of the carbonate aquifer (Brooks et al., 2014) in eastern Nevada was reviewed for its possible impact of masking geothermal anomalies. In the Great Basin and several other geothermal provinces (e.g., western Turkey), aquifers may capture and entrain rising thermal fluids before they reach the surface. This may explain why the western domains of the play fairway study area host a greater percentage (61%) of known geothermal systems, because the water table is less likely to be influenced by a regionally extensive and relatively cool aquifer in the upper levels as compared to the carbonate aquifer in eastern Nevada (Koenig and McNitt., 1983; Coolbaugh et al., 2002). Based on the inferred influence of the carbonate aquifer, temperature gradients were assessed for wells that exceed 2 km in depth in the eastern part of the study area, whereas wells deeper than 1 km were evaluated outside the carbonate aquifer. The temperature assigned to a well was compared to the predicted temperature at the bottom of the well based on the regional heat flow and temperature gradient map used for the play fairway analysis (Faulds et al., 2017). If the regional

predicted temperature was greater than or equal to the measured temperature (i.e., no temperature anomaly), the well was considered as a potential negative training site.

Next, a de-clustering algorithm was developed to reduce the number of possible negative training sites in areas with a high-density of drilled holes. This de-clustering was based on the condition that no two wells selected as negative training sites could be closer than 5 km to each other, or closer than 5 km to a positive training site. This distance was based on the broad analogies with negative training site distributions and the apparent size of geothermal reservoirs at developed systems. It was found that the distribution of such sites was not too complicated, such that it was possible to determine the optimal selection of sites in a reproducible manner from careful visual inspection. Finally, a detailed quality review of positive and negative sites was completed, checking that the spatial location and attributes corresponded to each training site.
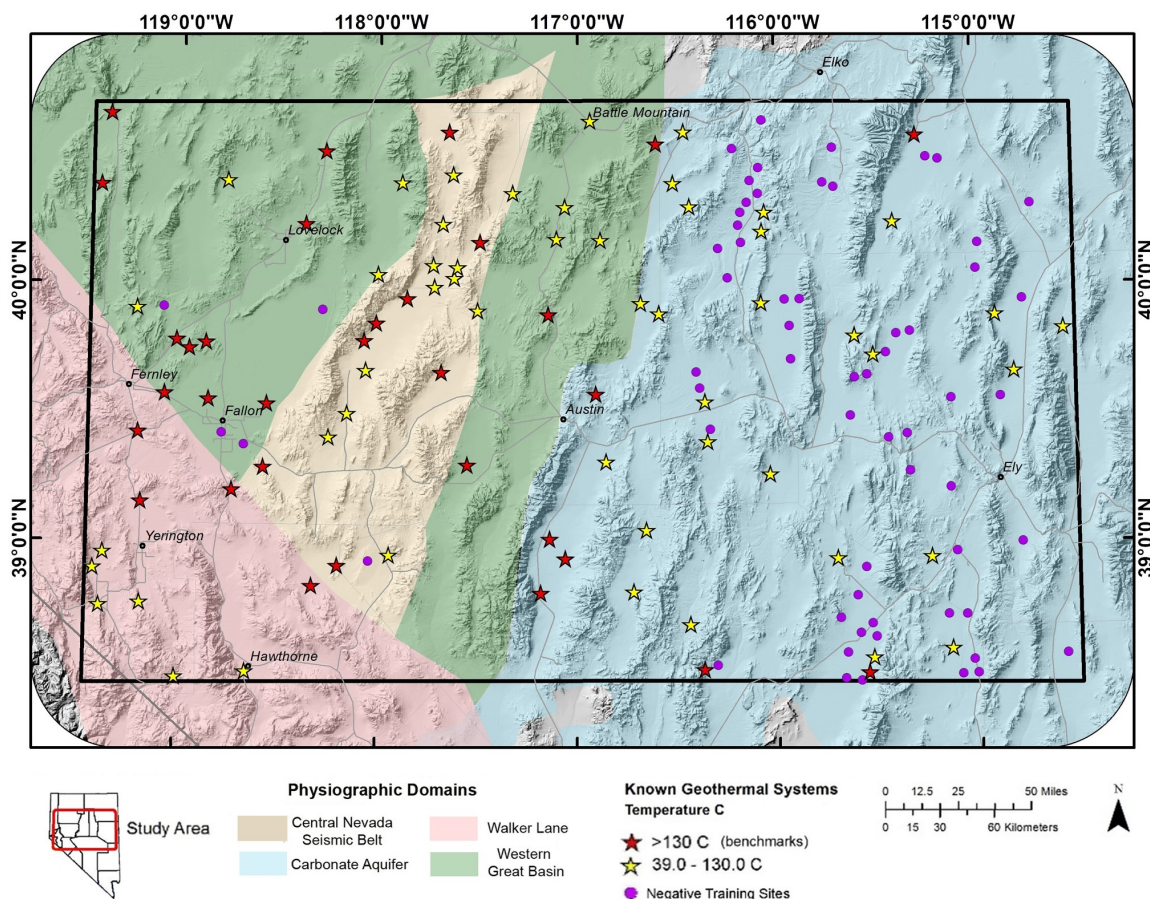
Figure 2.4. *Distribution of positive (red and yellow stars) and negative (purple circles) training sites and major domains. Positive sites labeled as red stars have a maximum temperatures >130°C and yellow stars have temperatures between 39-130°C. Note, training site metadata is provided in Appendix A.*

Given the extent of the study area, the population of training sites represents a relatively high spatial density compared to most geothermal provinces around the world. From a machine learning perspective, the addition of a larger training dataset enables a broader understanding of physical controls for geothermal favorability and improves the capability for model generalization. However, this training set accounts for less than 1%

of the surface area of the PFA study area and still represents a small population in terms of most data driven approaches. To address this, the real positive and negative training sites are augmented by including neighboring grid points as training samples in the supervised modeling.

2.2 Supervised Modeling

By revisiting the PFA workflow from a machine learning perspective, it can be viewed as type of feed-forward neural network, where linear combinations of feature weights are linked through linear "activations" to the next layer in the computation (Figure 2.5). This network goes directly from the measured features on the left through the series of algebraic calculations, without any loops, as it moves toward the resulting fairway value on the right. Also, by relaxing expert constraints built into the model, it represents a fully-connected artificial neural network (ANN), and this opens the opportunity to explore how best to set the balance between sources of information in the PFA workflow (i.e., between letting the data speak for themselves and inserting expert knowledge).
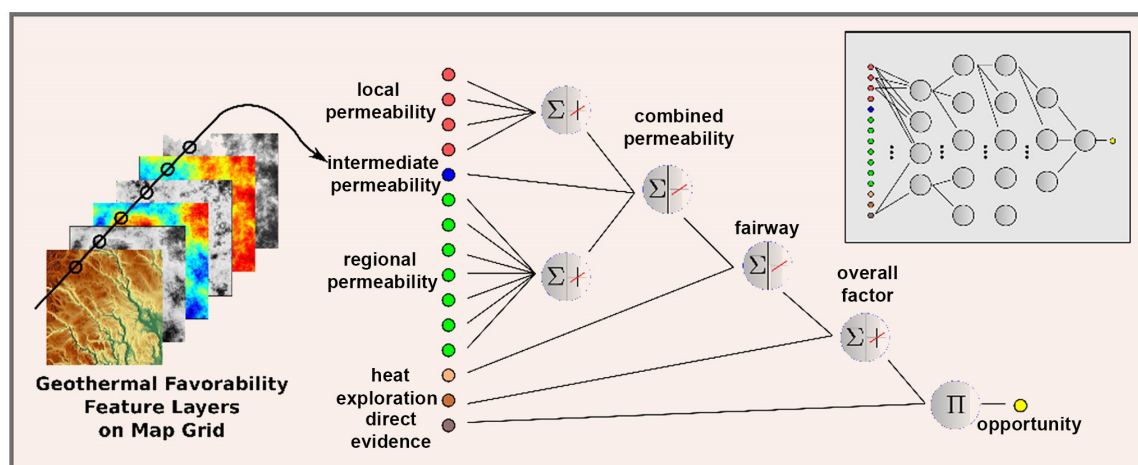
Figure 2.5. *The PFA workflow redrawn as a fully connected neural network. The top right corner shows a schematic of a fully connected neural network configured to take the PFA features as inputs on the left and infer the geothermal resource potential as a probability on the right (from Brown et al., 2020).*

Refining the original PFA workflow into a supervised machine learning approach, in particular as an ANN, has some key advantages. First, the outcome can be cast as a probability, defensible through validation tests. Second, careful implementation can reduce or eliminate biases in the choices of the most appropriate features and in the choices of the network architecture controlling how the features are combined. Finally, the algorithms can be easily automated, generalized, refined, and extended to accommodate new data sources (Brown et al., 2020).

2.2.1 Artificial Neural Networks

Artificial neural networks (ANNs) are modeled after the interpretation of biological neurons in the brain, where a neuron fires if the total input signal exceeds some weighted

threshold (Goodfellow, 2018). ANNs commonly map input data to a predictive output

layer by a concatenated sequence of matrix vector multiplication and nonlinear

thresholding with activation functions (Figure 2.6).
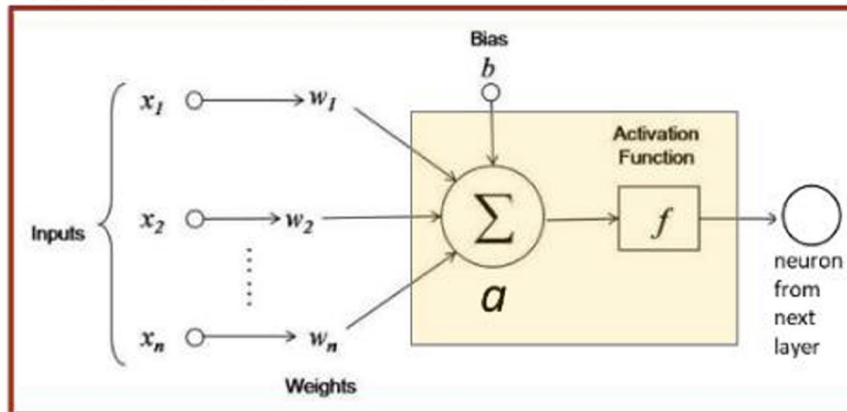
$$a = f(Wx + b)$$

a: activation value
W: weight matrix
x: input/data vector
b: bias term
f: activation function
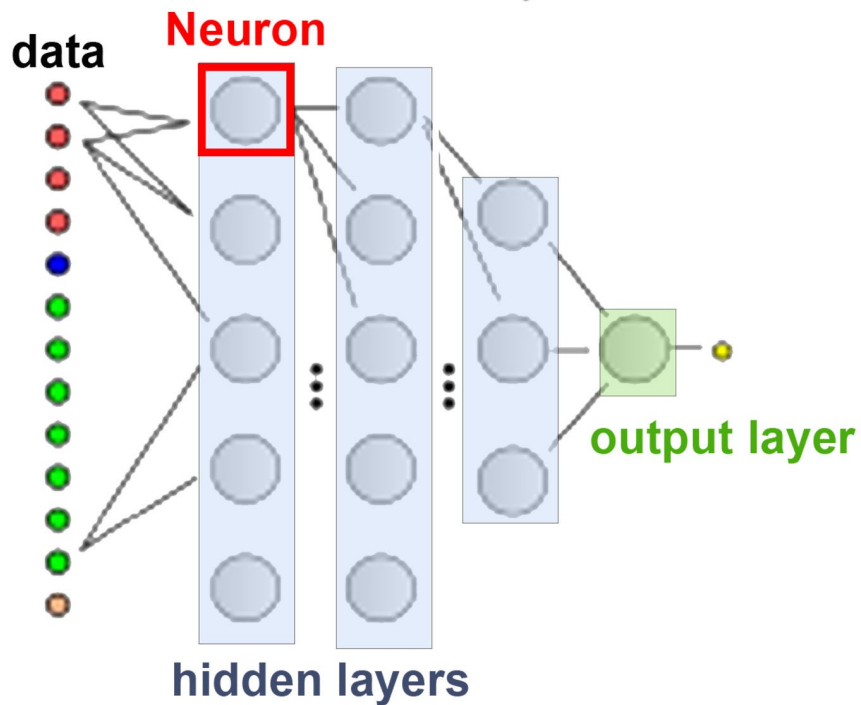
Figure 2.6. *Schematic of a fully connected artificial neural network model. Each hidden layer in the network contains multiple neurons. Lines connecting each of the neurons to the next layer represent weights. Each neuron in hidden layers is interconnected with all*

the neurons in the previous and following layers (modified from Nurindrawati and Sun., 2019).

Activation functions (Figure 2.7) within artificial neurons are the key component of the learning process because of their ability to account for non-linear relationships between input data. Activation functions are applied to the weighted sums of input data plus a bias term. A common activation function is the ReLU function, which transforms the negative values of the weighted sums and bias to 0.
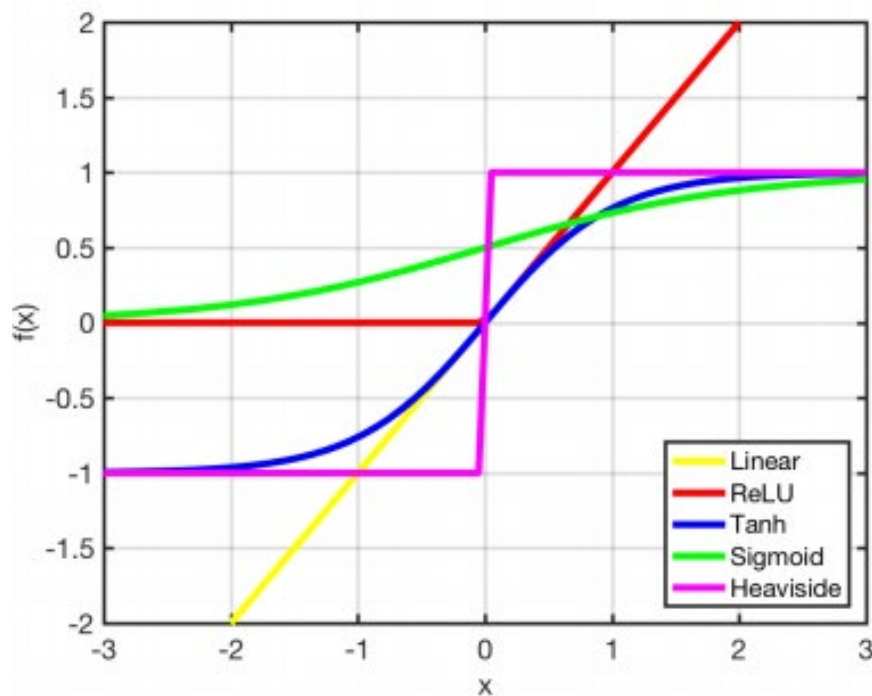
Figure 2.7. *Examples of different activation functions commonly used in neural networks. In this plot, the x axis is the weighted sum, and the y axis is the transformed activation value f(x) (from Granek, 2016).*

ANNs can be trained to optimize sets of weights and bias terms in an iterative scheme, with gradient based optimizers that look to solve an objective loss function (e.g., binary cross-entropy) based on the error rate obtained in previous iterations. The workflow for optimizing and applying ANNs and other supervised learning techniques can be broken into the development and application stage (Figure 2.8). During the development stage, cross validation is used to assess and optimize model performance. Cross validation commonly involves breaking up the labeled input data into sets for training/validation (~70%) and testing (~30%). Labeled training data are used to define 1) an initial fit of model weights; 2) validation data to tune hyperparameters (a parameter whose value is used to control the learning process); and 3) unlabeled testing data to provide an unbiased evaluation of the final model fit and performance.
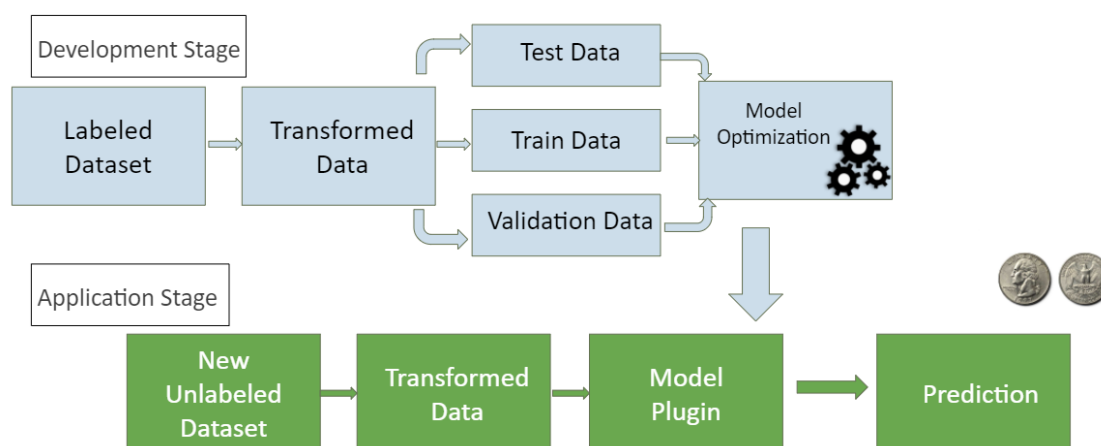
Figure 2.8. *Generalized workflow of a supervised learning model.*

The selection of an optimization algorithm, activation functions, learning rate, number of iterations, and other architectural aspects of ANNs can result in varying

degrees of performance. Thus, it is good practice to explore various approaches to identify an optimal ANN model. This study explores a hierarchy of different ANN model approaches, moving from the original PFA workflow to more complex and generally fully connected neural networks (Figure 2.9).
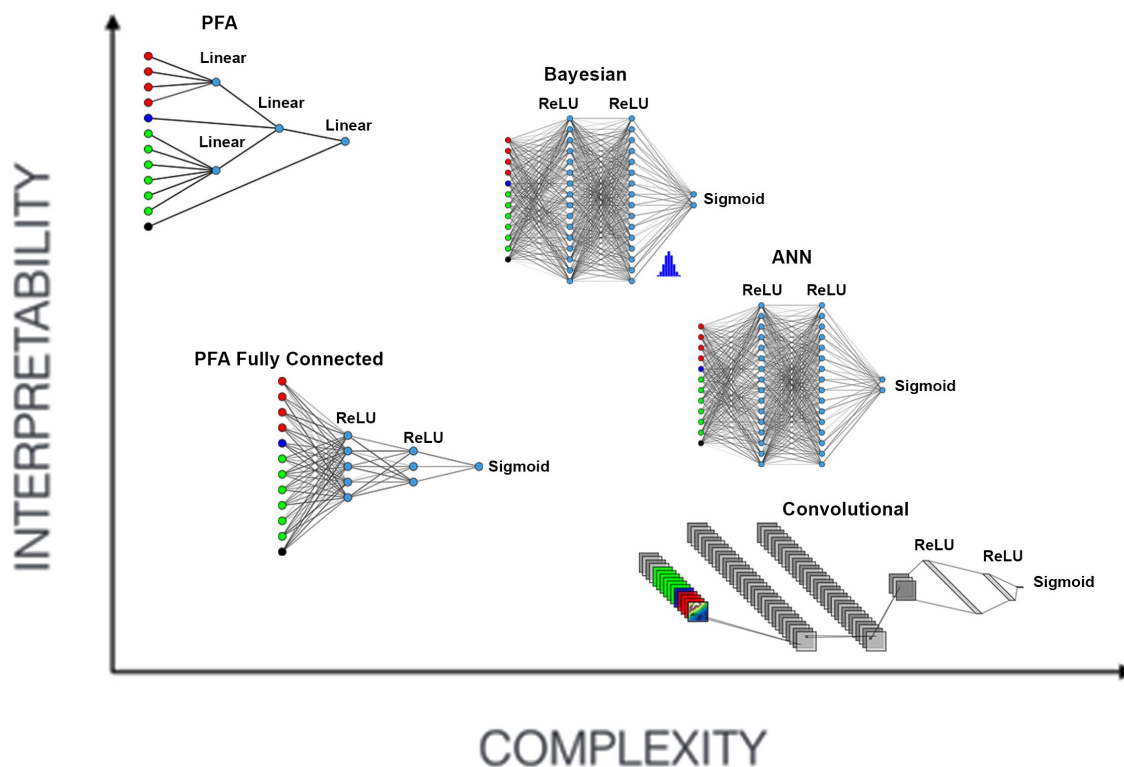
Figure 2.9. *Generalized complexity versus interpretability plot of PFA neural networks. Activation function utilized in the hidden and output layers are labeled for each network type.*

Probabilistic Bayesian neural networks (BNN) were selected as the optimal method for supervised modeling efforts based on performance and interpretability relative to the ANNs that were explored. This is termed the Bayesian neural network,

because it uses the algorithm Bayes by backprop (Blundell et al., 2015) to optimize the parameters of the probability distribution for each weight (e.g., mean and standard deviation) instead of a single weight value (Figure 2.10). The weights for a forward run can then be sampled from these distributions.

This becomes Bayesian when the cost component (Kullback-Leibler distance) is imposed, whereby the solution is penalized by how much it deviates from the prior idea of weight distributions (S. Brown, personal communication, 2021). Bayesian methods work to update prior interpretations (*priors*) based on new evidence (new data examples). The updates are balanced by weight regularization constants that are also integrated into the training process. Instead of training a single network, this method trains an ensemble of networks, where each network has its weights drawn from a shared, learnt probability distribution. By setting an optimal regularization term and informative *prior* for the distribution of samples, the BNN design avoids potential overfitting. The learned uncertainty in weights improves the generalization capacity of the model and interpretability of the results relative to the other ANN designs explored in this study. Once the ensemble of networks is trained, a distribution of predictions for each grid point in the study area can be produced with a well-defined most-likely value along with confidence bounds. Additionally, the method helps accelerate the systematic studies of the benefits or consequences of including features used in the original PFA workflow, as well as new features.
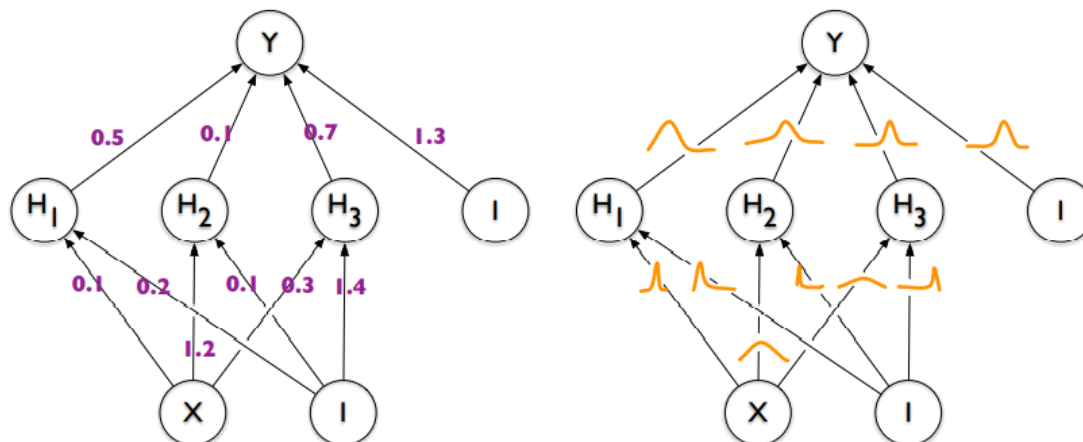
Figure 2.10. Bayes by backprop example. Left: each weight in a network has a fixed value, as provided by classic back propagation. Right: each weight in a network is assigned a distribution, as provided by Bayes by backprop (from Blundell et al., 2015).

Although there is a great deal of promise in the Bayesian approach, this model and the other ANNs utilize complex operations within hidden layers to parse and analyze the data. This procedure presents a 'black box' aspect to the derivations of feature weights and prediction outcomes. Even with a network design that performs well, the relationship between input data and output results are, for the most part, mathematically untraceable or too computationally expensive to derive.

2.3 Unsupervised Dimensionality Reduction and Clustering

Addressing the inherent complexity of the supervised learning problem prompted the application of unsupervised techniques for exploratory data analysis. Conventional unsupervised learning applications are commonly used to perform two major tasks,

clustering and dimensionality reduction. Clustering algorithms commonly use various

distance or dissimilarity measures to group and visualize data in ≥ three dimensions. In

the case of 'big data' problems (e.g., Goodfellow, 2018), data sparseness increases and

the efficacy of conventional clustering decreases as the number of dimensions increases.

This issue is commonly known as the curse of dimensionality (e.g., Hastie et al., 2001),

and methods are commonly utilized to apply a 'simpler' representation of multivariate

data. This study demonstrates a promising unsupervised method based on dimensionality

reduction with principal component analysis (PCA) coupled with k-means clustering

(PCAk), whereby PCA is first performed and then followed with k-means clustering.

There are several key advantages with PCAk. First, the reduction of PCA offers

promising results for isolating the sources of variance (variance being how far each value

lies from the mean) in the data. Second, the PCA reduction pairs well with k-means

clustering to visualize and organize grouped representations of the data. Finally, the

reduced feature signals from PCA can be evaluated as new combinations of geologic and

geophysical features.

With PCA, principal components (PCs) are found by solving an

eigenvalue/eigenvector problem from the combination of a scale part (eigenvalues) and

directional part (eigenvectors) of the covariance matrix of a dataset. This is illustrated in

an example looking at the PCA reduction of two well-correlated features introduced in

this study (Figure 2.12), earthquakes and geodetic strain rate. PCs are ordered by the

proportion of variance that they account for in the dataset (i.e., PC1 explains the largest

proportion of variance, PC2 the second largest, and so on). The measurement locations

along each PC axis are organized into parts of a mixing matrix (W), and the eigenvalues

or variable loading scores (found using the characteristic equation in Figure 2.12, step 4)

are organized into a feature matrix (H). Each of the PCs are constrained to be

orthonormal (unit length = 1) in W and orthogonal to each other in H, thus allowing a

distributed representation. In the example below, PCA reduction performs well with two

highly correlated features, but this operation may not fully represent the variance of

combined features that have non-linear relationships, and is further challenged with data

in higher dimensions.
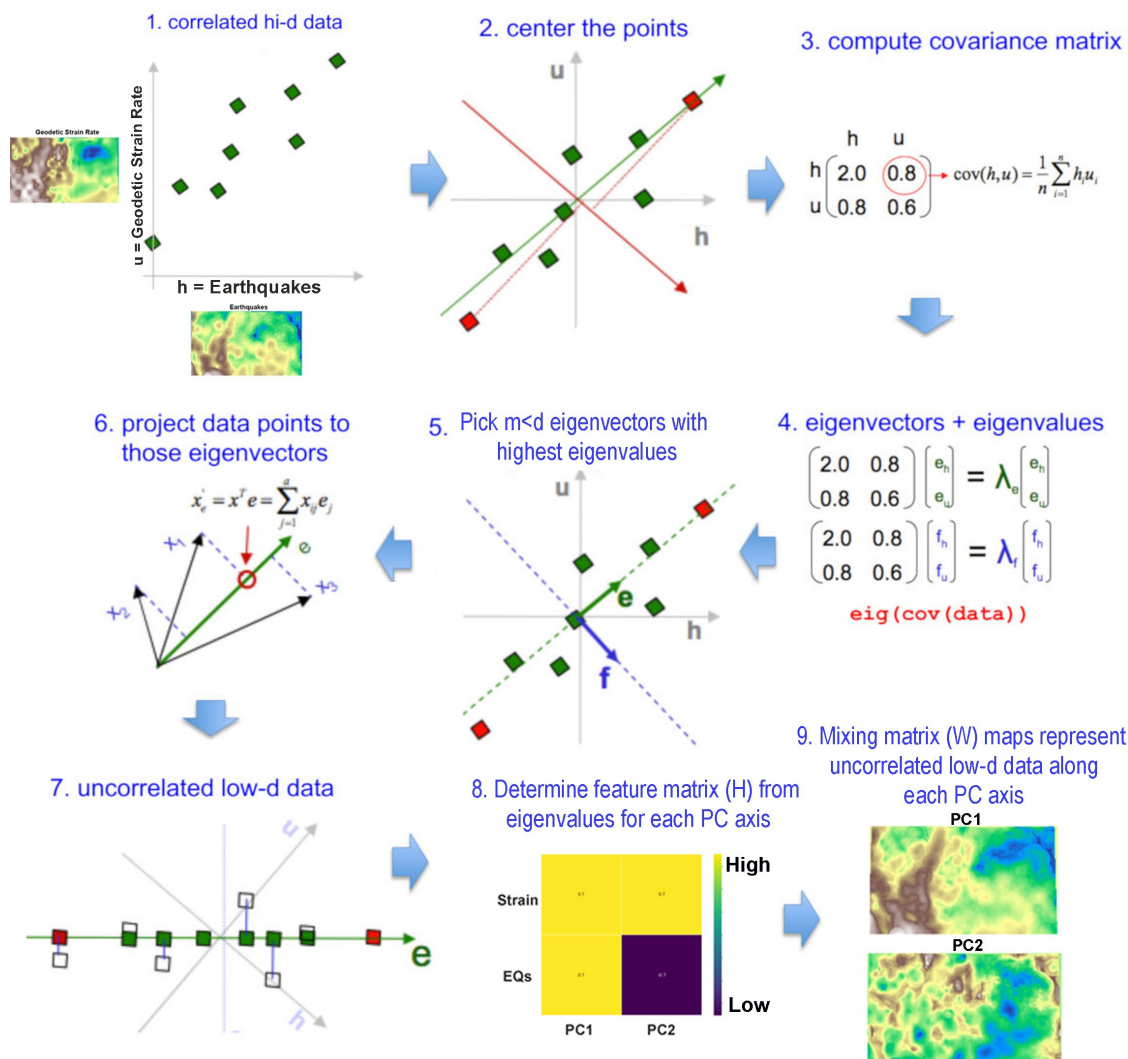
Figure 2.12. *Example PCA workflow. In this example, the maps for geodetic strain rate (u) and earthquakes (h) are plotted against one another and centered with respect to the mean. The covariance matrix between the two features is found and characteristic equation is introduced to determine eigenvectors and eigenvalues. Principal components (PCs) represent the orthogonal eigenvectors (e and f) and data points are projected onto each eigenvector. Data points along each eigenvector/PC represent new uncorrelated reconstructions of the data. For each eigenvector/PC there are loading values in the feature matrix (H) and new representation of the data along each eigenvector/PC axes in the mixing matrix (W). Here, the feature matrix (H) indicates that PC1 map appears directly correlated to both earthquakes and strain, and the PC2 map appears directly correlated to strain, but inversely correlated to earthquakes.*

The number of PCs are restricted to be less than or equal to the number of variables or measurements (whichever is greater) but are commonly truncated to produce a more generalized solution of multidimensional data (e.g., Cichocki, et al., 2009) with a lower degree of data sparseness to support clustering. K-means clustering was identified as a suitable method, which randomly initializes centroid locations and iteratively refines these locations until it finds an optimal centroid for each cluster group. The centroid position represents the arithmetic mean of the measurements that are in a spherical or elliptical cluster. This method requires the user to select the number of desired clusters.

Chapter III. Machine Learning Results

This chapter is dedicated to the modeling results of both the unsupervised PCAk analyses and the supervised BNN analyses for two different feature sets pertaining to heat and permeability (described in 3.1). Each method evaluates the full extent of the PFA study area (1,728,000 grid points). Modeling is performed using python and open source Keras, TensorFlow, PyTorch, and Scikit Learn libraries (Pedregosa et al., 2011; Chollet et al., 2015; Abadi et al., 2015; Paszke et al., 2019).

3.1 Model Optimization and Evaluation

Various validation metrics are introduced to evaluate modeling performance. The first

stage of this work is focused on the PCAk analysis, which requires identifying an

appropriate number of principal components and clusters. The number of principal

components used in the reduction is truncated by evaluating a plot of the variance

explained by each principal component (also known as a scree plot) to identify inflections

in the curve of variance explained and possible thresholds in terms of cumulative

variance (~60% or greater).

After performing the PCA reduction, determining the number of clusters for k-

means clustering commonly involves experimenting with a range of values and

evaluating the compactness of the resulting solution. An inflection in a plot of the within-

group sum of squares as a function of the number of clusters is used to denote the

appropriate number of clusters present in the data (e.g., Everitt et al., 2010). Evaluating

solutions for clusters also benefits from visualizing different values with reference to a-

priori knowledge.

To perform the BNN analysis, data inputs include the full sets of features and the

training sites with additional neighboring grid points as training samples (415 positive

and 310 negative sites total). An estimate of the prior weight and bias distribution is set to

near Gaussian, and additional hyperparameters (e.g., regularization term) are set based on

model training/testing performance with an experimental range of values. Once the

hyperparameters are selected for each feature set, the test results from the variational

BNN analysis are sampled to observe a range of posterior predictions at each grid block

(Figure 3.1). This range is used to optimize the probability distribution of the parameters

(mean and standard deviation) of each weight and bias based on the selected prior

inference. To evaluate the results and illustrate the diagnostic ability of the classifier,

various metrics are reviewed including loss, accuracy, the receiver operating

characteristic curve, and the precision/recall curve. Model performance is evaluated

during training with accuracy and loss, and during testing with the receiver operating

characteristic curve and precision/recall curve. In the training stage, the ability of the

BNN to return improved accuracy and a decrease in loss over time is analyzed. In the

testing stage, the predictive generalization power of the model is evaluated at various

discrimination thresholds (e.g., 50%, 60%, etc.,) based on the scores for the receiver

operating characteristic curve and precision/recall curves (ranging from zero to one) (e.g.,

Davis, J., 2006), whereby the closer the area under the curve is to one, the better the

predictive performance of the model with test data. The receiver operating curve

considers both the true positive rate and false positive rate according to different

probability threshold values. For the precision/recall curve, precision is:

$$precision = \frac{true\ positives}{(true\ positives + false\ positives)} \tag{3}$$

which is the ability not to label a positive sample as negative, whereas recall is:

$$recall = \frac{true\ positives}{(true\ positives + false\ negatives)} \tag{4}$$

which is the ability to find all the positive samples.

R165C396 Wild Rose
posterior predictions
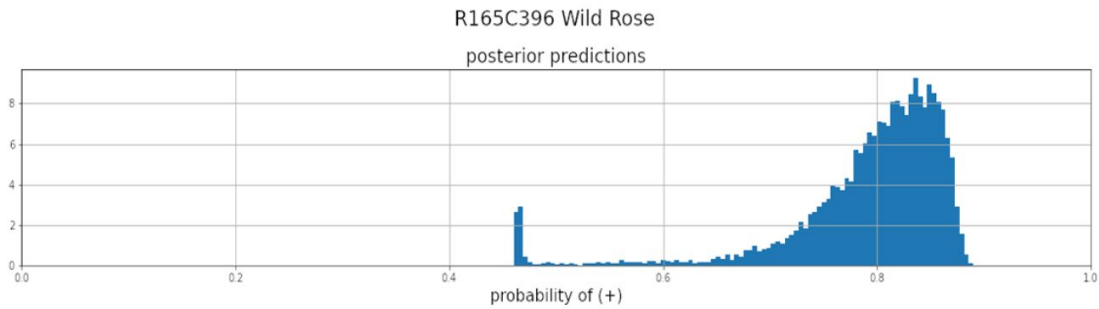
Figure 3.1. *Example of the distribution of posterior predictions (i.e., test results) at a single grid block (at Wild Rose, a known geothermal system/positive training, see Appendix A, ID 82) from the variational BNN analysis of feature set one.*

The parameterization of the BNN and PCAk techniques has a great influence on their robustness and predictive performance. Artificial neural network modeling has a stochastic nature, where the predictive outputs can vary because of the random initialization of weights for input features. To address this uncertainty, the variational BNN analysis was identified as an optimal approach based on the regularization by a compression cost on the weights and its capacity to produce a distribution of weights and biases, thus producing a reasonable ensemble of models to sample from. With PCAk, the k-means clustering algorithm also has a stochastic nature and this method produces a distribution of cluster centroids that vary to some degree based on the random initialization of cluster centroids. The selection of the best PCAk results was a heuristic decision that followed scrutinizing different outputs, which generally converged on the same cluster patterns even with different centroid initializations.

3.2 Feature Set Results

In each feature set analysis, the appropriate number of PCs for PCAk modeling was

identified to be four, and the number of clusters for PCAk to be three. PCAk results

include 1) mixing matrix maps (W) and a feature matrix (H) for the first four principal

components; 2) scree and within group sum of squares plots; 3) a biplot of the first two

principal components; 4) a matrix of the sum of PC feature loadings at the center of each

cluster; 5) a spatial map where locations of each cluster member are projected onto the

DEM-30m layer (where darker colors indicate higher elevation) that also includes the

labeled domains (WGB = western Great Basin, WL = Walker Lane, CNSB = central

Nevada seismic belt, CA = carbonate aquifer) and their boundaries; and 6) a table

summarizing cluster distributions and feature characteristics.

The PCA biplot can be used to interpret underlying characteristics of each cluster

by observing the feature vectors that extend from the origin of each biplot and their

relation to each cluster (Figure 3.2). A vector is defined from the center of the plot to the

vector vertex (endpoint), and the length of the vector is proportional to the fraction of the

total variance explained by that feature, where larger vectors have a higher influence on

data position. The arrowhead on each vector corresponds to high values of that particular

feature (Pepin, 2019). Notably, the biplot is a constrained representation of underlying

cluster characteristics, because the biplot only depicts the PC1 and PC2 results versus the

four PCs used for k-means analysis. To provide a more comprehensive understanding, a

matrix is also included of the sum of loadings at the center point of each cluster for PC1-

4, to give a score for the overall influence of each feature in the spatial distribution of each cluster.
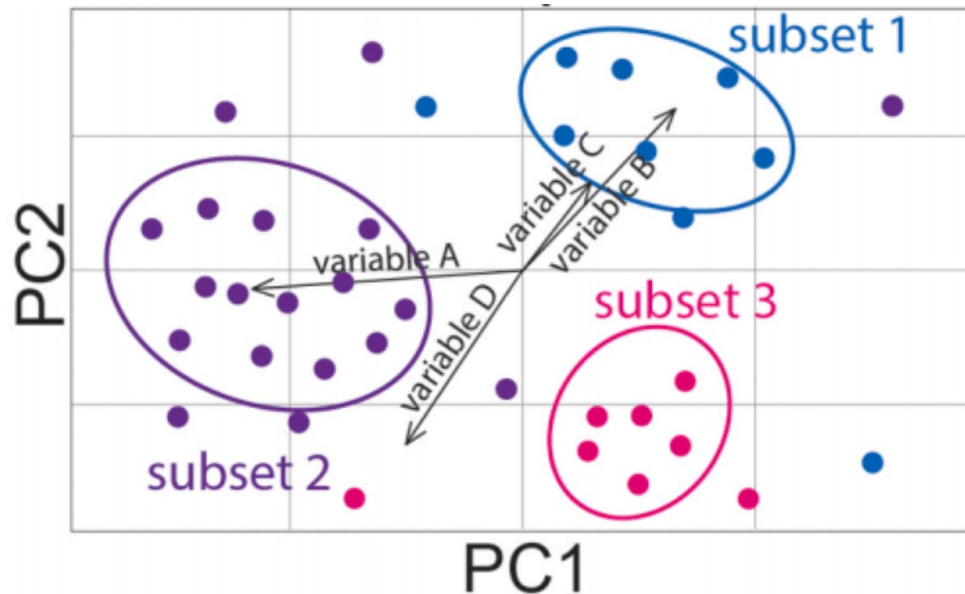
Figure 3.2. *Example PCA biplot. This figure shows a simplified biplot to help demonstrate the main interpretable relations. For PC1 vs. PC2, variables B, C, and D distinguish subset 1. Variable B is more strongly related to subset 1 relative to variable C. Variable D is inversely related to subset 1. Variable A distinguishes subset 2. No variables uniquely distinguish subset 3 (modified from Siler and Pepin, 2021).*

BNN modeling includes all the original input features for each respective feature set. The BNN results include predictive output maps as well as plots for loss, accuracy, receiver operating curve, and precision/recall. The threshold for predictions (0 to 1) is set to be at 50% (0.5) for each of the probability maps. Maps from the BNN results consist of 1) the mean value of the BNN probability distribution output (Bayesian mean map of the 50th percentile); 2) a 68% confidence bound map; and 3) the 5th percentile of the BNN probability distribution. Since the modeling is guided by a normal prior distribution

(Figure 3.2), the 68% confidence map (i.e., a map of the range of predictions from the mean to +/- two standard deviations) helps to identify the range or variation of each grid point prediction with respect to the mean prediction. In this map, higher values (cooler colors) indicate a deviation from the mean prediction values (i.e., less confidence). Finally, the 5th percentile map is selected as the preferred map to display predicted geothermal favorability and includes spatial reference to major domains and training sites. A probability value on this map means that 95% of all of the Bayesian models used in the analysis would have a value greater than or equal to the value shown on the map (S. Brown, personal communication, 2021). This lower percentile range is particularly useful to isolate points in the study area have the highest fidelity in terms of positive predictions.
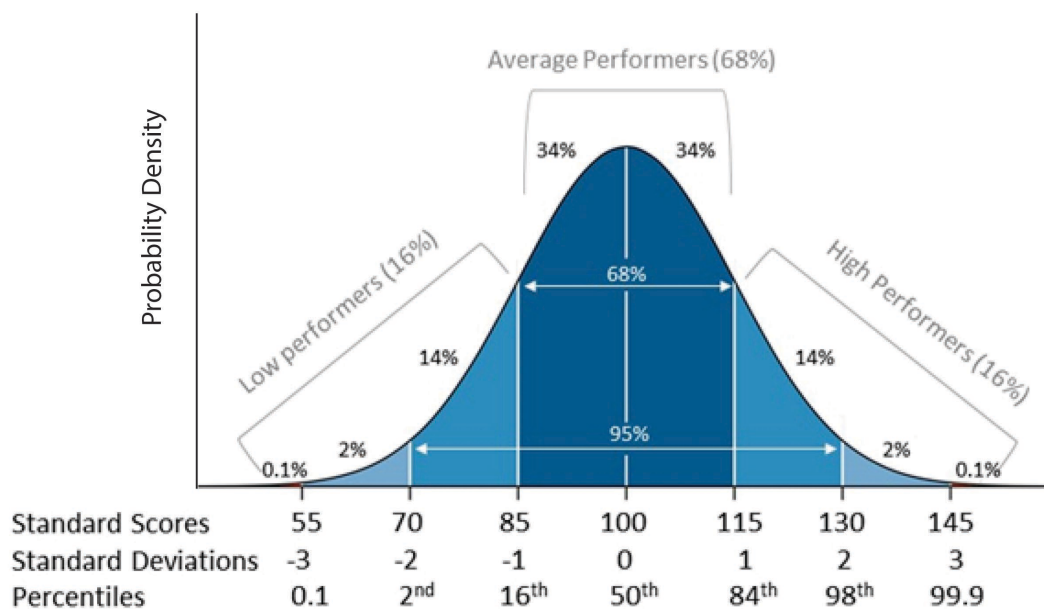
Figure 3.3. *Example of the probability density for a normal Gaussian sampling distribution. Annotations include labels for standard scores, standard deviations, percentiles, and the range of low to high performers.*

3.2.1 Feature Set One Results

Feature set one includes ten features pertaining to regional permeability (Figure 3.4).

These feature maps represent those data that were incorporated in the initial PFA

(geodetic strain rate, Quaternary slip rate, fault recency, Quaternary fault slip and dilation

tendency, and earthquake density), data that were augmented (Quaternary fault distance,

horizontal gravity gradient), and data that have been newly integrated during the machine

learning study (horizontal magnetic gradient, heatflow, and a 30m digital elevation

model). To perform the k-means cluster analysis, these features are reduced using PCA

into four principal components (Figure 3.5).
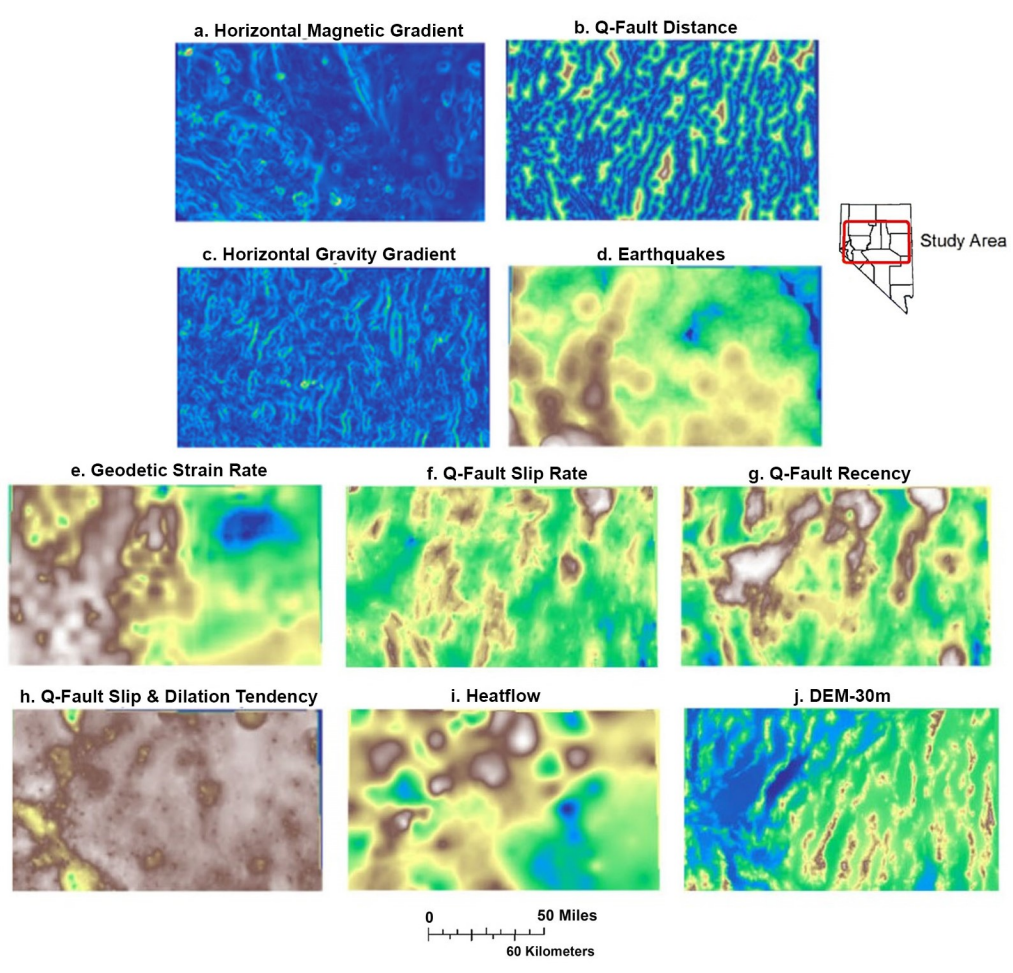
Figure 3.4. Feature set one color contoured maps. Warmer colors indicate higher feature values.
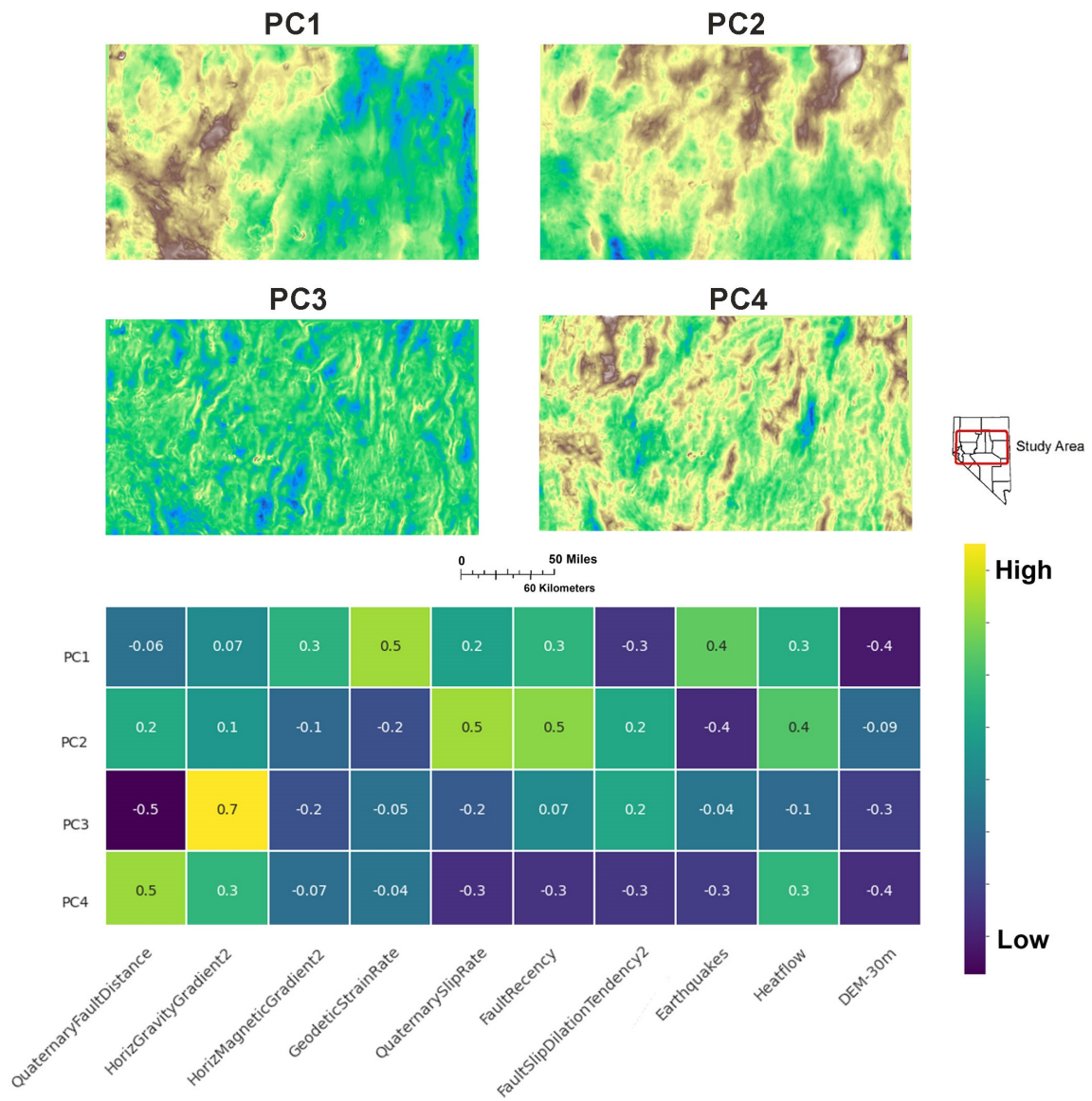
Figure 3.5. *Features set one PCA spatial plots of mixing matrix (W) maps of PC1-PC4 and accompanying feature matrix (H). The percentage of total variance explained by each principal component is: 24% (PC1), 18% (PC2), 11% (PC3), and 9% (PC4). In the feature matrix, the columns quantify the sources of variance related to the 10 features as loading values.*

Feature set one results (Figures 3.6 to 3.11 and Table 4) indicate that the spatial distribution of clusters is divided into fairly homogenous groupings, and that the majority of the study area falls above 50% in the probability outputs. The BNN validation metrics and confidence bound map (Figures 3.8 to 3.10) indicate that the model performs well as a classifier and that there is generally less confidence in the areas of highest favorability, but higher confidence around predictions of ~60% probability of a positive site.

Looking at the PCAk and positive BNN fairway maps from west to east, cluster 3 (purple; Table 4) appears to dominate most of the Walker Lane, central Nevada seismic belt, and the western subregion of the western Great Basin, with several pockets in the eastern subregion of the western Great Basin and the carbonate aquifer. This cluster hosts a far greater percentage of positive sites than negative, and its distribution appears in areas with high probability. Cluster 1 (green; Table 4), which has relatively higher variation in its distribution across the study area is most prevalent in the northern half of the study area in the western Great Basin and the carbonate aquifer. This cluster group hosts a balanced percentage of positive and negative sites, and the probability values in this region generally have an above 50% output with a slightly lower range of probability values to the east. Cluster 3 (blue; Table 4) is primarily concentrated in the southeastern portion of the carbonate aquifer, with notable pockets along ranges to the north in the carbonate aquifer, western Great Basin, and Walker Lane. This cluster group hosts a far greater percentage of negative sites than positive and scores in the lower range of probability values.
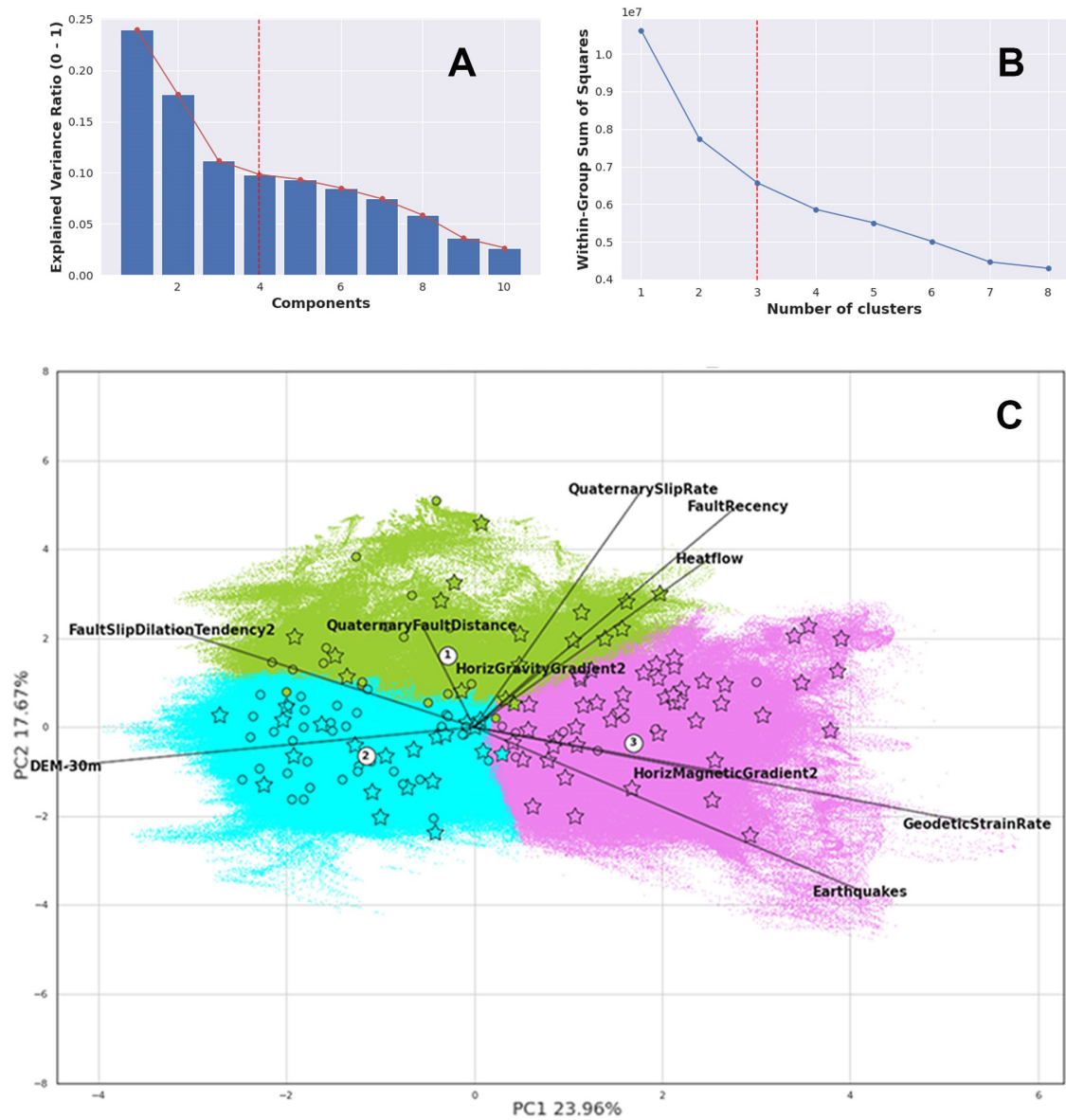
Figure 3.6. *Feature set one (A) PCAk plot of explained variance for each component; (B) Within group sum of squares plot for different cluster values; and (C) The PC1 PC2 biplot with color-coded k-means cluster groups points, stars being positive training sites and circles being negative training sites. The axes of PC1 and PC2 also include the explained variance for each component.*
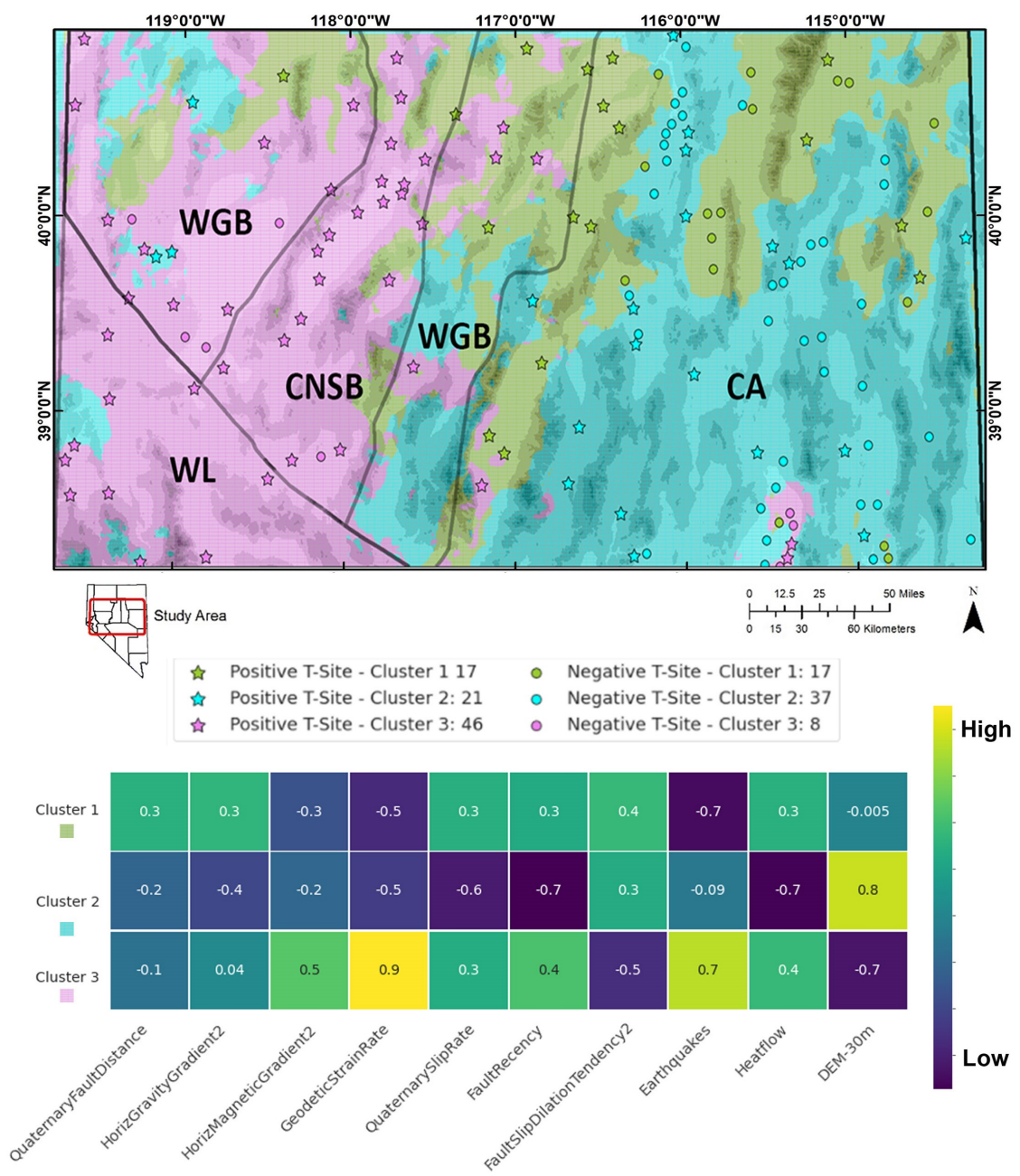
Figure 3.7. *Feature set one PCAk cluster map of the study area and PCAk feature score matrix (the sum of loadings at the center point of each cluster for PC1-4) for three cluster groups. The PCAk feature matrix is used to reference the influence of each feature in the spatial distribution for each cluster group. Acronyms for the labeled domains in the cluster map include: WGB = western Great Basin, WL = Walker Lane, CNSB = central Nevada seismic belt, CA = Carbonate Aquifer.*

Table 4. Feature set one cluster patterns. Acronyms for the labeled domains in the cluster map include: WGB = western Great Basin, WL = Walker Lane, CNSB = central Nevada seismic belt, CA = Carbonate Aquifer.

	Cluster 1 (Green)	Cluster 2 (Blue)	Cluster 3 (Purple)
Distribution	Mostly the northern half of the study area in the WGB and CA. Hosts 20% of positive sites and 27% of negative sites	Mostly Southern CA. Hosts 25% of positive sites and 60% of negative sites	Mostly the western half of the study area in the WL, western portion of the WGB, and the CNSB. Hosts 55% of positive sites and 13% of negative sites
Direct Correlation	➢ Q. Slip Rate ➢ Fault Recency ➢ Heatflow ➢ Q. Fault Distance ➢ Fault Slip and Dilation Tendency	➢ DEM-30m ➢ Fault Slip and Dilation Tendency	➢ Geodetic Strain Rate ➢ Earthquakes ➢ Horizontal Magnetic Gradient ➢ Fault Recency ➢ Heatflow
Inverse Correlation	➢ Earthquakes ➢ Geodetic Strain Rate	➢ Fault Recency ➢ Heatflow ➢ Geodetic Strain Rate ➢ Q. Slip Rate	➢ DEM-30m ➢ Fault Slip and Dilation Tendency
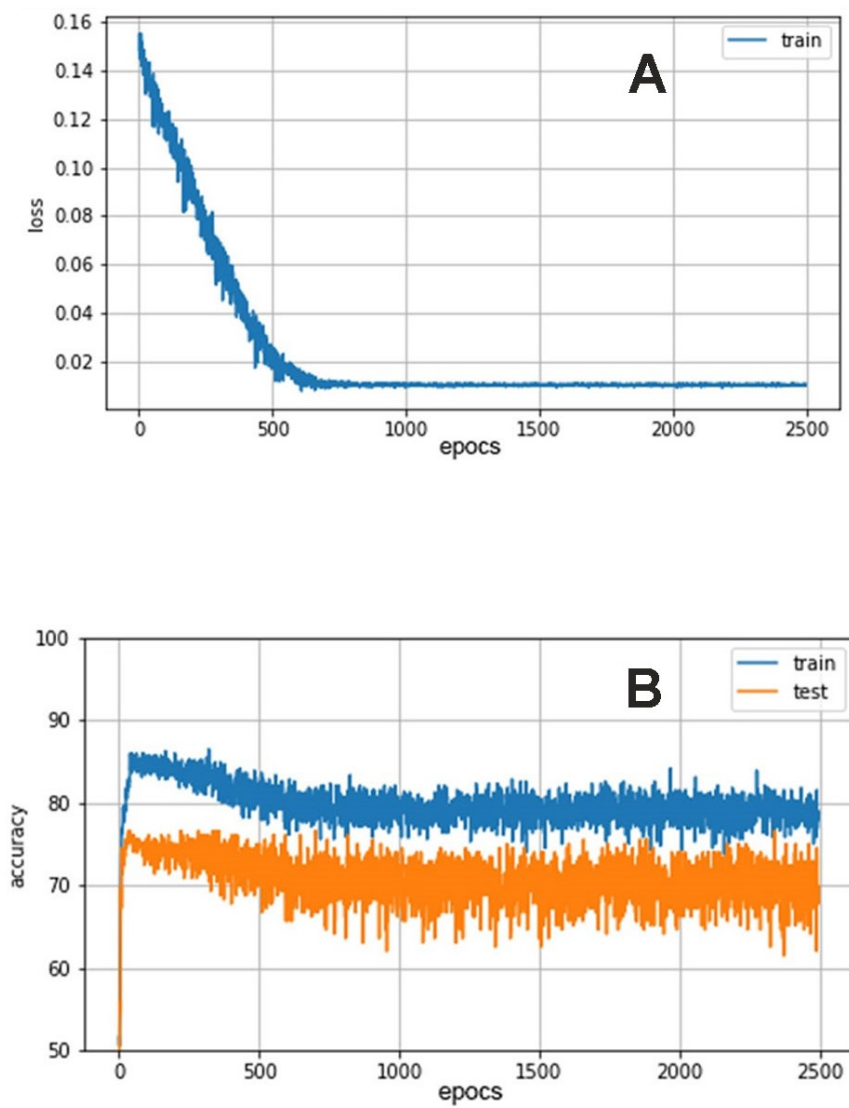
Figure 3.8. *Feature set one (A) loss and (B) accuracy validation metrics based on variational BNN training and testing.*
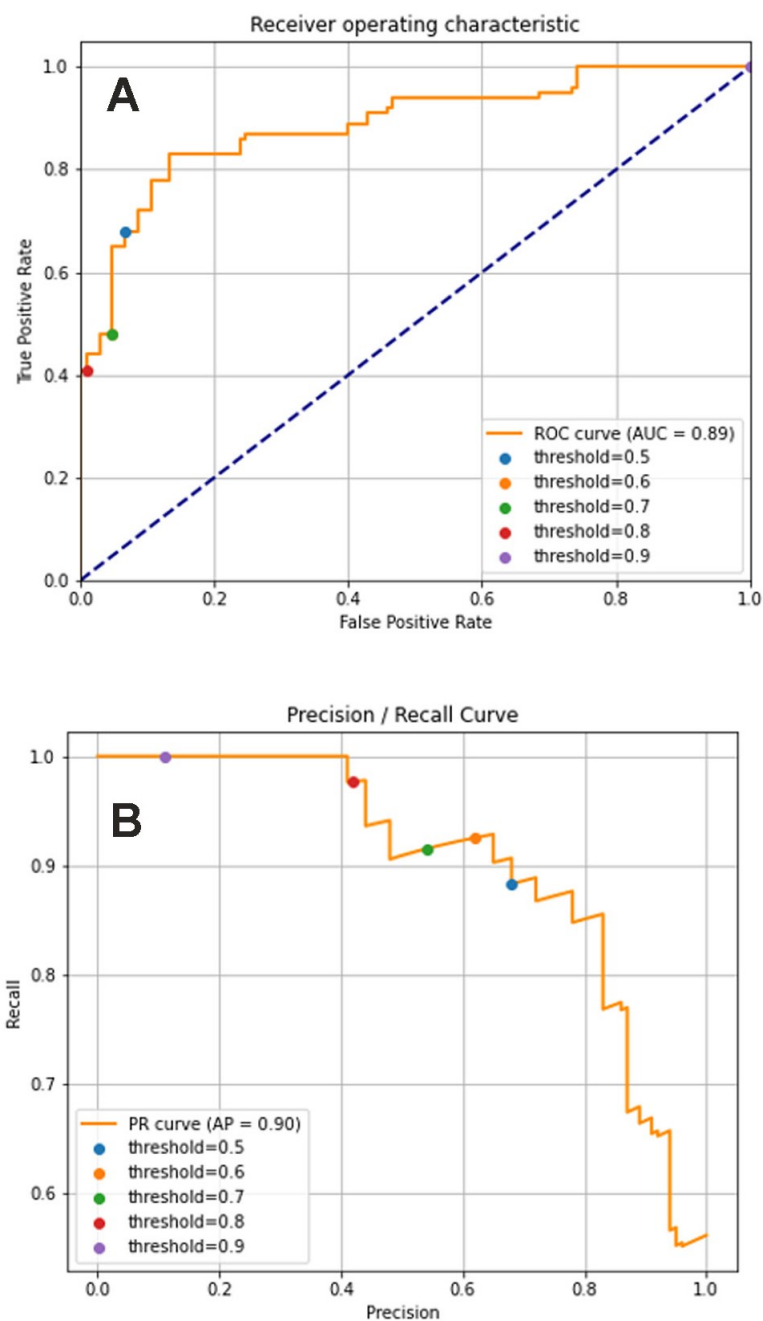
Figure 3.9. *Feature set one (A) receiver operating characteristic curve and (B) precision/recall curve based on variational BNN testing. Precision is the ratio of true positives / (true positives + false positives), which is the ability not to label a positive sample as negative, whereas recall is the ratio of true positive / (true positive + false negative), which is the ability to find all the positive samples.*
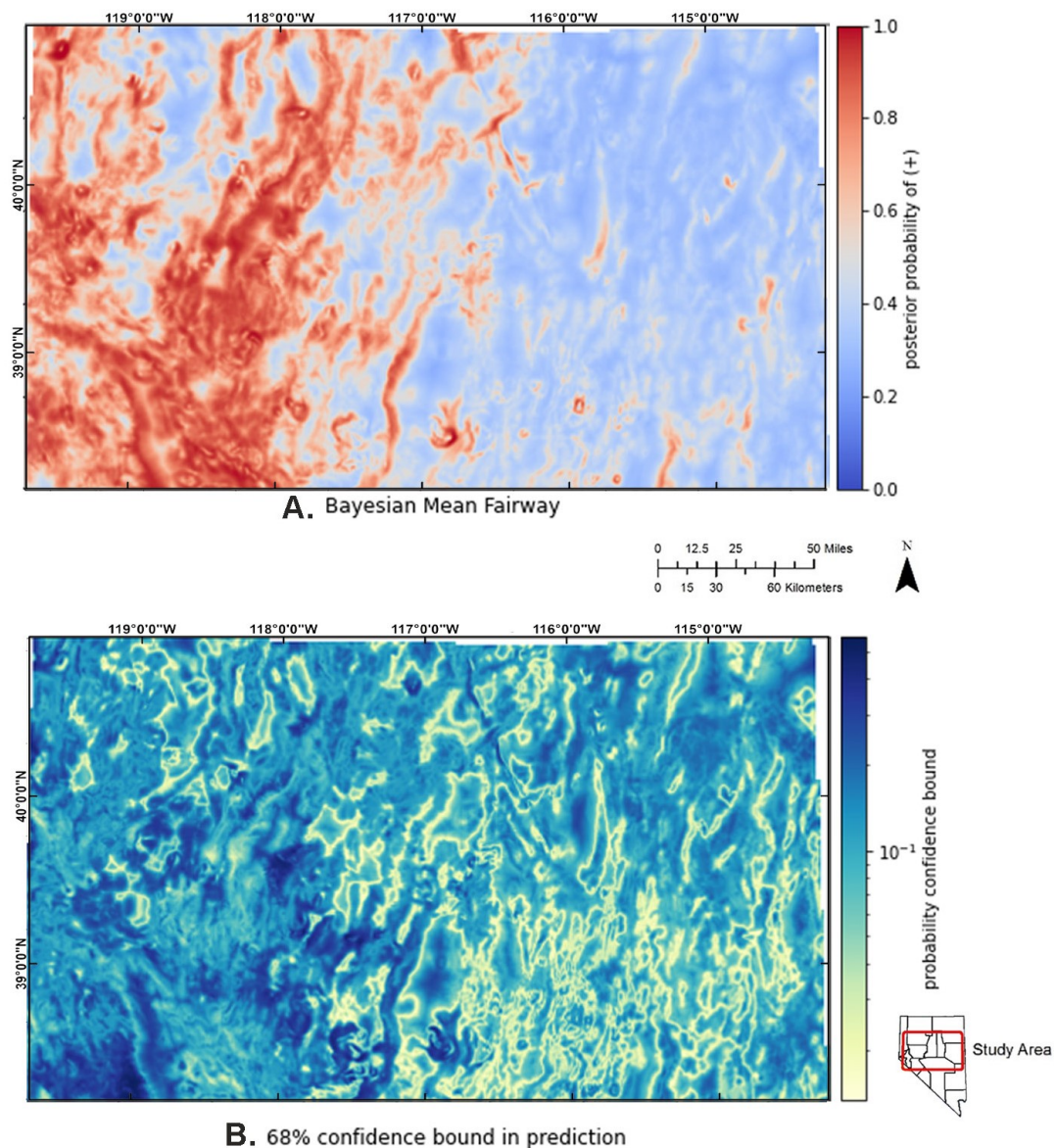
Figure 3.10. *Feature set one predictive maps of (A) the mean probability output and (B) the 68% confidence bound based on variational BNN testing. Warmer colors in the BNN probability map indicate higher geothermal favorability. Warmer colors in the 68% confidence bound map indicate the degree to which grid cells approach a normal Gaussian posterior probability distribution.*
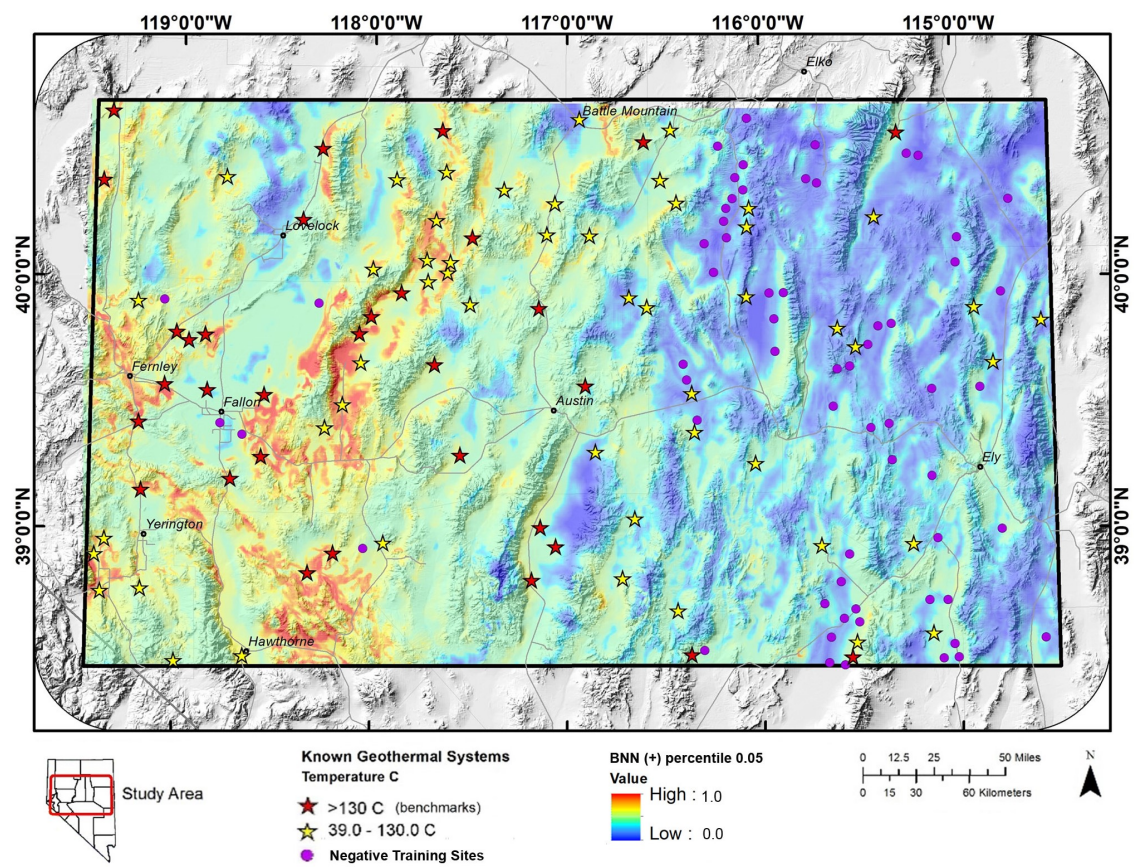
Figure 3.11. *Feature set one Bayesian 5th percentile fairway map. Plotted within the study area are BNN prediction values (normalized) ranging from a low of 0 to a high of 1. Positive training sites are plotted as stars (red ~ relatively high-temperature (>130°C), yellow relatively moderate temperature 39-130°C) and negative training sites as purple circles.*

3.2.2 Feature Set Two Results

Feature set two includes fourteen features pertaining to regional and local permeability (Figure 3.12). These are the same regional permeability feature layers as in feature set one with the addition of each of the original local permeability features used in the prior PFA study (structural setting, quaternary fault recency, Quaternary fault slip and dilation tendency, and Quaternary fault slip rate, all at the local scale). To perform the k-means cluster analysis, these features are reduced using PCA into four principal components (Figure 3.13).
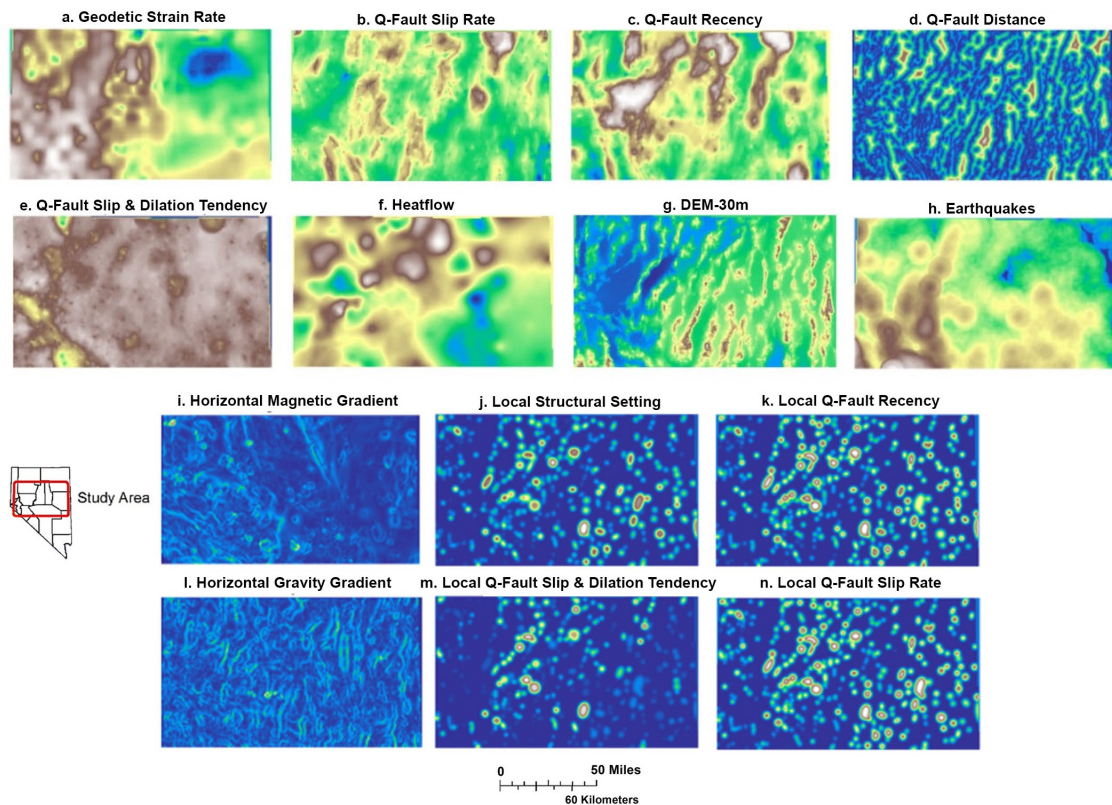
Figure 3.12. *Feature set two color contoured maps. Warmer colors indicate higher feature values.*
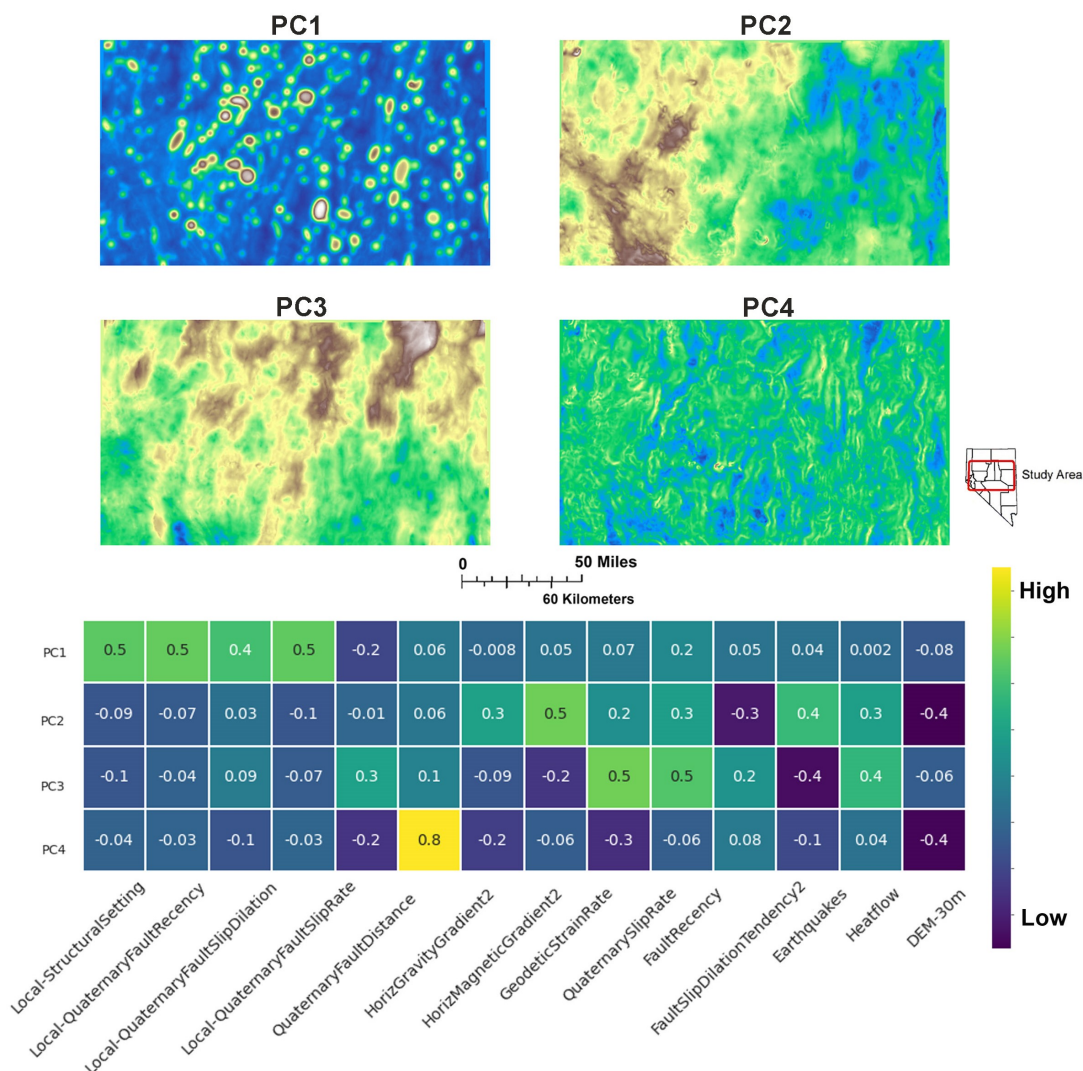
Figure 3.13. *Feature set two PCA spatial plots of mixing matrix (W) maps of PC1-PC4 and accompanying feature matrix (H). The percentage of total variance explained by each principal component is: 27% (PC1), 18% (PC2), 12% (PC3), and 7% (PC4). In the feature matrix, the columns quantify the sources of variance related to the 14 features as loading values.*

Feature set two results (Figures 3.14 to 3.19 and Table 5) are greatly influenced by the local permeability features concentrated in local structural setting ellipses. The local permeability features are each directly correlated to one another and inversely correlated to Quaternary fault distance in the PCA results, and they characterize both the

heterogeneous distribution of cluster group two (green; Table 5) and the highest

probability areas in the BNN predictions. The BNN validation metrics and confidence

bound map (Figures 3.16 to 3.18) indicate that the model has a stronger performance than

feature set one with classifying positive and negative training sites and that the model has

higher confidence in positive prediction values versus negative values. The highest

confidence bound values are primarily along the edges of structural setting ellipses which

fall in the range of 60-70% probability of a positive site, as well as within the structural

settings with the highest local permeability feature values. The majority of Bayesian

mean fairway predictions that fall less than 50% have a lower range of confidence

values.

In the PCAk and 5th percentile Bayesian fairway maps, cluster group two hosts

the majority of positive sites and a small percentage of negative sites. It is notable that the

number of positive sites in this cluster group is only 50, whereas a total of 68 out of the

83 positive sites fall within structural ellipses (7 negative sites also fall within these

ellipses). This contrast likely relates to the prescribed numerical ranking of local

permeability features within each structural setting, with the area inside of lower ranking

structures having a higher chance of mixing in with the grouping of cluster group three

(purple; Table 5) or two (blue; Table 5). Reviewing the other cluster groups from west to

east, cluster group three (purple; Table 5) is distributed throughout most of the Walker

Lane, central Nevada seismic belt and the western subregion of the western Great Basin,

as well as several pockets in the carbonate aquifer. Cluster group three hosts 31% of

positive sites and appears to have close to or slightly higher than 50% probability

averages in the BNN maps, with relatively high confidence. Cluster group one (blue;

Table 5) appears to be hosted primarily in the carbonate aquifer, with notable pockets at

and adjacent to ranges in the wester Great Basin and discrete portions of the Walker

Lane. This cluster group hosts a far greater percentage of negative sites than positive and

generally scores at or below 50% probability with relatively low confidence.
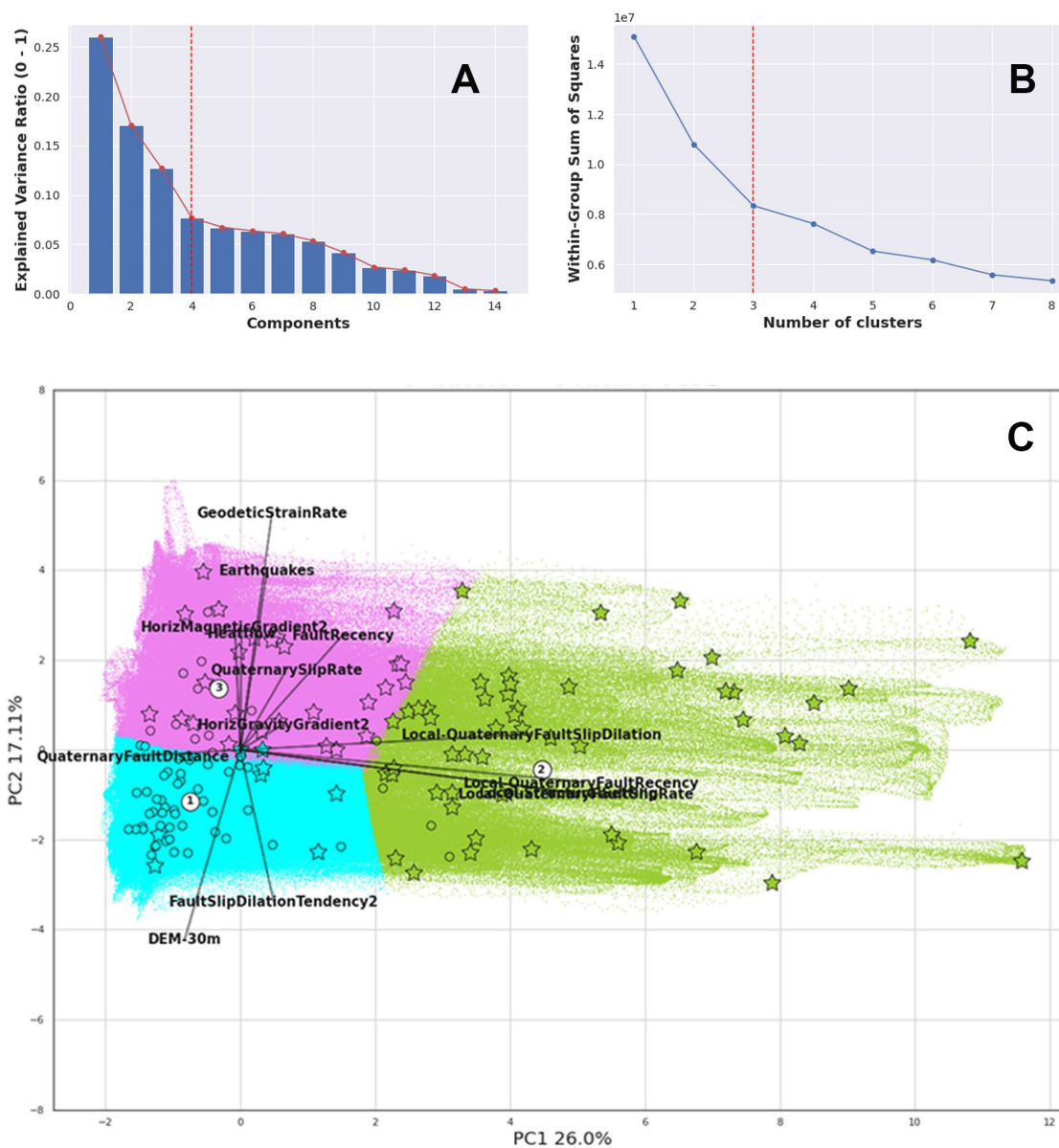
Figure 3.14. Feature set two (A) PCAk scree plot of explained variance for each component; (B) Within group sum of squares plot for different cluster values; and (C) PC1 PC2 biplot with. color-coded k-means cluster groups.,Stars being positive training sites and circles being negative training site. The axes of PC1 and PC2 also include the explained variance for each component.
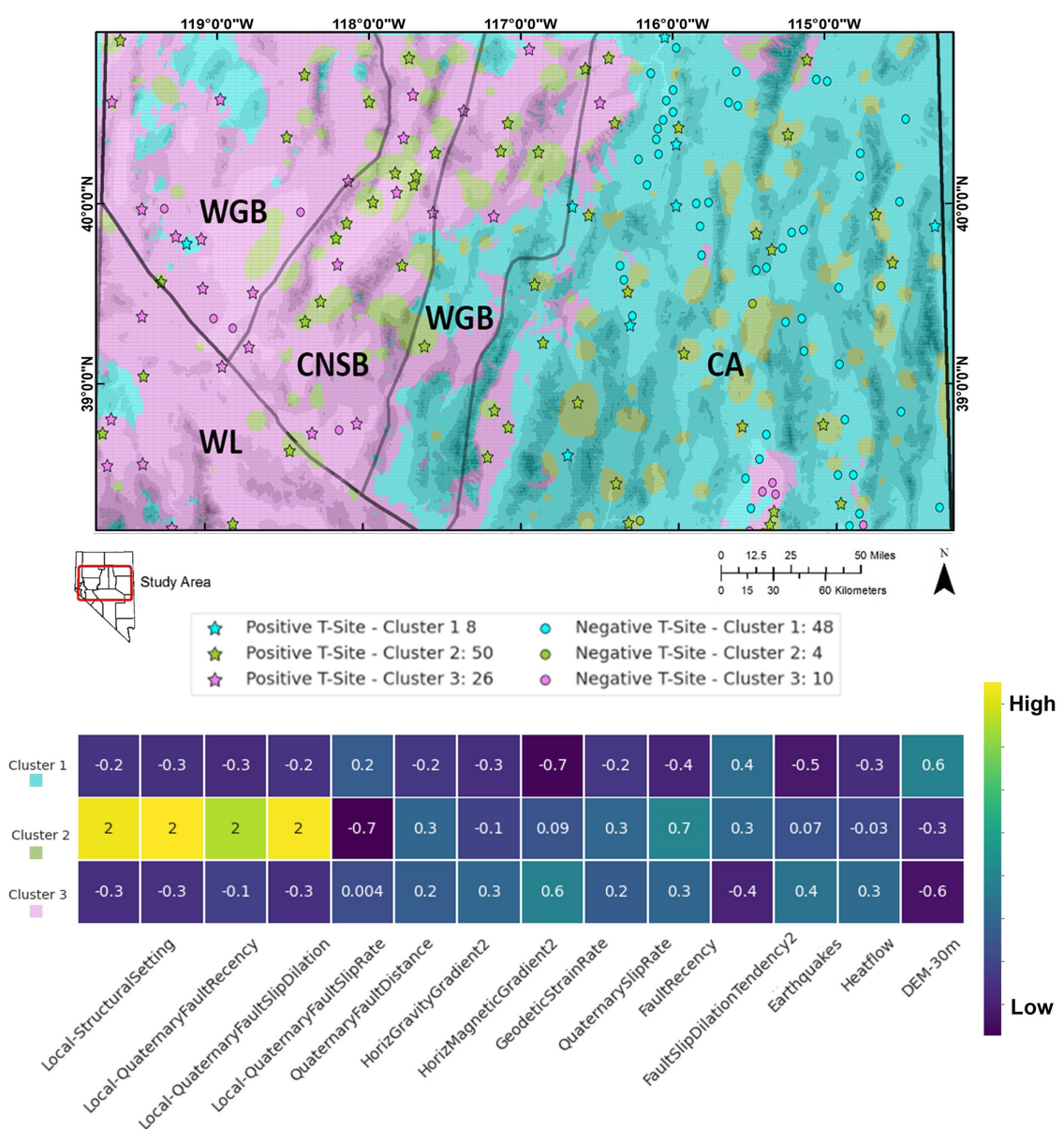
Figure 3.15. *Feature set two PCAk cluster map of the study area and PCAk feature score matrix (the sum of loadings at the center point of each cluster for PC1-4) for three cluster groups. The PCAk feature matrix is used to reference the influence of each feature in the spatial distribution for each cluster group. Acronyms for the labeled domains in the cluster map include: WGB = western Great Basin, WL = Walker Lane, CNSB = central Nevada seismic belt, CA = Carbonate Aquifer.*

Table 5. Feature set two cluster patterns including spatial distribution and notable features in terms of high or low values. Acronyms for the labeled domains in the cluster map include: WGB = western Great Basin, WL = Walker Lane, CNSB = central Nevada seismic belt, CA = Carbonate Aquifer.

	Cluster 1 (Blue)	**Cluster 2 (Green)**	**Cluster 3 (Purple)**
Distribution	Covering most of the eastern half of the study area. Hosts 9% of positive sites and 78% of negative sites	Concentrated within the extent of local structural setting ellipses. Hosts 60% of positive sites and 6 % of negative sites	Covering most of the western half of the study area. Hosts 31 % of positive sites and 16 % of negative sites
Direct Correlation	➢ DEM-30m ➢ Q. Fault Distance ➢ Fault Slip and Dilation Tendency	➢ Local-Q. Fault Slip and Dilation Tendency ➢ Local Structural Setting ➢ Local-Q. Fault Slip and Dilation Tendency ➢ Local-Q. Fault Recency ➢ Fault Recency	➢ Geodetic Strain Rate ➢ Fault Recency ➢ Heatflow ➢ Q. Slip Rate
Inverse Correlation	➢ Fault Recency ➢ Q. Slip Rate ➢ Geodetic Strain Rate ➢ Heatflow ➢ Local-Q. Fault Slip and Dilation Tendency	➢ Q. Fault Distance	➢ DEM-30m ➢ Fault Slip and Dilation Tendency ➢ Local-Q. Fault Slip and Dilation Tendency ➢ Local Structural Setting
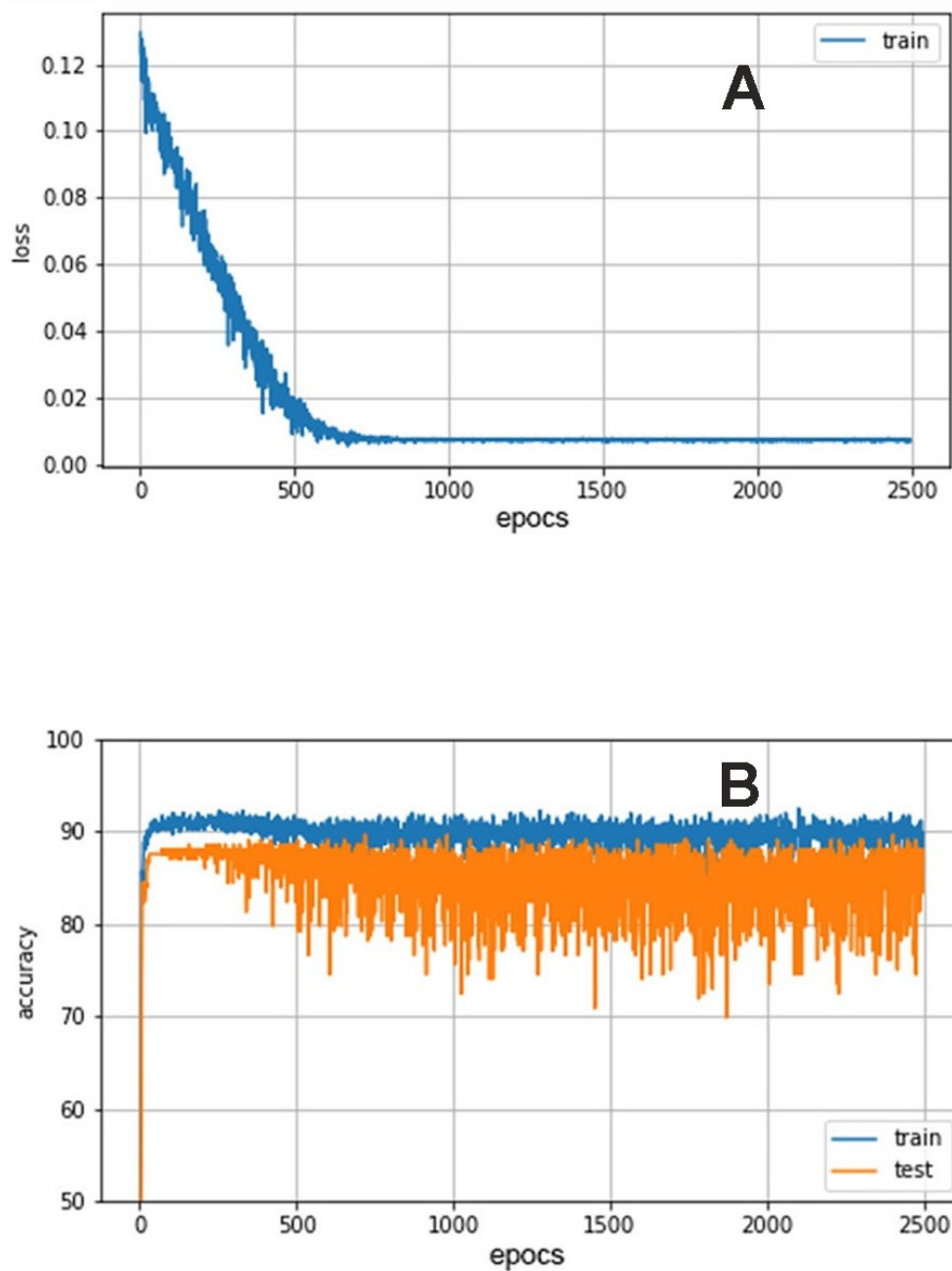
Figure 3.16. *Feature set two (A) loss and (B) accuracy validation metrics from the mean value based on variational BNN analysis training and testing.*
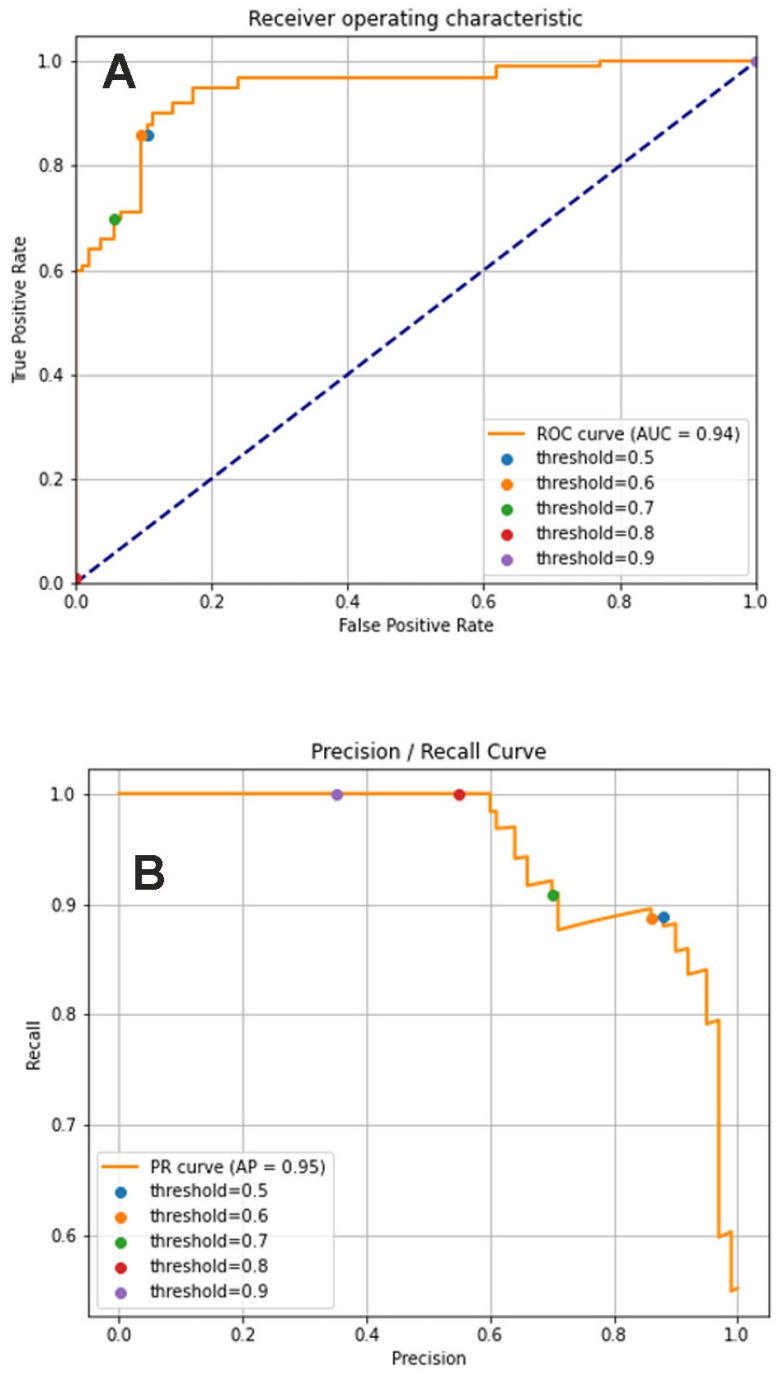
Figure 3.17. *Feature Set two (A) receiver operating characteristic curve, (B) precision/recall curve based on variational BNN testing. Precision is the ratio of true positives / (true positives + false positives), which is the ability not to label a positive sample as negative, whereas recall is the ratio of true positive / (true positive + false negative), which is the ability to find all the positive samples.*
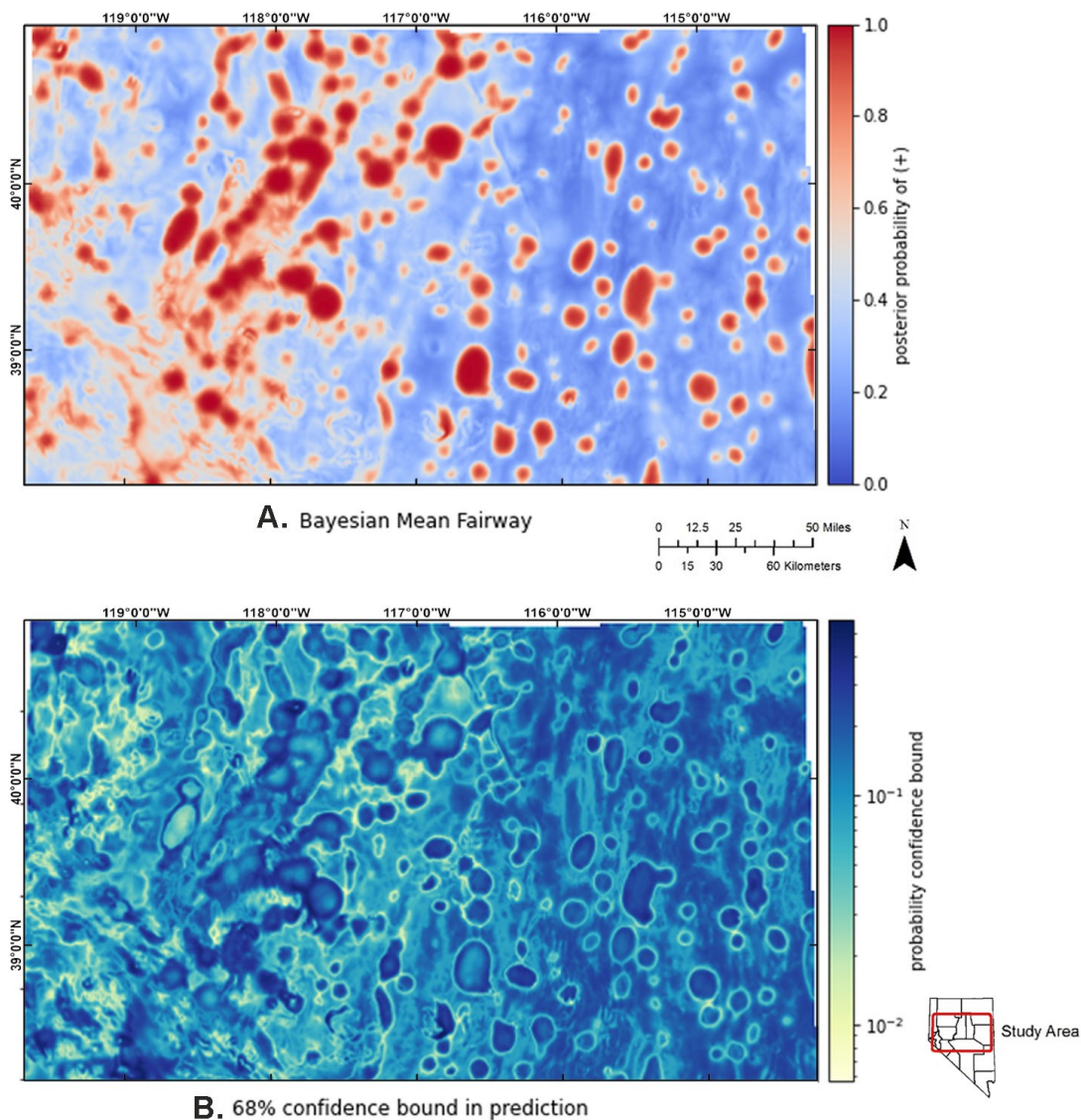
*:**Figure 3.18.** Feature set two predictive maps: (A) Mean probability output (B) 68% confidence bound based on variational BNN testing. Warmer colors in the BNN probability map indicate higher geothermal favorability. Warmer colors in the 68% confidence bound map indicate grid points that host a sample distribution that approaches a normal Gaussian distribution.*
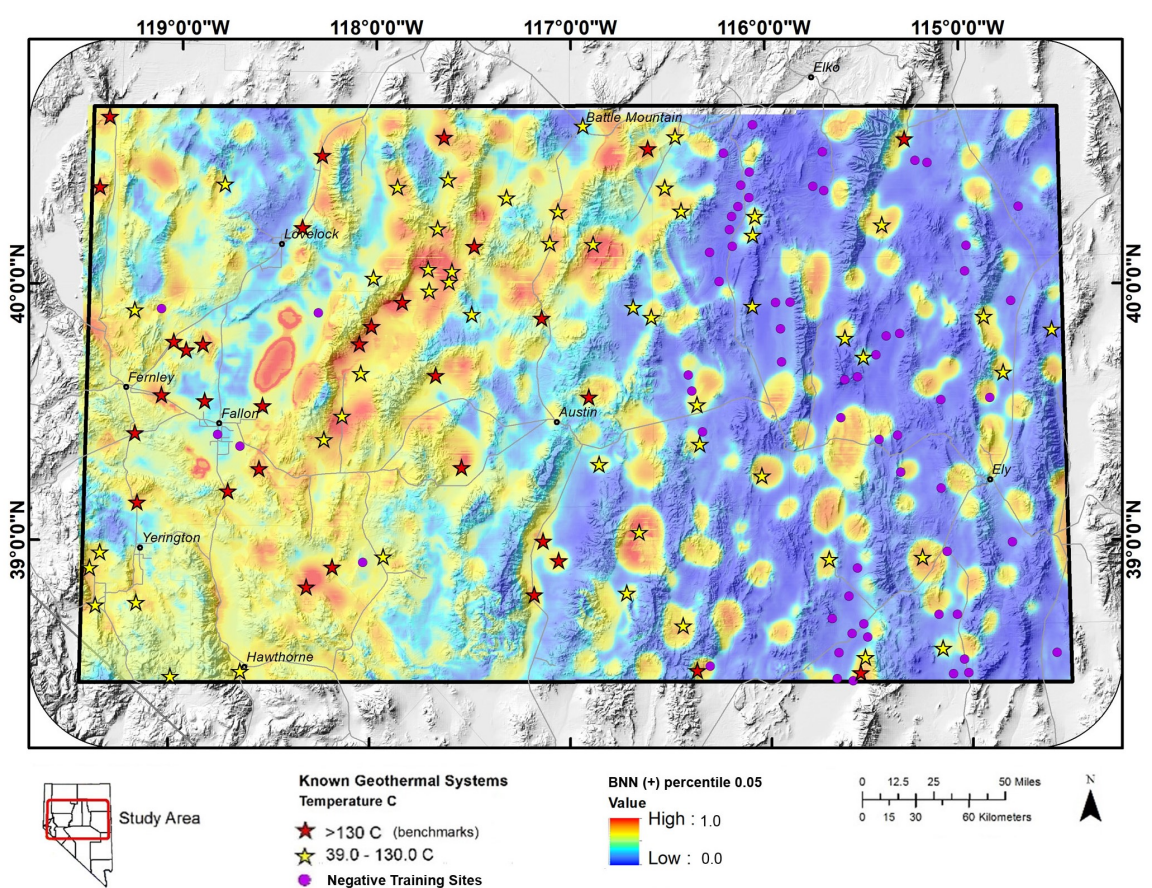
Figure 3.19. *Feature set two Bayesian 5th percentile fairway map. Plotted within the study area are BNN prediction values (normalized) ranging from a low of 0 to a high of 1. Positive training sites are plotted as stars (red ~ relatively high-temperature (>130°C), yellow relatively moderate temperature 39-130°C) and negative training sites as purple circles.*

Chapter IV. Discussion

4.1 Comparative Analysis of Modeling Results

The direct comparison of the results from the PCAk and BNN techniques helps to demonstrate some important lessons learned in this study and guide future modeling efforts. These results are organized below to compare PCAk results between both feature sets and selective BNN modeling with different inputs and outputs. In these analyses, feature set one results display a regional perspective in contrast to feature set two, which incorporates local permeability features at a subregional or local scale.

The comparative analysis of PCAk cluster maps for feature set one and two help to synthesize patterns of the relative influence of each feature in organizing cluster groups, and thus, data structure across the study area (Figure 4.1; Tables 4 and 5). In both cluster maps, there are distinct similarities between the spatial distribution of the blue and pink cluster groups, yet notable differences between the feature loadings due to inclusion of local permeability features in feature set two. In the feature set one analysis there are six principal feature relationships controlling the spatial distribution of both the blue and pink cluster group. The blue cluster group represents points that have a direct correlation with elevation, and inverse correlations with heatflow, fault recency, Quaternary slip rate, geodetic strain rate, and horizontal gravity gradient. The pink cluster group represent points that have direct correlations with geodetic strain rate, earthquakes, and horizontal magnetic gradient, and inverse correlations with elevation and fault slip and dilation tendency. In contrast, in the feature set two analysis, there are only four principal feature relationships controlling the spatial distribution of the blue and pink cluster group. The blue cluster group represents points spatially organized by inverse correlations with geodetic strain rate and earthquakes, and to a lesser degree direct correlations to elevation

and fault slip and dilation tendency. The pink cluster group represents points with direct correlations to geodetic strain and earthquakes, and inverse correlations to elevation and fault slip and dilation tendency.

The major spatial contrast between the PCAk results can be seen in the green cluster group. In the feature set one analysis, the green cluster group is most prevalent in the northern half of the study area in the western Great Basin and the carbonate aquifer. This cluster group is primarily controlled by inverse correlations to earthquakes, and geodetic strain rate, and to a lesser degree, direct correlations with heatflow, Quaternary fault slip rate, fault recency, Quaternary fault distance, and fault slip and dilation tendency. In the feature set two analysis, the green cluster group is primarily controlled by direct correlations with the four local permeability features concentrated in local ellipses defining favorable structural settings, and to a lesser degree, an inverse correlation with Quaternary fault distance (where positive values represent the distance from a fault). Overall, this analysis illustrates a more balanced distribution in terms of data variance and feature influence without the incorporation of local permeability features. Additionally, this technique provides key insights into which features are directly (e.g., earthquakes and geodetic strain rate) or inversely (e.g., local permeability features and Quaternary fault distance) correlated to one another.
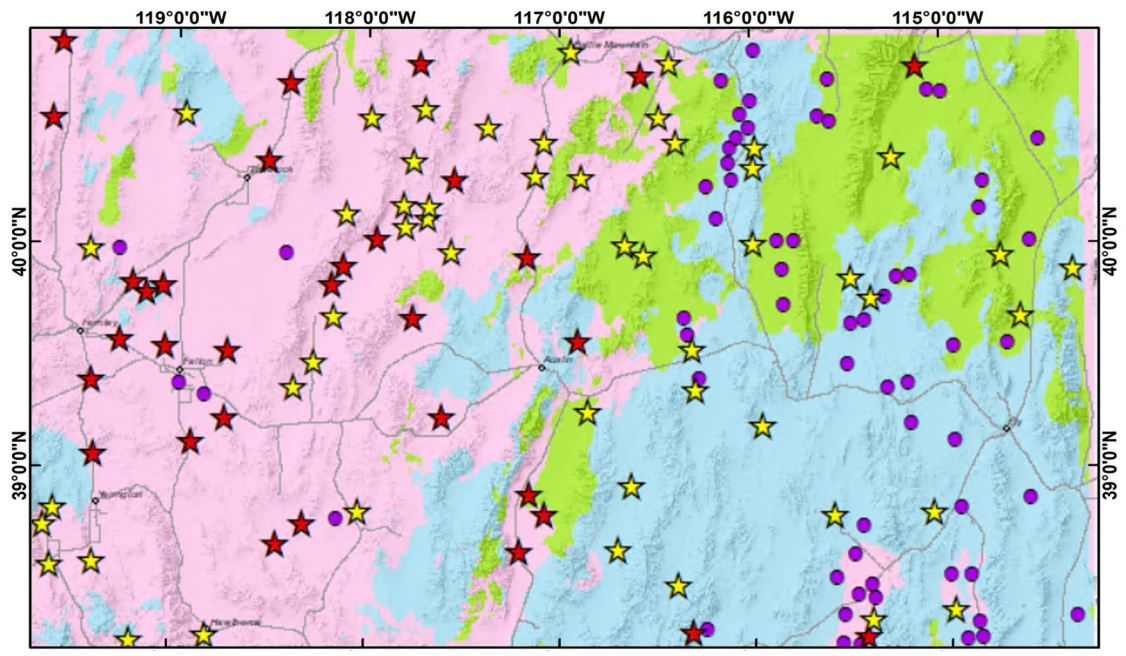
(A)

(B)

Known Geothermal Systems
Temperature C

★ >130 C (benchmarks)
☆ 39.0 - 130.0 C
● Negative Training Sites

Study Area
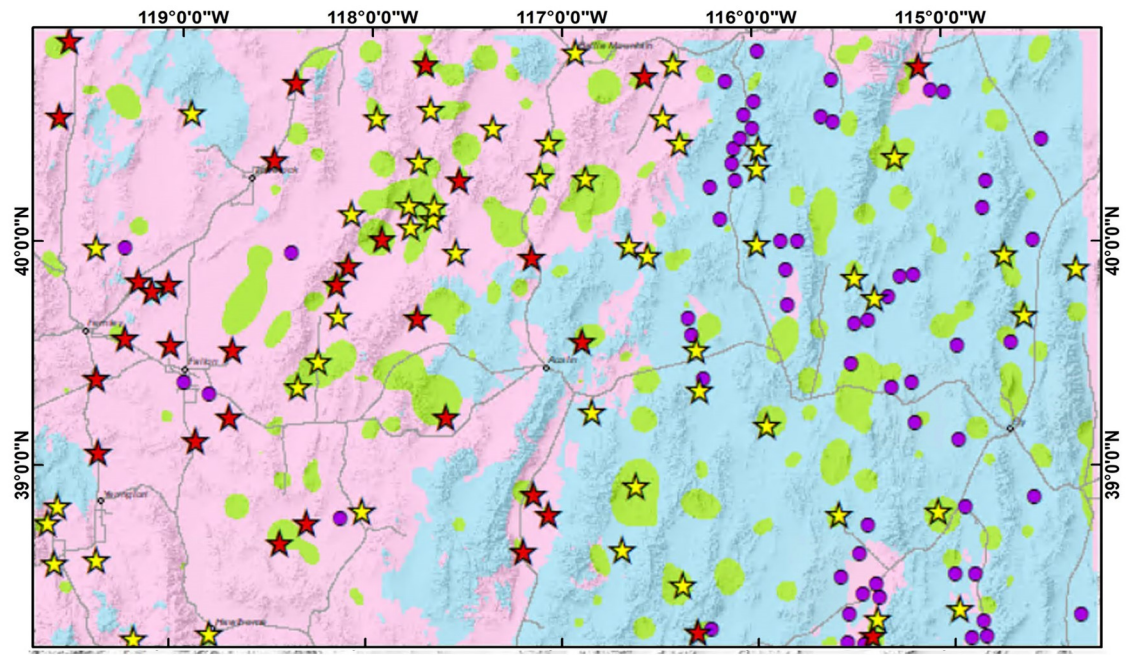
Figure 4.1. *Comparison of the PCAk maps with three clusters from PC 1-4 inputs of (A) feature set one and (B) feature set two. This map includes the locations of positive (red and yellow stars) and negative (purple triangles) training sites.*

The comparisons of BNN maps with each feature set benefit from referencing the PCAk analysis to contextualize spatial patterns. To help synthesize the results with both sets, the BNN outputs of the 50th percentile (mean probability) maps versus the 5th percentile maps, where there is a higher degree of confidence for every positive prediction, are demonstrated below (Figure 4.2). In both feature set results, there is a clear contrast between the predictions in the 5th percentile map versus the 50th percentile map, where areas of higher probability become more localized and discretely defined. In feature set one, the points with positive predictions and high fidelity in the 5th percentile map (Figure 4.2C) appear to be controlled by a mix of feature patterns relative to the results from feature set two (Figure 4.2D). In the feature set two maps, the same general areas are presented as highly favorable in both the 5th and 50th percentile maps and are largely controlled by the favorable structural settings and attendant local permeability features (Figure 4.2B,D). Besides the elliptical favorable structural setting zones in the feature set two results that appear directly linked to local permeability features, the localized patterns in each map are relatively difficult to interpret because BNN assesses features in such a way that spatial patterns are relatively obscure. PCAk analysis offers some important insights into these patterns, in particular that the majority of the areas with moderate to lower favorability predictions appear to correlate with the locations of the blue cluster groups seen in Figure 4.1. This may indicate that the features that control this cluster group are influencing the BNN model in denoting areas of negative

geothermal potential. However, because the confluence of regional features (with the exception of DEM-30 and fault slip and dilation tendency) have an inverse correlation to this cluster group and because there are more negative sites in the east (primarily within the blue cluster group) and positive sites in the west, it is more likely that an additional factor or separate analysis is needed to evaluate geothermal potential in these areas. This cluster group in the feature set one analysis also hosts many highly favorable known geothermal systems (e.g., McGinness Hills). Another factor to consider is that the datasets incorporated into this study may not properly account for the potential influence of the carbonate aquifer in entraining rising thermal fluids before they reach the surface and affecting the development of higher temperature geothermal systems.
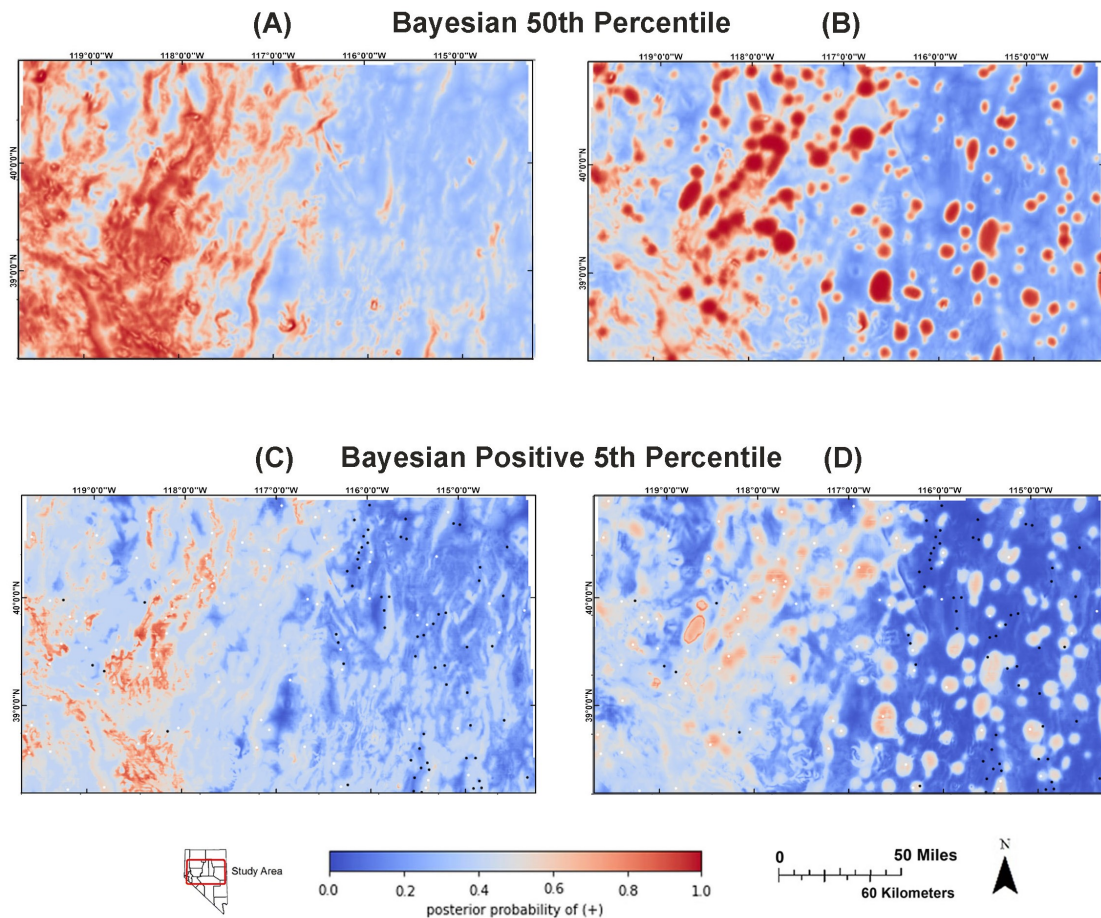
Figure 4.2. *Comparison of the maps from (A) the Bayesian 50th percentile for feature set one; (B) the Bayesian 50th percentile for feature set two; (C) the 5th percentile map for feature set one; and (D) the 5th percentile map for feature set two.*

Alongside evaluating the results from different feature set inputs, an avenue of particular interest was to evaluate the how new PC 1-4 reduced features compare to the full set of features in BNN modeling. The Bayesian 5th percentile maps for analysis (Figure 4.3A,C and Figure 4.3B,D) have similar structural and apparent localized similarities. However, the original input features appear to have a higher degree of granularity relative to the maps associated with PC 1-4 inputs. This is likely because PCA

is a linear algebraic method and the combination of features decorrelates the data and reduces second order dependencies, thus nonlinear/manifold structure may not be represented as strongly. However, distinct patterns revealed in the PC maps may help identify new and important links to guide exploration following a more detailed analysis.
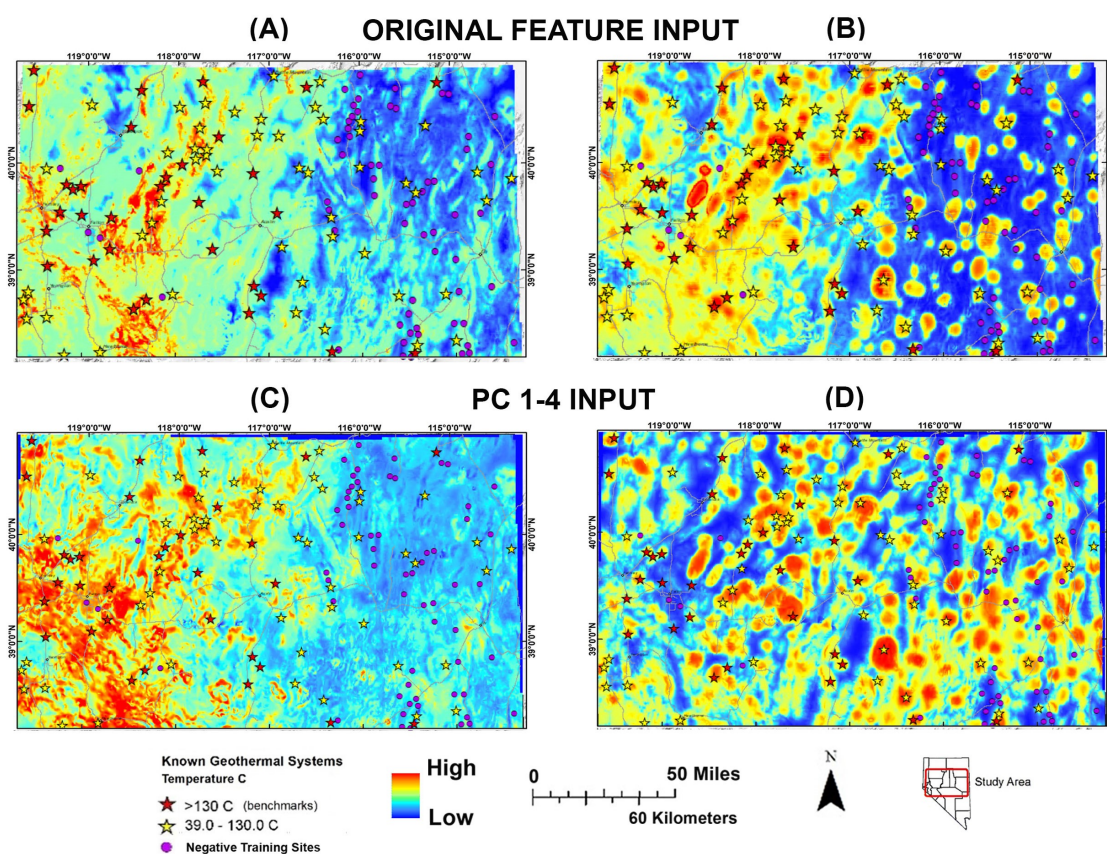
Figure 4.3. *Comparison of the Bayesian 5th percentile maps from (A) the ten input features for feature set one; (B) the fourteen input features for feature set two; (C) the PC 1-4 inputs of the reduced feature set one; and (D) the PC 1-4 inputs of the reduced feature set two. This map includes the locations of positive (red and yellow stars) and negative (purple triangles) training sites.*

An ancillary goal of this project was to assess the performance of similar dimensionality reduction methods capable of accounting for non-linearity/manifold structure in low-dimensional representation of multivariate data. This study explored both non-negative matrix factorization (e.g., Vesselinov et al., 2020) and T-distributed stochastic neighbor embedding (van der Maaten and Hinton, 2008), but following the evaluation of results from each method, PCA was selected as the preferred method. This was due to the lack of a notable contrast between the results of these methods and PCA, and the benefits that PCA offers by providing 1) a linear solution; 2) an understanding of the inverse correlation of features to a cluster group; and 3) a wholistic picture of feature influence by taking the sum of feature loading values (i.e., eigenvalues) at the center of each k-means cluster.

4.2 Guiding Exploration

In this study, the combined use of PCAk and BNN has proven to be a powerful approach for constraining patterns of elevated geothermal potential, complementing and in some cases enhancing the results produced by the original PFA. Key insights into the potential of this study to guide future exploration are provided through the direct comparison of BNN fairway map results to the original regional permeability and fairway maps from the PFA. Additionally, the regional perspective from BNN analysis with feature set one is framed around the areas surrounding several recently discovered blind systems to evaluate how the results at different percentiles appear at sub-regions of each system.

The input features for the PFA regional permeability model (4.4C) included horizontal gravity gradient and features that essentially track crustal deformation through time, from the past ~20 years (geodetic strain), to ~150 years (earthquakes), and to ~2.6 Ma (Quaternary slip rates). This model was recognized as a particularly useful guide for exploration, because much of the region has not been mapped at a sufficient scale to define local permeability or reflect the extent of Quaternary faulting. Small step-overs, terminations of small to moderate size normal faults, many fault intersections, and even some accommodation zones may not be detectable with currently available data. Also, major pluvial lakes, such as Lake Lahontan in the western part of the study area, essentially reset the Quaternary fault clocks at ~13 ka by eroding and burying all Pleistocene fault scarps in the affected basins. Because many of the fault zones within this region have earthquake cycles on the order of tens of thousands of years, the extent of Quaternary faults is probably far greater than that reflected by surface ruptures (Faulds et al., 2015a).

In the machine learning project, feature set one was selected to build on regional scale modeling by both introducing refined data (horizontal gravity gradient and fault slip and dilation tendency data), and experimenting with combining intermediate permeability (Quaternary faults as Quaternary fault distance), heat (heatflow), and several of the new available data sets (horizontal magnetic gradient and DEM-30m). The combination of these features aims to enhance the regional permeability model by more fully representing crustal deformation, heat, zones that collocate with existing Quaternary faulting, and areas where faults may not be readily detected.

In both the PFA regional permeability map and the feature set one Bayesian 5th percale map, prominent fairway belts stand out in the western domains of the Walker Lane and the central Nevada seismic belt. In the PFA study (Figure 4.4B), these areas reflected high strain rates, active faults, abundant earthquakes, and steep gravity gradients (Faulds et al., 2015a). Many belts of high favorability in the PFA regional permeability model are along main segments of major normal faults, owing primarily to the original horizontal gravity gradient data (both features are displayed in Figure 4.5), which commonly have high values in the vicinity of major normal faults due to the juxtaposition of lower density sedimentary basin fill against high density basement rocks. These areas are commonly not associated with geothermal activity, whereas the ends and discontinuities (e.g., step-overs, intersections with other faults) along such faults do correlate with geothermal systems (Faulds et al., 2015a). In the BNN analysis, many of the same segments exist at higher percentiles (e.g., 50th percentile), but the predictions at lower percentiles constrain more localized zones of favorability. This is highlighted in the 5th percentile map (Figure 4.4A), where areas of elevated geothermal potential appear to be more concentrated at the ends and discontinuities of major Quaternary normal faults.

(A) FEATURE SET 1 INPUT

Known Geothermal Systems
Temperature C

★ >130 C (benchmarks)
☆ 39.0 - 130.0 C
● Negative Training Sites

High

Low
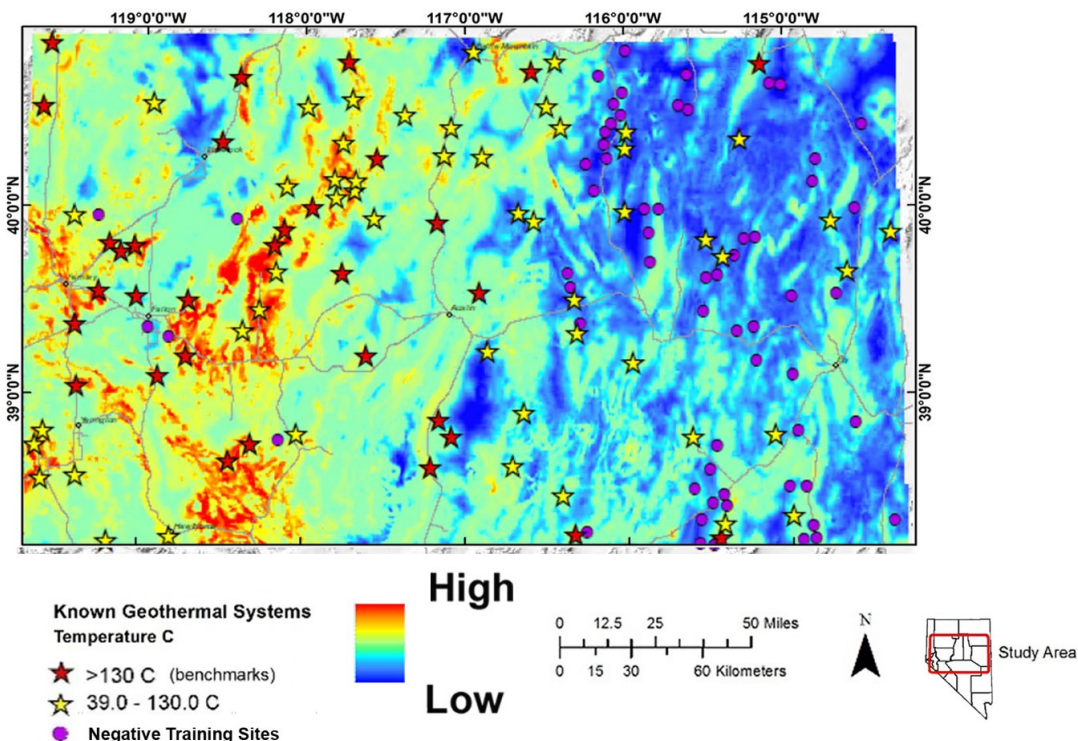
(B) ORIGINAL PFA REGIONAL PERMEABILITY
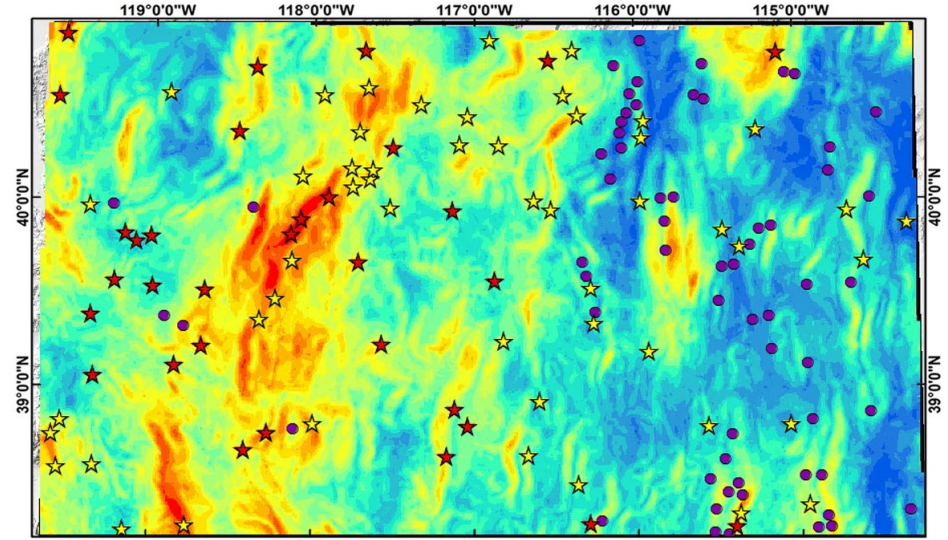
Figure 4.4. Comparison of the (A) feature set one 5th percentile map and (B) the original PFA Regional Permeability model. This map includes the locations of positive (red and yellow stars) and negative (purple triangles) training sites.
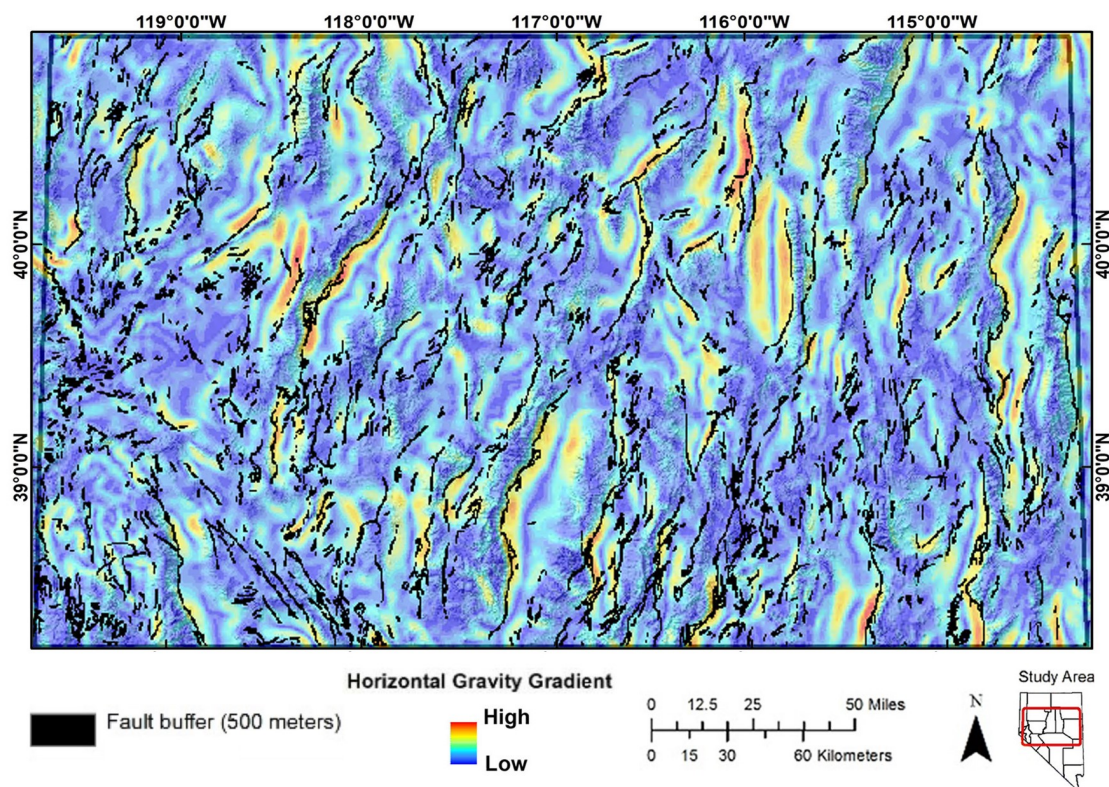
Figure 4.5. The map of the original total horizontal derivative of the Complete Bouguer anomaly computed at 2.40 g/cc used the PFA, as well as the location of Quaternary faults (with 500m buffers) (modified from Faulds et al., 2015a).

Further insight into the utility of the BNN technique can be gained by considering the PFA fairway model (Figure 4.6). The fairway model incorporated regional permeability, local permeability, and heat to produce the primary predictive product of the study. Both models are particularly useful to evaluate the many structural settings (Figure 4.7) relative to one another. However, there are notable contrasts in the new BNN

analysis. In particular, compared to the PFA fairway model, there is more broadly distributed favorability within each favorable structural setting ellipse and higher degrees of favorability along the margins of these ellipses and Quaternary fault traces. This is likely a consequence of the density and distance transformations introduced in this study to convert the local permeability and Quaternary fault trace features from categorical to numerical features. This represents a promising adaptation, because BNN results with these transformed features are more likely to reflect areas that host favorable structures and Quaternary faults, which may not be readily detectable with currently available data in some areas. Furthermore, this adaptation appears as a natural progression for regional modeling based on the results form detailed PFA studies, where vectoring into known favorable structural settings led to the discovery of new Quaternary faults and additional favorable structural settings at a finer scale in Gabbs Valley, Granite Springs Valley, Crescent Valley, Sou Hills, and Steptoe Valley (Craig, 2018; Faulds et al., 2019; McConville et al., 2017; Faulds et al., 2020b; Hinz et al., 2020).

(A) **FEATURE SET 2 INPUT**

Known Geothermal Systems
Temperature C

★ >130 C (benchmarks)
☆ 39.0 - 130.0 C
● Negative Training Sites

High

Low

0   12.5   25   50 Miles
0   15   30   60 Kilometers

N

Study Area
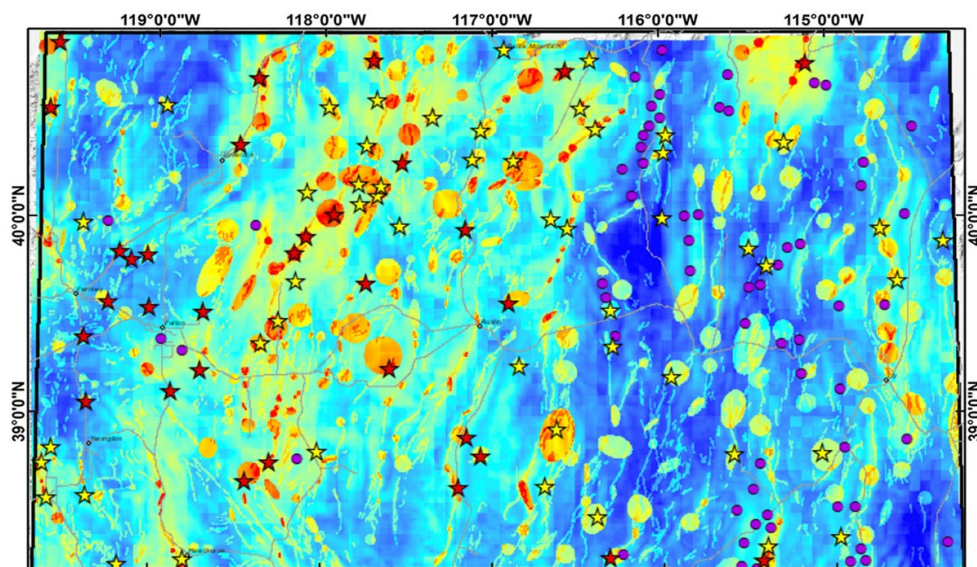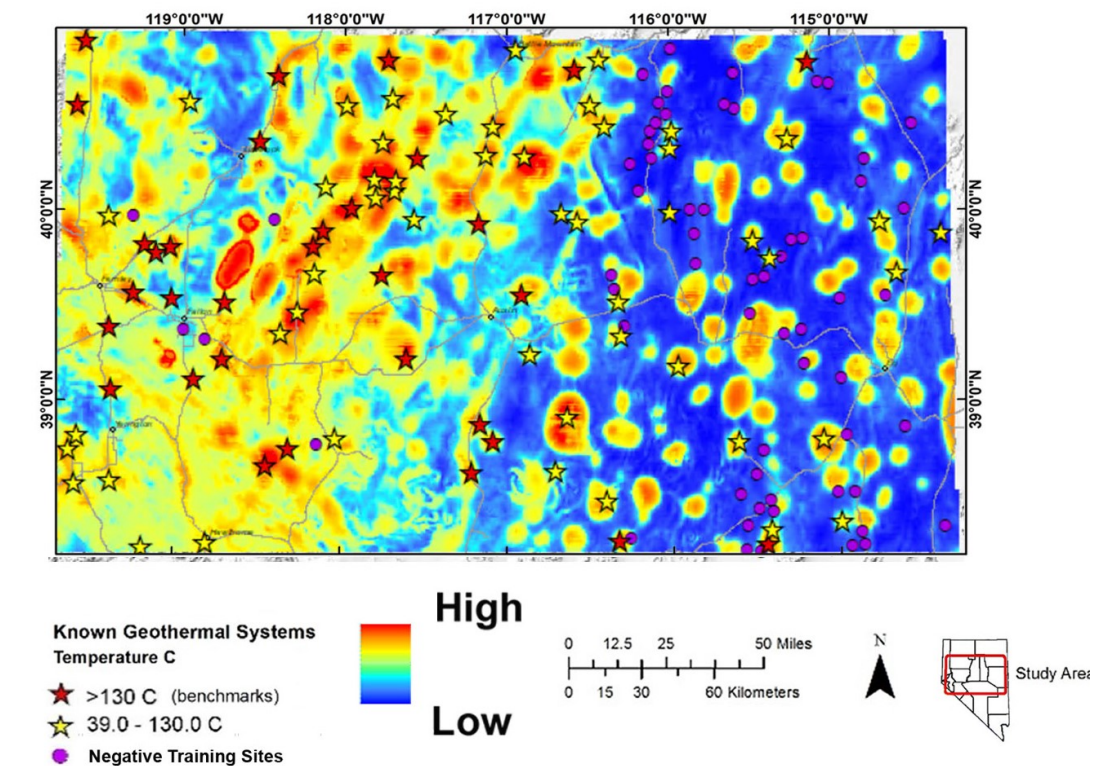
(B) **ORIGINAL PFA FAIRWAY**

Figure 4.6. *Comparison of the (A) feature set one 5th percentile map and (B) the original PFA Fairway model. This map includes the locations of positive (red and yellow stars) and negative (purple triangles) training sites*
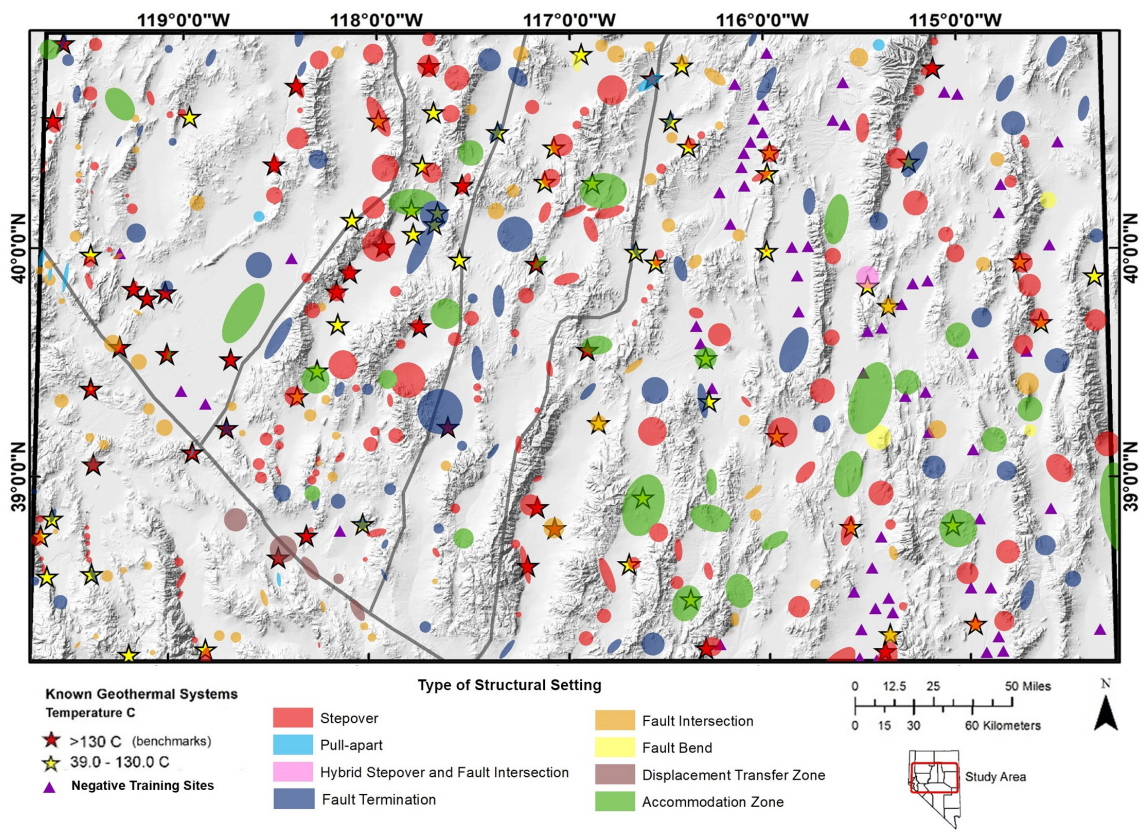
Figure 4.7. *Types of Structural settings with color coding, and the locations of positive (red and yellow stars) and negative (purple triangles) training sites (modified from Faulds et al., 2015a).*

The regional approach of BNN modeling with feature set one appears to hold promise in both facilitating and inducing green-field exploration. To evaluate the applicability of this method, the locations of several recently discovered blind systems in the study area are set against the backdrop of the BNN 50th and 5th percentile maps (Figure 4.8). Two of these sites, southern Gabbs Valley and Granite Spring Valley, were selected for detailed PFA studies based on results from the first phase of the PFA study. The third site, McGinness hills, is a recently discovered blind system (Nordquist and Delwiche, 2013) and the largest producing geothermal field in Nevada, with three 48 MWe power plants installed with a total gross generation capacity of over 150 MWe (Ayling, 2020).

Evaluating the sub-regions around each of these sites from west to east, the Granite Springs Valley area hosts high favorability along most of the main segments of a Quaternary faults bounding the basin, but the grid point and immediately surrounding area of this site hosts moderately positive values in both percentile maps. The southern Gabbs Valley sub-region hosts high favorability throughout in the 50th percentile map, yet as the zones of high favorability become more localized in the 5th percentile map, the grid block and immediately surrounding areas fall into a moderate range of favorability. To the east, the McGinness hills sub-region correlates to an area of moderate favorability. The highest areas of favorability in this sub-region are just to the south in a pattern that closely resembles the product of high horizontal gravity and magnetic gradient values along the main segment of a Quaternary fault. In the 5th percentile map, the zones of elevated geothermal potential along this same segment appear to be more localized, yet

the grid point and immediately surrounding area of this site remain in the moderate range of predictive values.

These results appear to emphasize the importance of additional factors, in particular the locations of favorable structural settings that motivated the greenfield exploration at each of these sites. If basing decisions for greenfield exploration relied solely on this modeling, these three sites would not appear as particularly favorable candidates. It is also notable that their locations along the margins of segments of higher favorability may indicate that elevated geothermal potential in this regional modeling is delineated more so along the main segments of Quaternary faults than the lateral terminations and more subtle discontinuities that characterize fault interaction zones, which host the vast majority of geothermal systems in the Great Basin region.
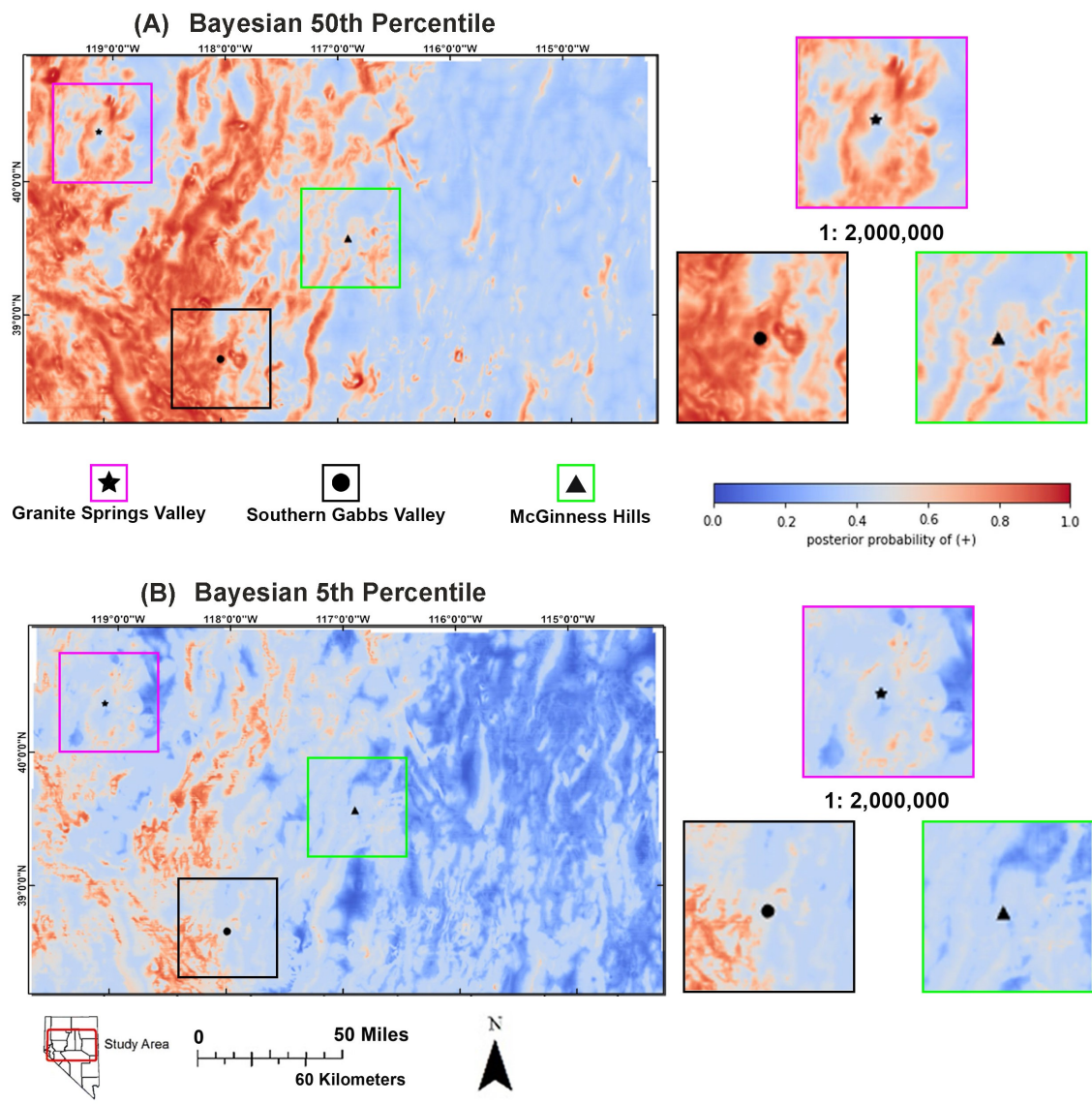
Figure 4.8. *Comparison of predictions at several recently discovered blind systems with the maps from (A) the BNN 50th percentile for feature set one and (B)the BNN 5th percentile map for feature set one. The star represents Granite Springs Valley, the circle denotes southern Gabbs Valley, and the triangle represents McGinness Hills.*

Chapter V. Conclusions and Future Work

The combined application of the PCAk and BNN techniques and new data developments in this study are well suited to mitigate the key data challenges of limited training data, variable data types, and complex feature and label relationships encountered in the PFA and at the onset of this study. Additionally, the PCAk and BNN predictive outputs demonstrate two well constrained and dynamic modeling techniques for evaluating geothermal favorability and organizing complex feature patterns.

The PCAk technique offers new insight into the structure of our data, particularly with the cluster maps for each feature set, which act as a promising guide to interpret feature influence. Furthermore, the PCA reduction isolates the sources of variance in our data, decorrelates/filters noise, and produces reconstructed mixing matrix maps that represent promising alternative inputs to our geologic and geophysical features. The BNN technique offers a dynamic approach for modeling geothermal favorability, where 1) ensemble modeling allows for a distribution of predictions to mitigate the stochastic nature of artificial neural network modeling, and 2) the representation of predictions can be selected from a range of different percentiles from the distribution of modeling predictions. The 5th percentile maps are the preferred representation of the results for each feature set, because they have a very high confidence in the predictive results for each pixel. However, Bayesian modeling also allows for any percentile value to be displayed. This is especially useful for different risk assessments for regional exploration modeling, where projects evaluating broader development factors, such as land status,

may focus on the maps with a broader prediction threshold (e.g., 50th percentile), versus

the high-risk factors, such as the extent of existing detailed geophysical data or presence

of a known favorable structural setting, where results with a degree of confidence may be

preferred (e.g., 5th percentile).

This study identifies the promise of machine learning techniques to support the

growing assemblage of geoscience data. The dual approach of PCAk and BNN

collectively analyzes a large number of features at the same time over an appreciable area

while also accounting for non-linear relationships between different input features.

Furthermore, the comparative analysis of feature set one and two addresses several issues

of particular interest. These include evaluating 1) how to further develop regional

modeling efforts by experimenting with feature sets that combine regional permeability

data with intermediate permeability data (i.e., location of Quaternary faults), and heat;

and 2) how to both incorporate and evaluate the influence of local and intermediate

permeability features in supervised favorability modeling. The results of the BNN

analysis both agree well with the prior PFA while also providing a more dynamics range

of predictions that have promising potential to scale into more localized zones of

favorability.

Future efforts would benefit from 1) designing a more comprehensive training set

collection; 2) exploring additional feature combinations, in particular using

dimensionality reduction methods to combine and decorrelate features, and 3) evaluating

additional methods to integrate categorical data (e.g., favorable structural settings and

Quaternary faults). Additional datasets that would contribute to these efforts include more

detailed potential field geophysical data, as well as LiDAR (light detection and ranging) data, to elucidate the location of undetected faults and favorable structural settings. These data types are especially useful in large basins (e.g., Granite Springs Valley and the Carson Sink in the western half of the study area, or Railroad Valley and Steptoe Valley in the east), where Quaternary basin-fill sediments may cover Quaternary faults. A great deal of insight into feature influence may also be found by performing more localized analysis. Examples isolating the training sites grid points are included below (Appendix A) for an exploratory PCAk analysis, as well as a supervised feature sensitivity analysis, which directly attributes the predictions of a supervised model to its input features by ranking the relative importance of each feature.

Appendix A

Appendix A provides ancillary data and results derived from the techniques presented above with feature sets one and two. This includes training site metadata, correlation matrices at training sites and for the full extent of the PFA study area, additional PCAk analysis for the PFA study area, PCAk results with training sites, and BNN feature sensitivity analysis with training sites.

The codes used in this study are made available for public usage at Nevada Bureau of Mines and Geology · GitHub (designed to be readily implemented for users

with a modest level of programming knowledge). The reader can deepen their

understanding of the algorithms by tuning the parameters of the algorithm and by

examining the details of the code. Many of these codes have been written by my team

members on my project. Without their contributions this work would not have been

possible.

Training Site Metadata

The locations and major attributes of positive (Figure A1 and Table A1) and negative

(Figure A2 and Table A2) training sites are organized below.

Name	ID	X_83UTM11	Y_83UTM11	Temp. [◦C]	Blind Status	Fairway (38 - 65)	FS 1 BNN 5th Percentile (0-1)	FS2 BNN 5th Percentile (0-1)	Average (BNN Scores + PFA) (0 - 1)
Beowawe	0	533578	4489964	227	no	58.33	0.453	0.607	0.653
Dixie Valley	1	426828	4423464	250	no	57.97	0.515	0.563	0.657
Kyle Hot Springs	2	295578	4473464	124	no	51.82	0.713	0.554	0.688
Desert Queen	3	327578	4406464	155	yes	53.72	0.591	0.529	0.649
Desert Peak	4	333078	4402714	219	yes	43.94	0.442	0.475	0.531
Bartine Hot Springs	5	341078	4380464	62	no	45.67	0.402	0.382	0.495
Stillwater	6	366328	4378464	178	yes	47.81	0.442	0.434	0.537
Rye Patch	7	392328	4486964	224	yes	54.55	0.701	0.577	0.706
Wabuska	8	311578	4336714	146	no	46.26	0.627	0.549	0.629
Darroughs Hot Springs	9	484328	4296464	145	no	53.89	0.519	0.546	0.632
Paris Well	10	383578	4455714	63	yes	52.38	0.408	0.646	0.620
Leach Hot Springs	11	445078	4494964	169	no	57.19	0.721	0.673	0.758
Bacon Flat	12	626328	4262714	130	yes	52.77	0.464	0.550	0.609
Sulphur Hot Springs	13	645078	4494214	182	no	57.70	0.423	0.495	0.602
Gerlach	14	299828	4503964	192	no	54.96	0.517	0.505	0.623
Hawthorne 1	15	356328	4263214	97	yes	56.02	0.554	0.515	0.644
Peterson	16	452578	4351714	150	no	53.41	0.629	0.577	0.676
Dixie Comstock	17	413578	4412964	196	no	62.84	0.776	0.645	0.796
McCoy	18	457078	4417964	122	yes	38.55	0.426	0.268	0.429
Lee-Allen Hot Springs	19	351078	4341464	171	no	50.45	0.433	0.468	0.559
McGinness Hills	20	320328	4383714	192	yes	45.23	0.718	0.568	0.660

Hot Creek Ranch Hot Spr	21	555078	4263714	160	no	48.75	0.403	0.513	0.556
Rawhide-Wedell Hot Spring	22	396328	4308464	151	no	45.98	0.527	0.462	0.565
Walti Hot Springs	23	679578	4417464	83	no	52.37	0.376	0.533	0.572
Clan Alpine Ranch	24	688078	4393214	70	yes	47.60	0.318	0.508	0.519
Smith Ranch	25	635328	4456964	72	no	46.92	0.180	0.561	0.488
Klobe Hot Spring	26	556078	4361964	86	no	34.31	0.405	0.400	0.444
Bruffey's Hot Springs	27	579328	4452464	72	no	50.26	0.242	0.281	0.432
near Dann Ranch	28	548078	4462964	86	no	62.05	0.580	0.539	0.691
Empire - San Emidio	29	541078	4472964	190	no	58.02	0.622	0.527	0.681
Spencer Hot Springs	30	512328	4353214	95	no	43.81	0.250	0.441	0.455
Shipley Hot Springs	31	527078	4421214	55	no	49.32	0.189	0.239	0.396
Buffalo Valley Hot Spring	32	472328	4468714	128	no	52.24	0.441	0.516	0.587
Crescent Valley Hot Sprgs	33	424828	4473214	87	no	54.65	0.462	0.591	0.631
Sou Hot Springs	34	438078	4437714	85	no	54.08	0.673	0.715	0.740
Eleven Mile Canyon	35	392828	4363714	82	yes	53.68	0.522	0.526	0.625
Pirouette Mount (Dixie Valley)	36	400578	4373964	87	yes	52.61	0.624	0.682	0.705
Wilson Hot Spring	37	311078	4293214	94	no	51.74	0.549	0.504	0.617
Diana's Punch Bowl-Potts Ranch	38	529828	4323464	74	no	49.48	0.345	0.675	0.594
Spring & Test hole Uce 10	39	549078	4283214	42	no	46.15	0.411	0.491	0.537
Blue Eagle Springs	40	628328	4269214	41	no	54.21	0.469	0.529	0.611
Moorman	41	662078	4273464	45	no	46.17	0.402	0.438	0.517
Williams Hot Springs	42	612578	4311964	123	no	44.56	0.402	0.515	0.534
Fish Creek Springs	43	583078	4347964	45	no	42.35	0.386	0.583	0.540
Warm Springs Ranch-Newark Valley	44	619328	4407714	42	no	40.40	0.262	0.462	0.448
Alligator Ridge well	45	627328	4399714	44	yes	45.31	0.296	0.467	0.487
Hot Springs Point	46	579078	4421714	128	no	39.25	0.197	0.062	0.288
Grant View Hot Springs	47	325828	4261214	53	no	34.88	0.461	0.398	0.465
Valley of the Moon	48	490828	4448964	56	no	52.91	0.559	0.594	0.656
Mound Spring	49	494578	4462714	54	no	53.95	0.448	0.581	0.620
Unnamed Hot Pool-Carico Valley	50	509828	4448464	50	no	51.27	0.438	0.708	0.645
McLeod Hot Spring	51	488078	4319714	134	no	48.68	0.414	0.479	0.547
Duckwater Area	52	494828	4311464	45	no	46.34	0.415	0.531	0.553
Big Blue	53	653078	4312714	155	no	42.78	0.402	0.603	0.554
Gene Sawyer well	54	295328	4315214	84	yes	44.92	0.489	0.497	0.559
Jersey Valley Hot Springs	55	458078	4447714	166	no	56.97	0.543	0.589	0.669
Mosquito Ranch Springs	56	524578	4297214	73	no	47.69	0.431	0.468	0.544
Ambassador Well	57	418578	4312964	110	yes	52.98	0.410	0.447	0.557
Spring Valley Well	58	709078	4411714	79	yes	36.31	0.155	0.041	0.252
Wellington Well	59	293328	4292214	83	yes	47.99	0.701	0.482	0.641
Horseshoe Ranch Spr	60	545328	4495214	77	no	50.04	0.406	0.529	0.568
Soda Lake	61	554828	4378964	216	yes	38.76	0.215	0.463	0.425
Battle Mountain City Well	62	505328	4499714	89	yes	38.87	0.177	0.131	0.302

Name	ID			Temp.	Blind	Fairway	FS 1 BNN 5th Percentile	FS 2 BNN 5th Percentile	Average (BNN Scores +PFA)
Cherry Creek Hot Springs	63	487578	4416464	102	no	48.43	0.433	0.486	0.555
Bach Well	64	350078	4474714	78	yes	34.73	0.459	0.460	0.484
Coyote Spring - Pleasant Valley NV	65	446828	4476714	64	no	43.70	0.459	0.467	0.533
Colado	66	442328	4455464	155	yes	41.25	0.765	0.554	0.651
Bradys	67	340328	4405214	212	no	48.86	0.537	0.516	0.602
Tungsten Mountain	68	408828	4392464	176	yes	42.62	0.492	0.518	0.555
New York Canyon	69	414328	4433714	75	yes	42.90	0.702	0.402	0.588
Salt Wells	70	364578	4351214	188	no	57.56	0.718	0.590	0.731
Hind's-Nevada Hot Springs	71	290828	4308214	80	no	61.71	0.579	0.596	0.708
Reese River	72	535078	4416964	150	yes	51.30	0.498	0.513	0.600
Carlotti Ranch Springs	73	580328	4460714	39	no	51.80	0.339	0.511	0.549
Patua Hot Springs	74	508078	4382214	182	no	48.12	0.407	0.466	0.538
Black Warrior	75	310828	4419964	128	yes	41.89	0.481	0.444	0.523
Monte Neva Hot Springs	76	441328	4391714	111	no	55.48	0.498	0.545	0.632
Silver Springs	77	310578	4366714	149	yes	39.99	0.613	0.424	0.551
Dixie Meadows	78	408328	4405464	145	no	61.27	0.851	0.680	0.825
Hyder Hot Spring	79	438578	4428214	84	no	43.34	0.609	0.526	0.601
Western Augusta Mtn Hot Springs	80	447078	4432214	40	no	57.63	0.790	0.671	0.783
McCoy Hot Springs	81	448328	4436714	49	no	56.41	0.597	0.703	0.722
Wild Rose/Don Campbell	82	385078	4299714	151	yes	51.85	0.631	0.648	0.692

Table A1. Compiled positive training sites. Name = Geothermal Site, ID = Generic identification number, Temp.[◦C]= maximum temperature from geochemistry or well temperature. Blind = Distinction if system is blind or not. Fairway = fairway score (Faulds et al., 2015a), FS 1 BNN 5th Percentile (0-1) = Scores from the feature set one Bayesian 5th percentile map, FS 2 BNN 5th Percentile (0-1) = Scores from the feature set two Bayesian 5th percentile map; Average (BNN Scores +PFA) = average score of the BNN models (feature sets one and two) and the PFA values (converted to 0-1). The top 10% of site scores are highlighted red, and the bottom 10% of site scores are highlighted blue.
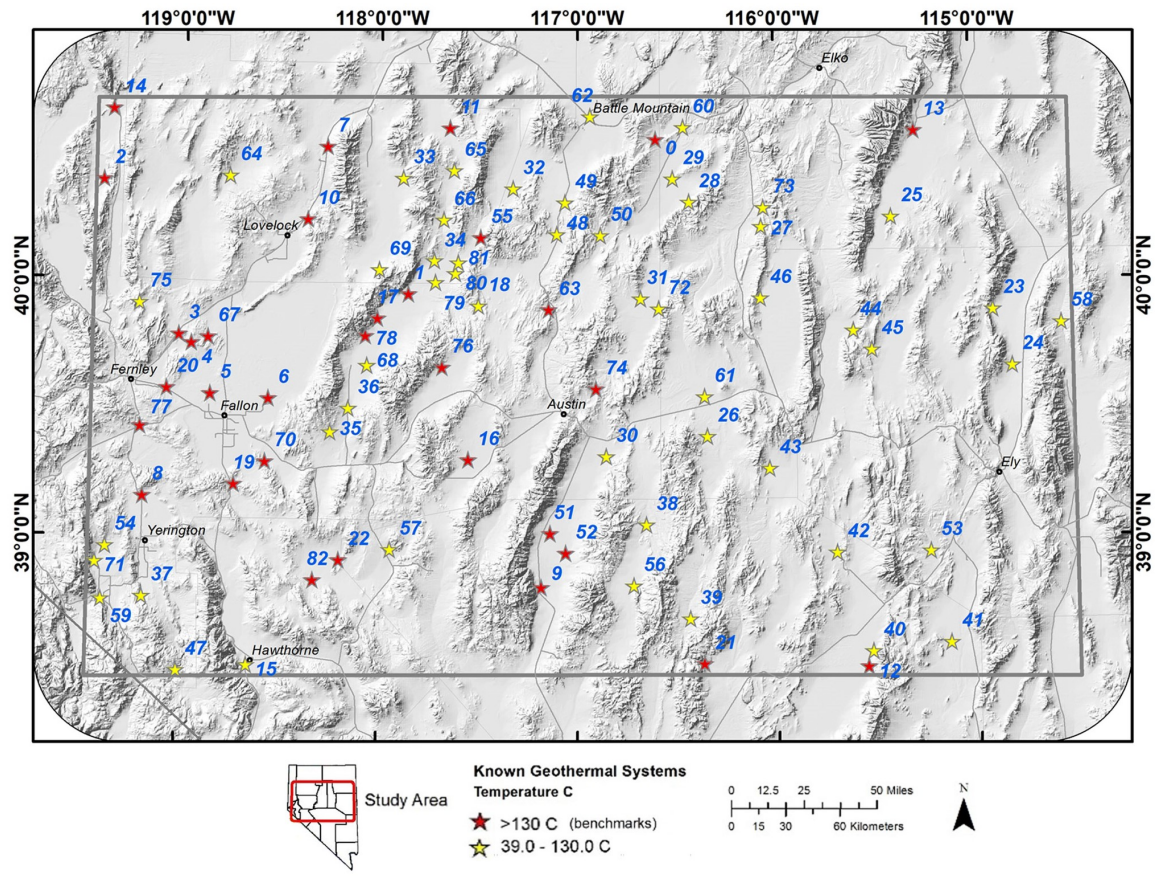
Figure A1. *Map of positive training sites with ID numbers (0-82). Red stars are systems >130°C, yellow stars are systems 37°C-130 °C.*

NAME	ID	X_83UTM11	Y_83UTM11	Δ Temp. [°C]	Depth(m)	Fairway (38 - 65)	FS 1 BNN 5th Percentile (0-1)	FS 2 BNN 5th Percentile (0-1)	Average (BNN Scores + PFA) (0 - 1)
Steptoe Federal No. 17-14	0	691327.69	4423963.77	-5.06	3568.90	38.27	0.187	0.059	0.278
U.S.A. Jiggs No. 1	1	610077.69	4471713.77	-60.85	4143.76	38.21	0.137	0.042	0.256
Three Bar Federal No. 24-13A	2	570077.69	4460213.77	-40.39	3845.66	36.88	0.247	0.054	0.289
FRANKLIN #1	3	649577.69	4484713.77	-81.91	3995.70	45.53	0.155	0.084	0.313
Standard-Amoco-S.P. Land Co. No. 1	4	390327.69	4418463.77	-32.26	3352.80	40.41	0.406	0.339	0.455
East Bailey Ranch No. 1	5	574077.69	4473963.77	-17.07	2740.76	37.89	0.212	0.050	0.282

Jiggs No. 10-1	6	605327.69	4473463.77	-35.80	2830.68	38.59	0.135	0.028	0.252
Tommy Knocker Unit No. T61X-33G	7	643077.69	4409713.77	-49.52	3546.65	40.95	0.349	0.066	0.349
Pine Creek No. 1-7	8	572577.69	4464713.77	-36.71	2956.56	36.52	0.206	0.055	0.274
Huntington Creek No. 1	9	609327.69	4488463.77	-15.07	2209.80	41.35	0.076	0.019	0.244
Duck Creek No. 1	10	682077.69	4381713.77	-59.81	2825.80	50.04	0.396	0.492	0.553
Diamond Valley Federal No. 1-24	11	589077.69	4422963.77	-12.50	2707.84	33.63	0.135	0.070	0.241
Nevada """"""""""DK"""""""""" Federal No. 1	12	622827.69	4258963.77	-10.28	2193.34	49.41	0.416	0.464	0.547
Hot Creek Federal No. 24-13	13	560827.69	4265213.77	-25.34	2956.56	50.03	0.403	0.486	0.553
Federal No. 1-5	14	671077.69	4436713.77	-61.97	3208.63	35.83	0.201	0.099	0.284
Southern Pacific Land Co. No. 2-27	15	577577.69	4468463.77	-38.19	2644.44	40.09	0.304	0.074	0.332
Blue Eagle No. 1	16	629077.69	4277963.77	-40.06	2747.47	43.23	0.417	0.154	0.412
Silver State Federal No. 33-18	17	552827.69	4384713.77	-15.27	2773.98	33.71	0.190	0.273	0.327
Palisades No. 1	18	566327.69	4487713.77	-30.22	2897.43	40.64	0.392	0.085	0.367
Ruby Valley Unit No. 1	19	654827.69	4483713.77	-64.32	2743.20	41.56	0.075	0.052	0.256
Big Pole Creek No. 1-11	20	569077.69	4454713.77	-40.09	2503.02	38.59	0.197	0.043	0.278
Reggie No. 1	21	346577.69	4365713.77	-13.77	1879.09	39.96	0.402	0.265	0.427
White River Valley No. 1	22	666327.69	4262213.77	-37.09	3183.64	41.73	0.395	0.086	0.375
Shields Federal No. 13-22	23	663827.69	4315213.77	-60.54	2781.91	37.65	0.288	0.180	0.349
Federal No. 1-4	24	671827.69	4447963.77	-67.12	2764.23	39.37	0.199	0.094	0.300
White River No. 2	25	668077.69	4287713.77	-19.78	2307.34	38.36	0.389	0.095	0.358
Twin Springs Federal No. 10-6	26	557327.69	4366963.77	-17.29	2446.63	33.64	0.233	0.100	0.284
Anderson D. Federal No. 1	27	616077.69	4259963.77	-26.97	2167.43	38.89	0.151	0.137	0.295
Currant No. 1	28	627577.69	4283713.77	-33.18	2375.61	38.81	0.397	0.114	0.370
Long Valley No. 35-88	29	637077.69	4408463.77	-30.51	2155.24	38.89	0.181	0.032	0.270
Currie Federal No. 1	30	694577.69	4464963.77	-54.11	2621.58	36.10	0.196	0.060	0.270
Long Jevity Federal No. 1	31	632577.69	4400463.77	-31.36	2389.33	37.19	0.200	0.075	0.283
Federal White Pine Unit No. 1	32	642077.69	4365463.77	-68.25	3374.75	33.55	0.230	0.059	0.269

Gose """"""""BZ"""""""" Federal """"""""A"""""""" No. 1	33	673077.69	4262713.77	-13.58	2134.21	40.51	0.404	0.119	0.382
Titan Federal No. 1-9	34	692077.69	4319463.77	-65.99	2347.26	40.81	0.382	0.074	0.361
Jackpot Federal No. 1	35	564577.69	4432213.77	-37.85	2507.59	31.91	0.123	0.039	0.218
Three Bar Federal No. 36-C	36	570327.69	4447463.77	-33.07	2076.60	34.84	0.157	0.042	0.245
S.P. Land Company No. 1-23	37	577827.69	4479463.77	-44.71	2177.49	39.46	0.326	0.122	0.352
Duckwater Creek No. 8-12	38	622327.69	4279463.77	-32.58	2101.29	40.35	0.209	0.081	0.304
Roulette No. 1	39	613827.69	4285963.77	-29.26	2087.88	36.52	0.342	0.058	0.321
Moorman Ranch Unit No. 2	40	643577.69	4349463.77	-38.06	2380.18	46.14	0.290	0.417	0.472
Quartz Road Federal No. 1	41	560327.69	4444713.77	-69.09	2768.19	36.43	0.149	0.038	0.249
Yankee Mine Unit Federal No. 27-23X	42	624577.69	4307963.77	-59.04	2033.02	37.94	0.280	0.055	0.306
Giroux Wash No. 1-29	43	661077.69	4342713.77	-38.22	2242.11	35.39	0.218	0.063	0.275
Black Point No. 6-41	44	591827.69	4397213.77	-28.22	2619.76	38.34	0.321	0.096	0.336
Gose """"""""DL"""""""" Federal No. 1	45	671327.69	4268463.77	-23.34	2154.02	38.01	0.296	0.164	0.348
Diamond Valley Unit No. 1	46	591327.69	4411713.77	-33.86	2450.59	37.84	0.218	0.081	0.294
Marathon-Anadarko Keno Unit No. 23-33	47	617577.69	4373213.77	-29.69	2225.04	41.23	0.194	0.443	0.424
Koch No. 2-29	48	621077.69	4295713.77	-37.72	2078.74	37.42	0.170	0.041	0.262
Saguaro Unit No. 1	49	711577.69	4271463.77	-38.64	2112.26	35.54	0.337	0.105	0.330
Cove Unit No. 1-18	50	660327.69	4287713.77	-38.58	2168.96	38.91	0.254	0.239	0.364
Bonanza Federal No. 1-32	51	660827.69	4380963.77	-54.76	2088.49	38.87	0.206	0.058	0.287
Buck Mountain Unit No. 36-1	52	619327.69	4389713.77	-42.28	2381.71	33.12	0.191	0.034	0.245
Willow Wash Federal No. 42-24	53	551077.69	4391713.77	-42.49	2386.89	38.83	0.319	0.178	0.365
Petan Trust F-12-19-P	54	579077.69	4500213.77	-61.96	2759.96	31.73	0.149	0.034	0.224
Gigante No. 1-4	55	409577.69	4310213.77	-36.08	1583.44	40.97	0.478	0.397	0.502
Illipah Federal No. 1	56	634077.69	4363713.77	-58.31	2318.61	33.02	0.277	0.280	0.355
Lockes Unit No. 1	57	616827.69	4271213.77	-63.09	2232.36	40.64	0.130	0.049	0.268

Diamond Federal 11-22	58	595577.69	4423213.77	-56.03	2260.09	38.67	0.387	0.099	0.360
Duckwater Federal No. 9-1	59	624577.69	4390963.77	-42.25	2161.03	34.00	0.143	0.026	0.231
82-36	60	356327.69	4360713.77	0.00	2742.74	44.64	0.597	0.429	0.571
Fireball Ridge	61	322077.69	4420463.77	0.00	0.00	41.92	0.464	0.480	0.530

Table A2. Compiled negative training sites. Name =Well name/site name, ID = Generic identification number, △ Temp.[∘C]= Difference between well bottom hole temperature and predicted geothermal gradient, Depth = Well depth, Fairway = fairway score (Faulds et al., 2015a), FS1 BNN 5th Percentile (0-1) = Scores from the feature set one Bayesian 5th percentile map, FS2 BNN 5th Percentile (0-1) = Scores from the feature set two Bayesian 5th percentile map, Average (BNN scores + PFA)= average score of the BNN models (feature sets one and two) and the PFA values (converted to 0-1) . The top 10% of site scores are highlighted red, and the bottom 10% of site scores are highlighted blue
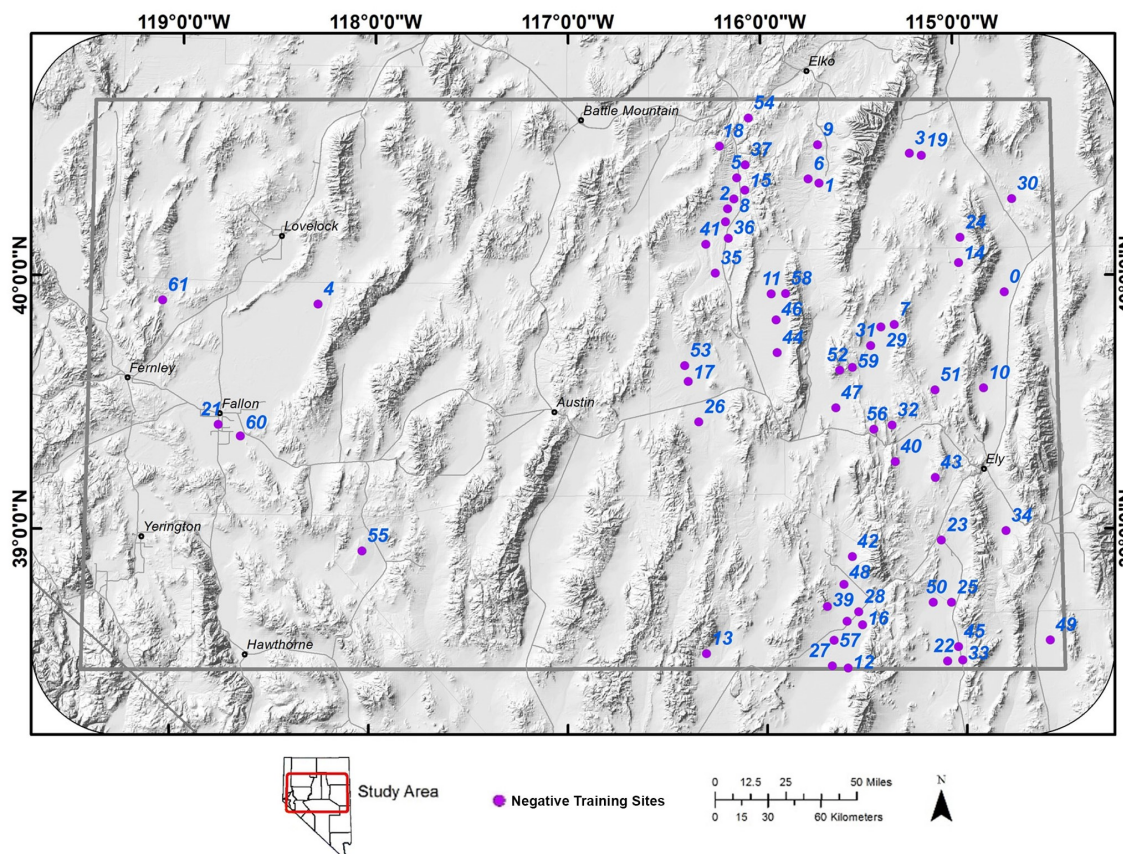
Figure A2. Map of negative training sites with ID numbers (0-61).

Correlation Matrices

This section includes Pearson (e.g., Benesty et al. 2009) correlation matrices for feature sets one and two isolating grid points at the full suite of PFA study area (Figure A3 and Figure A4) and grid points at training sites (Figure A5 and Figure A6). A matrix of the Pearson correlation indicates which of the features are most strongly correlated. The sign of the correlations indicates whether variables are directly (positive) or inversely (negative) correlated with one another.
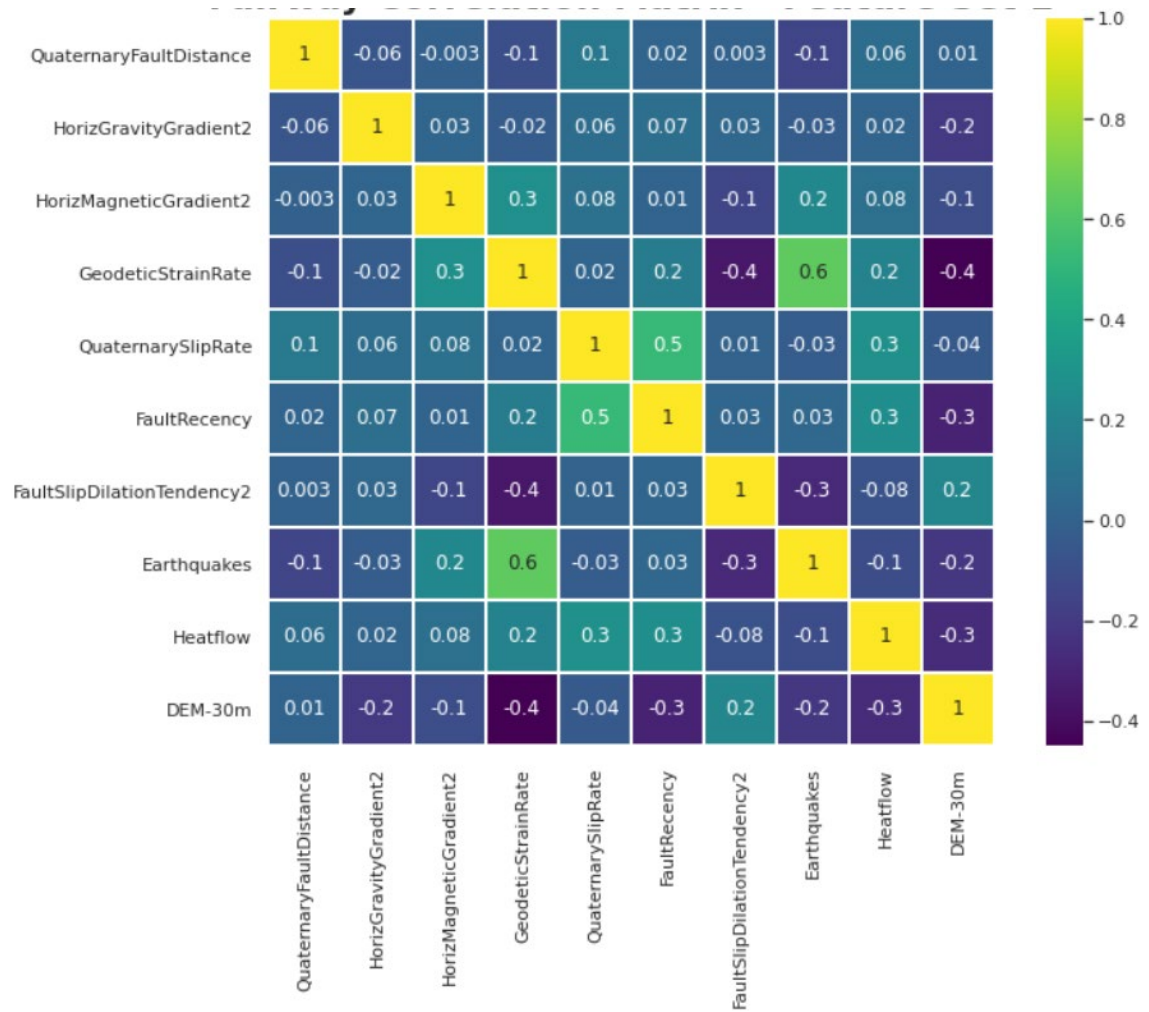
Figure A3. *Feature set one Pearson correlation matrix.*

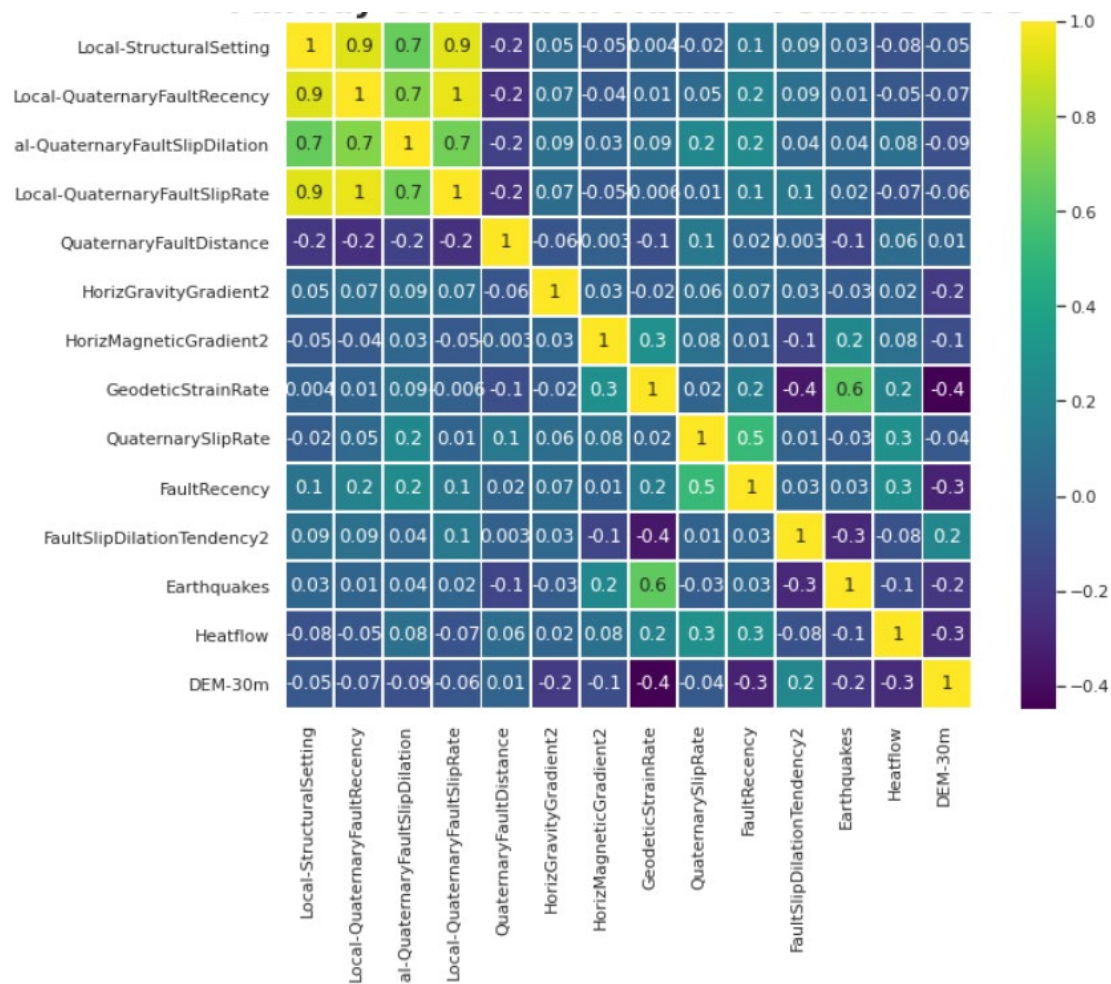***Figure A4.*** *Feature set two Pearson correlation matrix.*
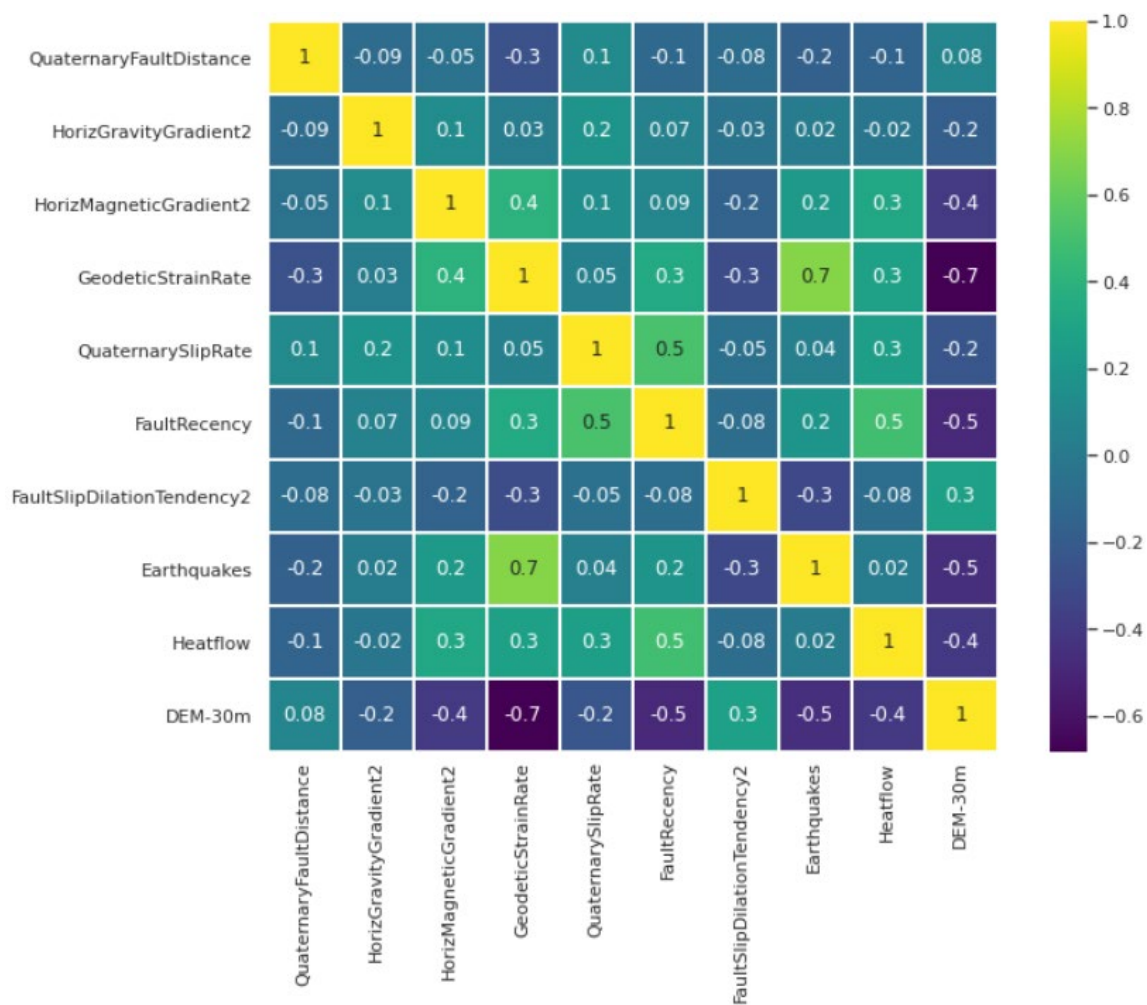
Figure A5. *Feature set one training site Pearson correlation matrix.*
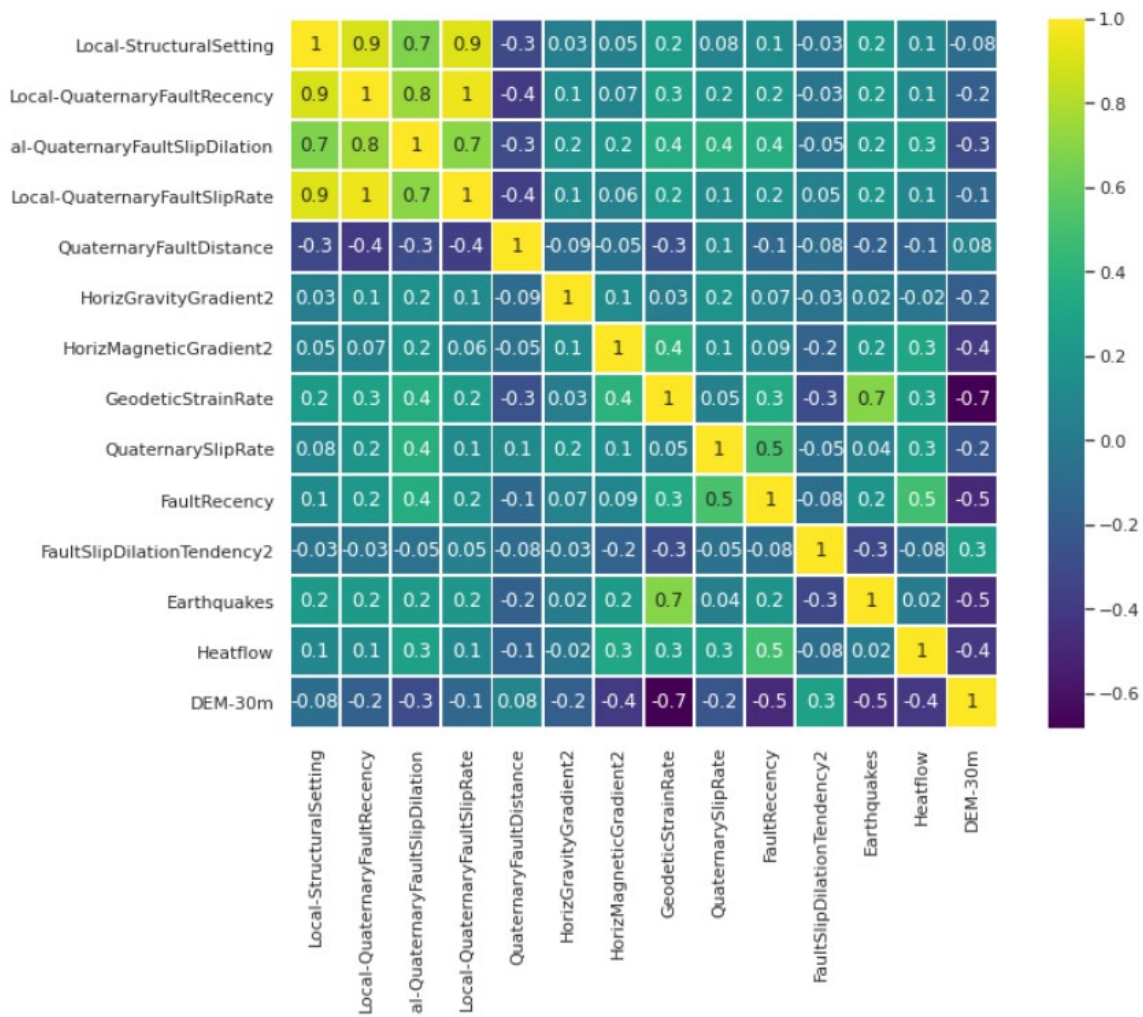
Figure A6. *Feature set two training site Pearson correlation matrix.*

Additional Fairway PCAk Data

This section includes additional figures of the composite maps for PC1-PC3 of the full

PFA study area with the two principal feature sets presented in section 2.1. The mixing

matrix maps for PC1-3 are combined into a single image for feature set one (Figure A7)

and feature set two (Figure A8) by color coding the highest values of each PC to

represent each channel of the red-green-blue (RGB) color ramp (i.e., PC1:red, PC2:

green, and PC3: blue). These images show strong agreements with the PCAk cluster

maps for both feature sets and the gradient displayed on the RGB color ramp appears to

provide additional insights into the mixing of each PC that is not readily defined in the

solid color representation of each PCAk cluster group.

Figure A7. *Feature set one PC 1-3 RGB composite color map (PC1 ~ red, PC2 ~ green, PC3 ~ blue).*

Figure A8. *Feature set two PC 1-3 RGB composite color map (PC1 ~ red, PC2 ~ green, PC3 ~ blue).*

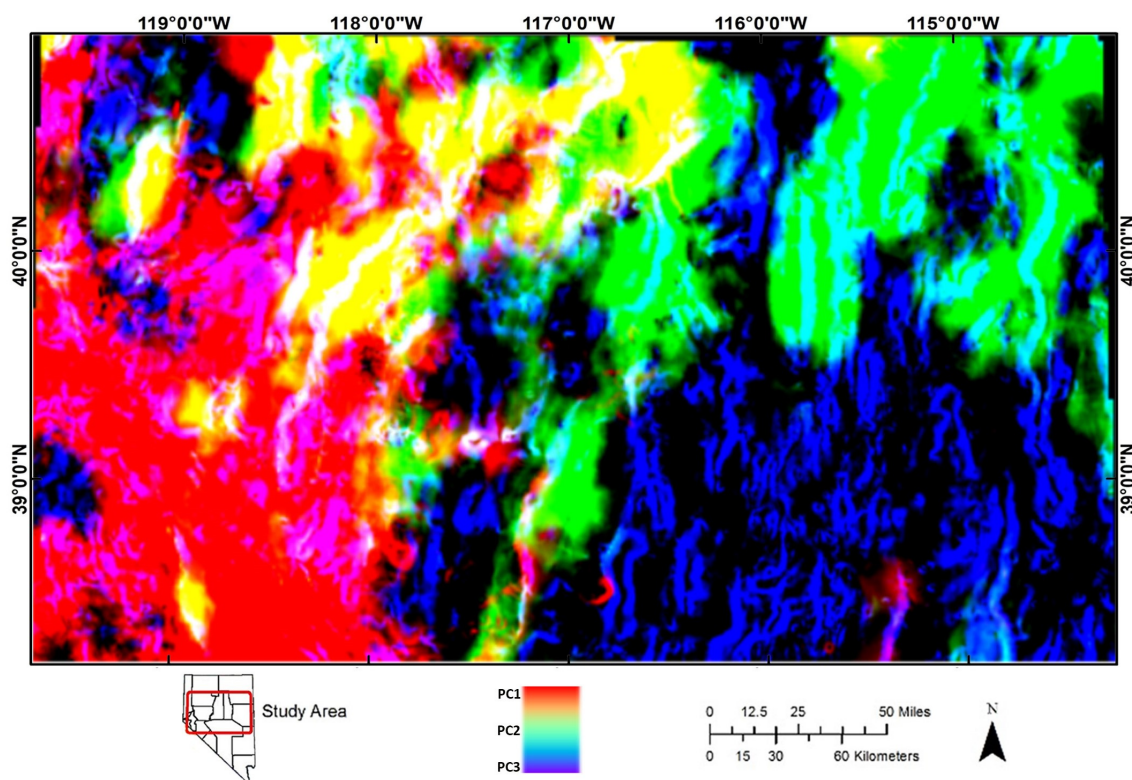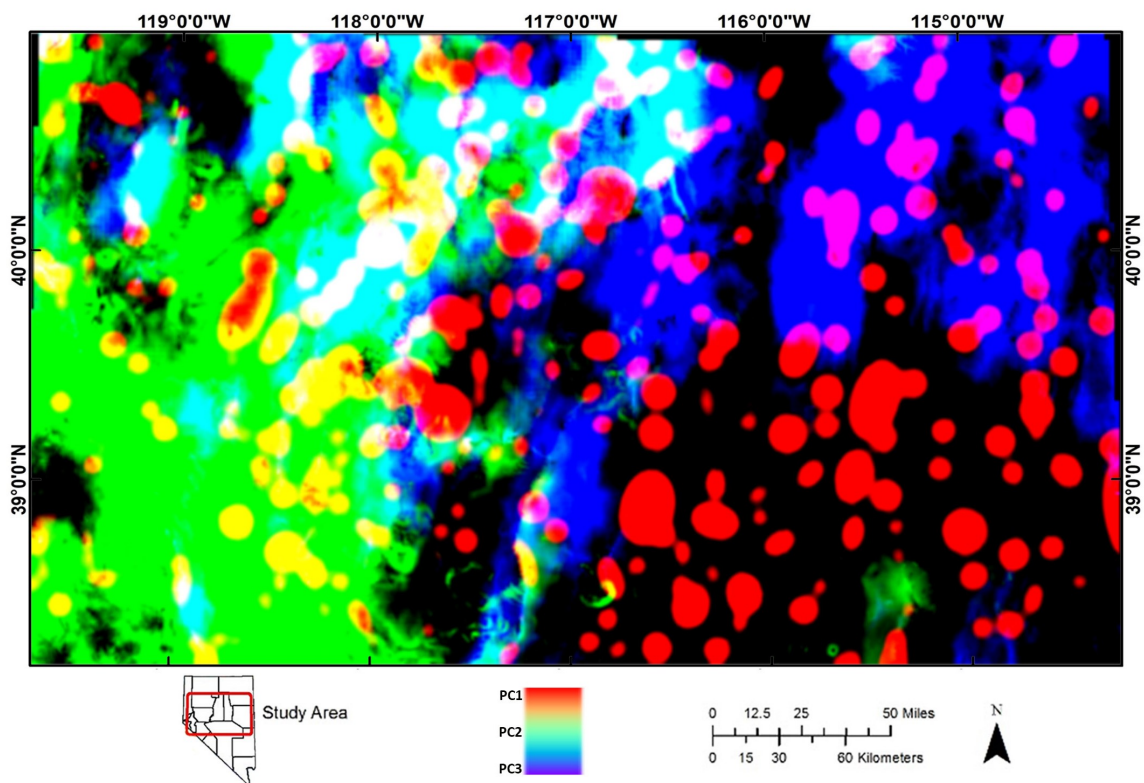**Training site PCAk Plots**

This section includes PCAk analysis of the 83 positive and 62 negative training sites.

With PCA the number of PCs considered for each feature set analysis was selected to be

four which combine to account for 75.65% and 68% of the total explained variance for feature sets one and two, respectively.

Feature set one results (Figure A9 and Figure A10) indicate that cluster-1 (pink) training sites are predominantly located in the western domains, especially the central Nevada seismic belt (CNSB). Most training sites in this cluster are known geothermal systems and directly correlated to geodetic strain rate, earthquakes, heatflow, fault recency, and inversely correlated to dem-30m values. Cluster-2 training sites (green) are located mostly in the carbonate aquifer domain. Cluster-2 hosts a balanced mix of positive and negative sites and is primarily controlled by direct correlations to horizontal gravity gradient and Quaternary fault slip rate. Cluster-3 training sites (blue) are also predominantly located in the carbonate aquifer domain. Most sites in this cluster are negative and directly correlated to DEM-30m (higher elevation), and inversely correlated to every other permeability features besides fault slip and dilation tendency.

Figure A9. *Feature set one training site (A) PCAk plot of explained variance for each component; (B) within group sum of squares plot for different cluster values; and (C) PC1 PC2 biplot with color-coded k-means cluster groups, stars being positive training sites and circles being negative training site.*

Figure A10. Feature set one training site PCAk cluster map of the study area and PCAk feature score matrix (the sum of loadings at the center point of each cluster for PC1-4) for three cluster groups. The PCAk feature matrix is used to reference the influence of each feature in the spatial distribution for each cluster group. Acronyms for the labeled domains in the cluster map include: WGB = western Great Basin, WL = Walker Lane, CNSB = central Nevada seismic belt, CA = carbonate aquifer.

Feature set two results (Figure A11 and Figure A12) indicate that cluster-1 (pink) training sites are distributed heterogeneously across the study area. Most training sites in this cluster are known geothermal systems and are directly correlated to local permeability features and horizontal gravity gradient, and inversely correlated to Quaternary fault distance. Cluster-2 training sites (blue) are located mostly in the carbonate aquifer domain. Most training sites in Cluster-2 are negative and this cluster group is primarily controlled by inverse correlations to local permeability and horizontal gravity gradient and a direct correlation to Quaternary fault distance. Cluster-3 training sites (green) are distributed heterogeneously across the study area like cluster-1. All training sites in this cluster are positive and have strong direct correlations to local permeability features, horizontal gravity gradient, geodetic strain rate, heatflow, fault recency, Quaternary slip rate, and inverse correlations to Quaternary fault distance and DEM-30m.
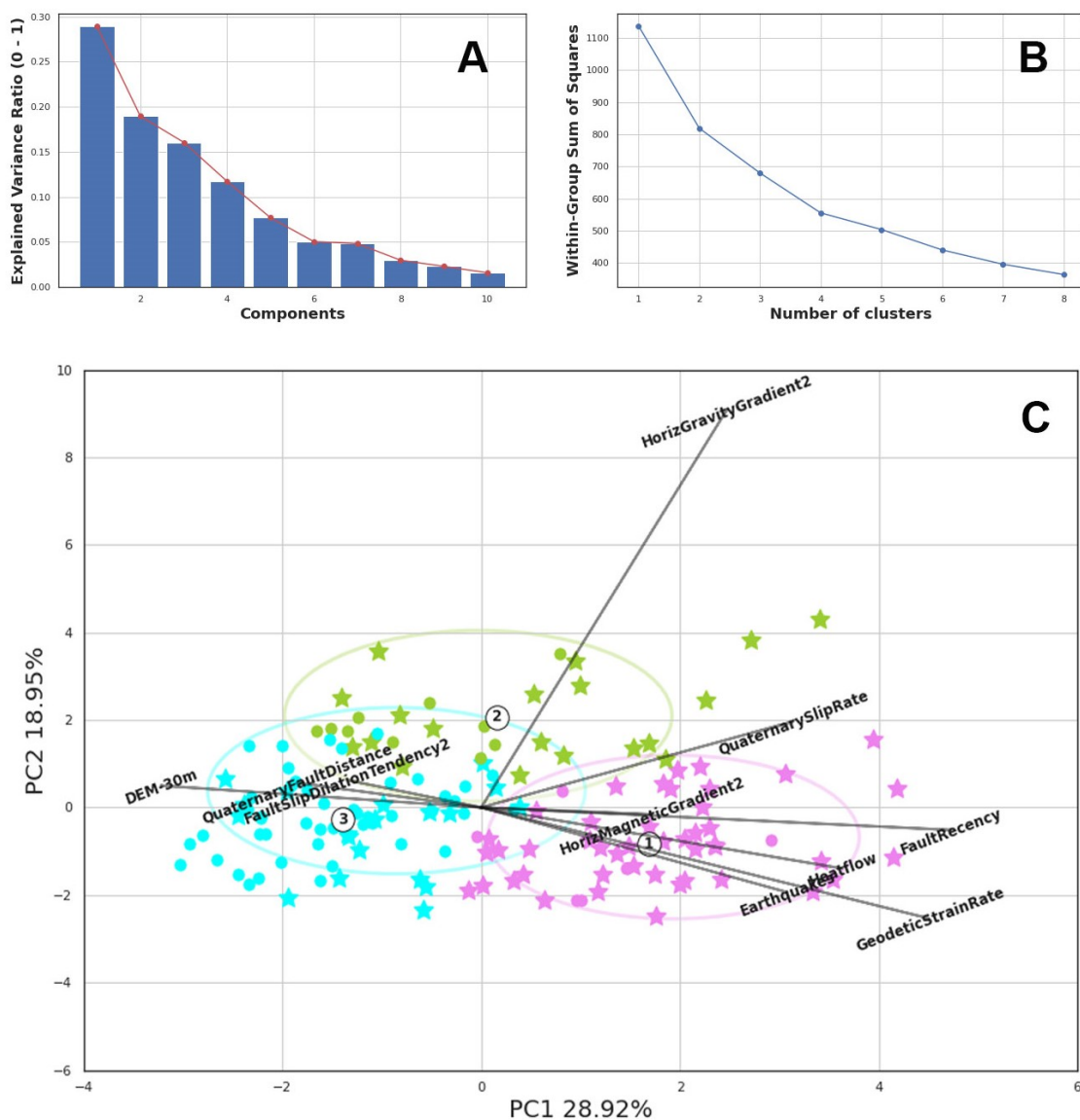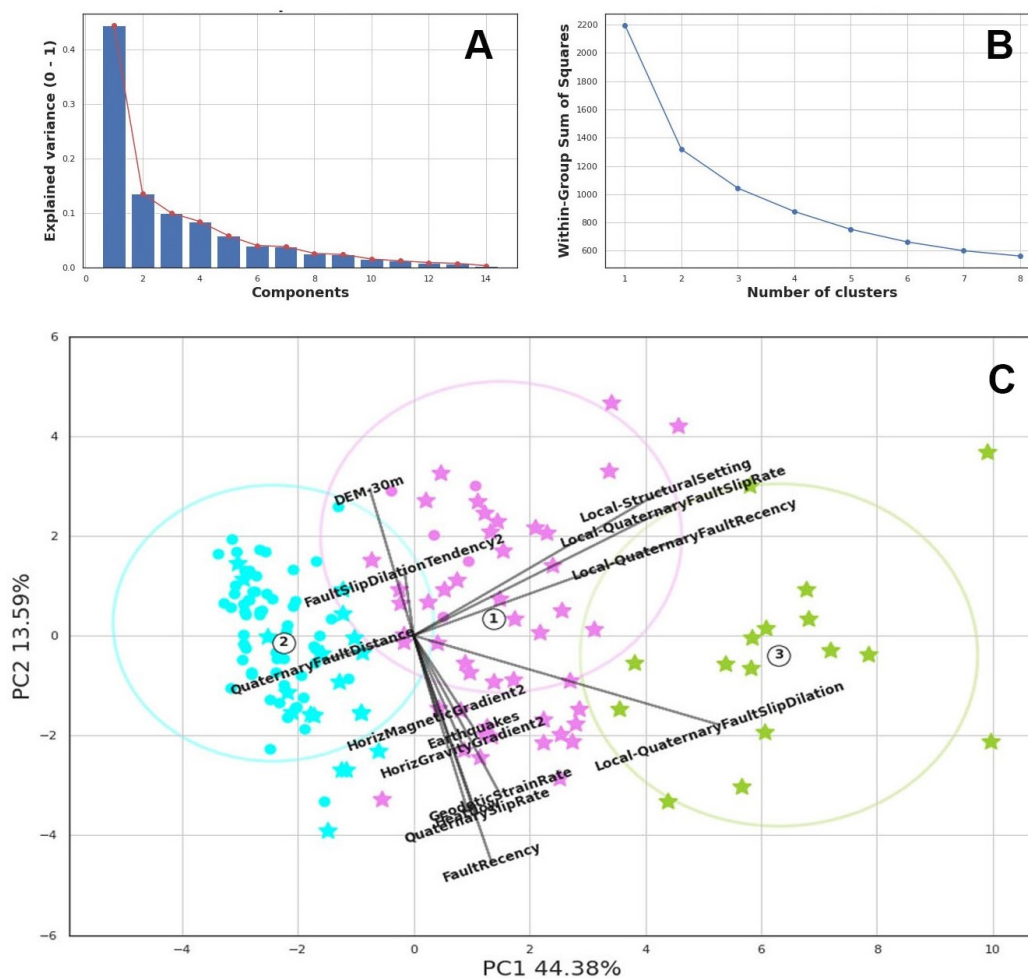
Figure A11. *Feature set two (A) PCAk plot of explained variance for each component; (B) within group sum of squares plot for different cluster values; and (C) PC1 PC2 biplot with color-coded k-means cluster groups, stars being positive training sites and circles being negative training site.*
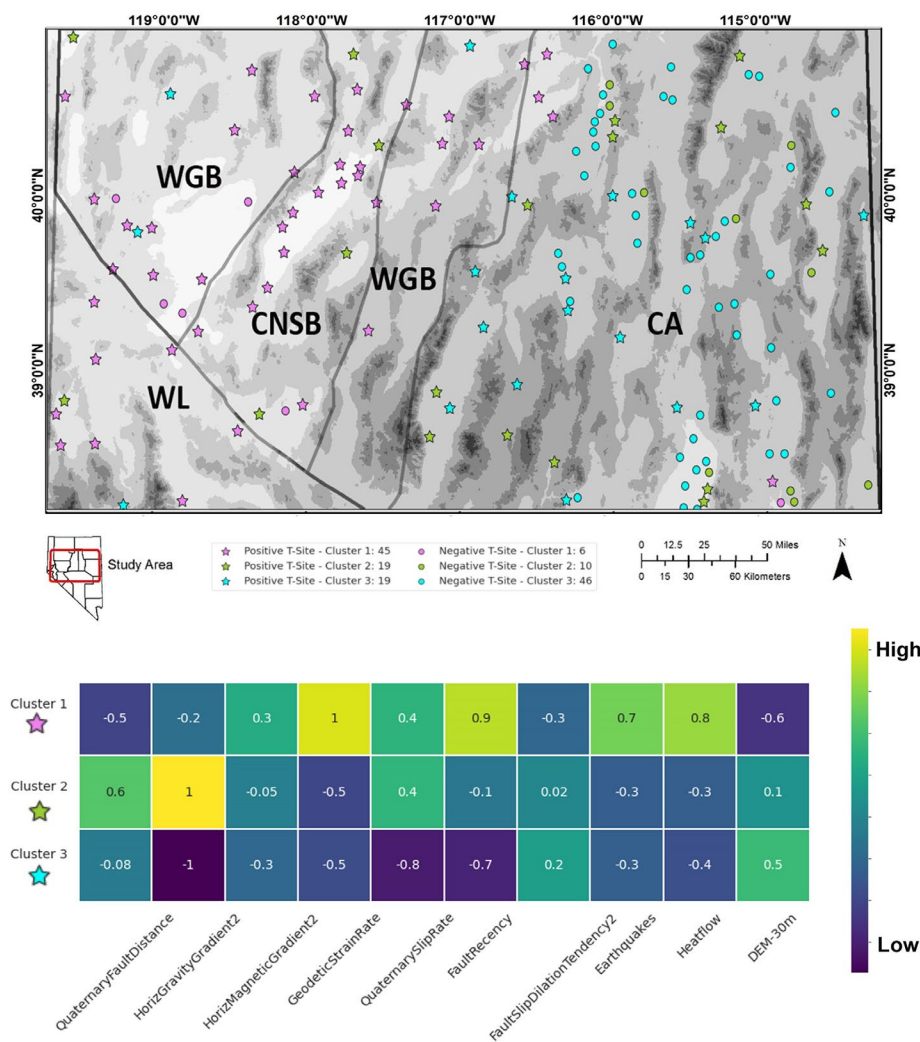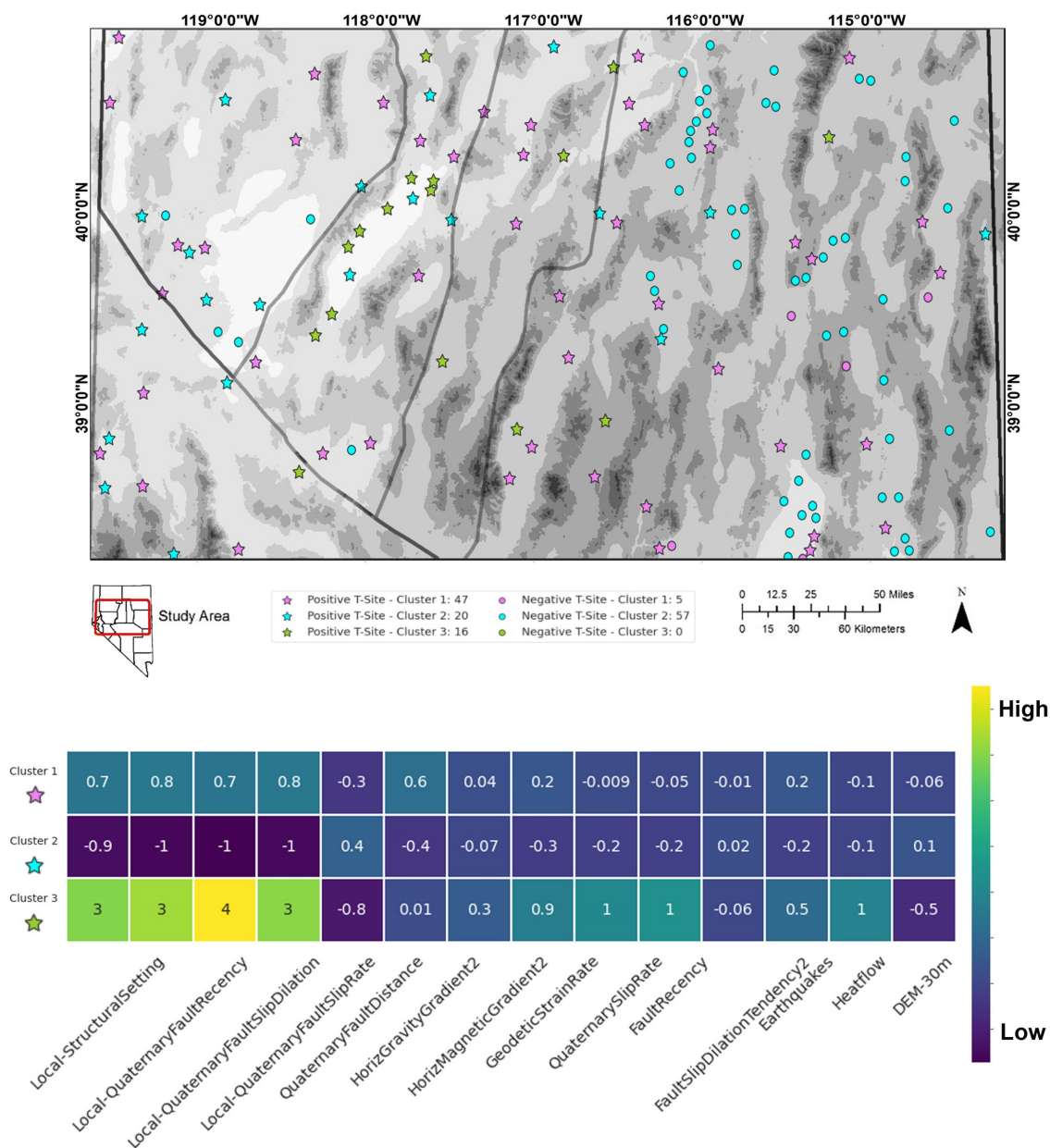
Figure A12. *Feature set two training site PCAk cluster map of the study area and PCAk feature score matrix (the sum of loadings at the center point of each cluster for PC1-4) for three cluster groups. The PCAk feature matrix is used to reference the influence of each feature in the spatial distribution for each cluster group. Acronyms for the labeled domains in the cluster map include: WGB = western Great Basin, WL = Walker Lane, CNSB = central Nevada seismic belt, CA = carbonate aquifer.*

Supervised Feature Sensitivity Analysis

This section includes example sensitivity analysis results incorporated into the BNN

modeling with feature set one from a permutation filter analysis (e.g., Pedregosa, 2011)

of training and test data. This method illustrates feature importance with respect to

predicting positive and negative training sites (Figure A13). Sensitivity analysis identifies

which input parameters are important for the prediction of the output variable and also

quantifies how the changes in the values of the input variables alter the value of the

output variable. Permutation filter analysis is applied during a single training and testing

stage of the variational BNN analysis using the inventory of positive and negative

training sites split into training (70%) and testing (30%) sets. The permutation filter

analysis allows for an internal calculation in which the difference in accuracy is

calculated, which is a consequence of not using each of the features.

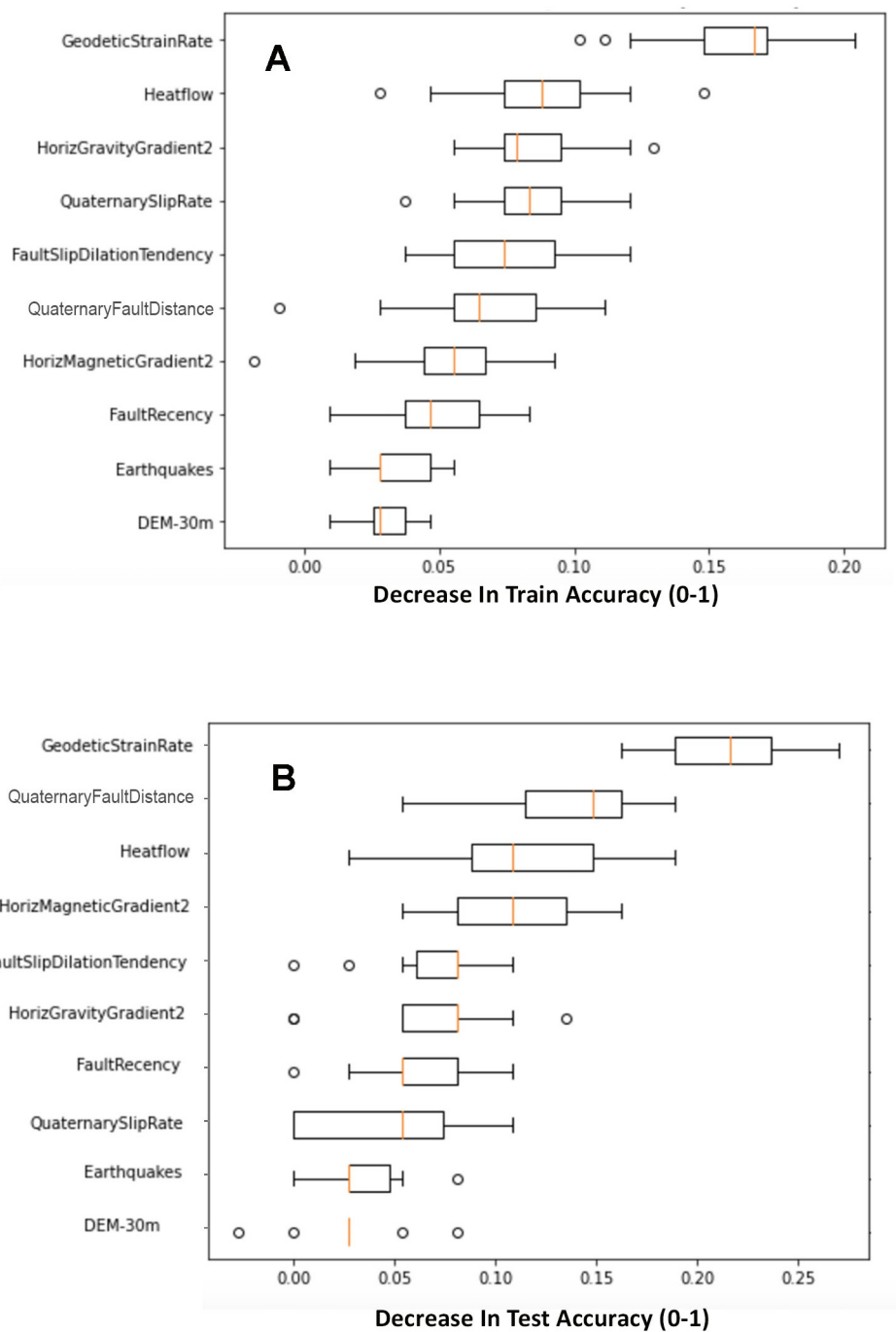***Figure A13.*** *Boxplots of permutation importance scores for training (A) and test data (B) with feature set one based on variational BNN analysis. Scores represent feature influence on model performance if dropped out during training/testing. Orange line*

represents mean value, the box bounds represent the mean value +/- standard error, and whisker bounds represent the mean value +/- standard deviation. Dots represent outlier sample values.

Both the training and test experiments indicate that geodetic strain and heatflow are principal features in dictating model performance. Additionally, Quaternary fault distance appears to be a key feature in the test set, which may indicate that this feature is better suited in supporting the generalization power of the model in testing versus directly fitting the data in the training process. Conversely, we can also identify the features that are less relevant to the classification of positive and negative sites using machine learning, including the DEM-30m and earthquake feature maps. Because permutation importance does not reflect the intrinsic predictive value of a feature by itself, but rather how important the feature is for a particular model and task, it is difficult to interpret why these features may receive their relative rankings. Given the nature of these efforts, where these features are structured and representative of different geologic and geophysical characteristics, direct observations of how they relate or what significance they have in distinguishing positive and negative sites benefit greatly from the context provided by unsupervised exploratory analysis. Also, this method would benefit from evaluating the ensemble of BNN networks, rather than a single network, but these efforts are computationally expensive and beyond the scope of this study. In future efforts, another promising approach tied to the BNN technique is performing local sensitivity analysis, where a user can probe a specific grid point and not only identify the distribution of

posterior predictions, but also determine feature importance in controlling the results of

said distribution (S. Brown, personal communication, 2021).

References

Ayling, B., 2020, 35 years of geothermal power generation in Nevada, USA: A review of field development, generation, and production histories: Proceedings, 45th Stanford Geothermal Workshop on Geothermal Reservoir Engineering, SGP-TR-216, 3 p.

Bell, J.W., and Ramelli, A.R., 2007, Active faults and neotectonics at geothermal sites in the western Basin and Range: Preliminary results: Geothermal Resources Council Transactions, v. 31, p. 375-378.

Bell, J.W., and Ramelli, A.R., 2009, Active fault controls at high-temperature geothermal sites: Prospecting for new faults: Geothermal Resources Council Transactions, v. 33, p. 425–429.

Benesty J, Chen J, Huang Y, Cohen I., 2009, Pearson Correlation Coefficient. In: Noise Reduction in Speech Processing: Springer Topics in Signal Processing, v. 2, p. 1-4.

Blackwell, D., Stepp, P., and Richards, M., 2010, Comparison and discussion of the 6 km temperature maps of the western US prepared by the SMU Geothermal Lab and the USGS: Geothermal Resources Council Transactions, v. 34, p. 515-519.

Blundell, C., Cornebise, J., Kavukcuoglu, K., Wierstra, D., 2015, Weight uncertainty in neural networks: Journal of Machine Learning Research Workshop Conference Proceedings, v. 37, p. 1613–1622.

Brooks, L.E., Masbruch, M.D., Sweetkind, D.S., and Buto, S.G., 2014, Steady-state numerical groundwater flow model of the Great Basin carbonate and alluvial aquifer system: U.S. Geological Survey Scientific Investigations Report, 86 p.

Brown, S., Coolbaugh, M., DeAngelo, J., Faulds, J., Fehler, M., Gu, C., Queen, J., Treitel, S., Smith, C., and Mlawsky, E., 2020, Machine learning for natural resource assessment, An application to the blind geothermal systems of Nevada: Geothermal Resources Council Transactions, v. 44, 14 p.

Caskey, S. J., Bell J. W., and Wesnousky S. G., 2004, Historic surface faulting and paleoseismicity in the area of the 1954 Rainbow Mountain–Stillwater earthquake sequence: Bulletin Seismological Society of America, v. 94, p. 1255–1275.

Coolbaugh, M.F., Taranik, J.V., Raines, G.L., Shevenell, L. A., Sawatzky, D.L., Minor, T.B., and Bedell, R., 2002, A geothermal GIS for Nevada: Defining regional controls and favorable exploration terrains for extensional geothermal systems: Geothermal Resource Council Transactions, v.26, p. 485-490.

Coolbaugh, M.F, and Shevenell, L., 2004, A method for estimating undiscovered geothermal resources in Nevada and the Great Basin: Geothermal Resources Council Transactions, v. 28, p. 13-18.

Coolbaugh, M., Zehner, R., Kreemer, C., Blackwell, D., and Oppliger, G., 2005, A map of geothermal potential for the Great Basin, U.S.A: Recognition of multiple geothermal environments: Geothermal Resources Council Transactions, v. 29, p. 223–228.

Coolbaugh, M.F., Raines, G.L., Zehner, R.E., Shevenell, L., and Williams, C.F., 2006, Prediction and discovery of new geothermal resources in the Great Basin: Multiple evidence of a large undiscovered resource base: Geothermal Resources Council Transactions, v. 30, 8 p.

Coolbaugh, M. F., Raines, G. L., and Zehner, R. E., 2007, Assessment of exploration bias in data-driven predictive models and the estimation of undiscovered resources: Natural Resources Research, v. 16, p. 199–207.

Coolbaugh, M., Lechler, P., Sladek, C., and Kratt, C., 2009, Carbonate tufa columns as exploration guides for geothermal systems in the Great Basin: Geothermal Resources Council Transactions, v. 33, p. 461–466.

Coolbaugh, M., Sladek, C., Zehner, R., and Kratt, C., 2014, Shallow temperature surveys for geothermal exploration in the Great Basin, USA, and estimation of shallow aquifer heat loss: Geothermal Resources Council Transactions, v. 38, p. 115-122.

Chollet, F., et al., 2015, Keras: Github Repository, https://github.com/fchollet/keras

Cracknell, M. J., and Reading, A. M., 2014, Geological mapping using remote sensing data: A comparison of five machine learning algorithms, their response to variations in the spatial distribution of training data and the use of explicit spatial information: Computers and Geosciences, v. 63, p. 22-33.

Craig, J.W., 2018, Discovery and analysis of a blind geothermal system in southeastern Gabbs Valley, western Nevada [M.S. Thesis]: University of Nevada, Reno, 111 p.

Curewitz, D. and Karson, J.A., 1997, Structural settings of hydrothermal outflow: Fracture permeability maintained by fault propagation and interaction: Journal of Volcanology and Geothermal Research, v. 79, p. 149-168.

Davis J, and Goadrich M., 2006, The relationship between Precision-Recall and ROC curves: Proceedings of the 23rd international conference on machine learning, p. 233–240.

Dixon, T.H., Miller, M., Farina, F., Wang, H., and Johnson, D., 2000, Present-day motion of the Sierra Nevada block and some tectonic implications for the Basin and Range province, North American Cordillera: Tectonics, v. 19, p. 1-24.

Dixon, T.H., Robaudo, S., Lee, J., and Reheis, M.C., 1995, Constraints on present-day Basin and Range deformation from space geodesy: Tectonics, v. 14, p. 755-772.

Doust, H., 2010, The exploration play: What do we mean by it? : American Association of Petroleum Geologists Bulletin, v. 94, p. 1657-1672.

Everitt B.S., Landau S., Leese M., Stahl D., 2011, Cluster Analysis: John Wiley & Sons, Limited Company, 348 p.

Faulds, J.E., Coolbaugh, M.F., Vice, G.S., and Edwards, M.L., 2006, Characterizing structural controls of geothermal fields in the northwestern Great Basin: A progress report: Geothermal Resources Council Transactions, v. 30, p. 69-76.

Faulds, J.E., and Henry, C.D., 2008, Tectonic influences on the spatial and temporal evolution of the Walker Lane: An incipient transform fault along the evolving Pacific – North American plate boundary: Spencer, J.E., and Titley, S.R., eds., Circum-Pacific Tectonics, Geologic Evolution, and Ore Deposits: Arizona Geological Society, Digest 22, p. 437-470.

Faulds, J.E., and Hinz, N.H., 2015, Favorable tectonic and structural settings of geothermal settings in the Great Basin region, western USA: Proxies for discovering blind geothermal systems: Proceedings, World Geothermal Congress, Melbourne, Australia, 6 p.

Faulds, J.E., Hinz, N.H., Coolbaugh, M.F., Shevenell, L.A., Siler, D.L., dePolo, C.M., Hammond, W.C., Kreemer, C., Oppliger, G., Wannamaker, P., Queen, J.H., and Visser, C., 2015a, Integrated geologic and geophysical approach for establishing geothermal play fairways and discovering blind geothermal systems in the Great Basin region, western USA: Final submitted report to the Department of Energy (DE-EE0006731), 106 p.

Faulds, J.E., Hinz, N.H., Coolbaugh, M.F., Shevenell, L.A., Siler, D.L., dePolo, C.M., Hammond, W.C., Kreemer, C., Oppliger, G., Wannamaker, P.E., Queen, J.H., and Visser, C.F., 2015b, Integrated geologic and geophysical approach for establishing geothermal play fairways and discovering blind geothermal systems in the Great Basin region, western USA: A progress report: Geothermal Resources Council Transactions, v. 39, p. 691-700.

Faulds, J.E., Hinz, N.H., Coolbaugh, M.F., Shevenell, L.A., Sadowski, A.J., Shevenell, L.A., McConville, E., Craig, J., Sladek, C., and Siler D.L., 2017, Progress report on the Nevada play fairway project, Integrated geological, geochemical, and geophysical analyses of possible new geothermal systems in the Great Basin region: Proceedings, 42nd Workshop on Geothermal Reservoir Engineering, Stanford University, Stanford, California, SGP-TR-212, 11 p.

Faulds, J.E., Craig, J.W., Coolbaugh, M.F., Hinz, N.H., Glen, J.M., Deoreo, S., 2018, Searching for blind geothermal systems utilizing play fairway analysis, western Nevada: Geothermal Resources Council Bulletin, v. 47, p. 34-42.

Faulds, J.E., Hinz, N.H., Coolbaugh, M.F., Ramelli, A., Glen, J.M, Ayling, B.A., Wannamaker, P.E., Deoreo, S.B., Siler, D.L., and Craig, J.W., 2019, Vectoring into potential blind geothermal systems in the Granite Springs Valley area, western Nevada: Application of the play fairway analysis at multiple scales: Proceedings 44th Workshop on Geothermal Reservoir Engineering, Stanford University, Stanford, California, SGP-TR-214, p. 74-84.

Faulds, J.E., Brown, S. Coolbaugh, M., DeAngelo, J., Queen, J.H., Treitel, S., Fehler, M., Mlawsky, E., Glen, J.M., Lindsey, C., Burns, E., Smith, C.M., Gu, C., and Ayling, B.F., 2020a, preliminary report on applications of machine learning techniques to the Nevada geothermal play fairway analysis: proceedings, 45th Workshop on Geothermal Reservoir Engineering, Stanford University, SGP-TR-216, 6 p.

Faulds, J.E., Sadowski, A.J., Coolbaugh, M., Siler, D.L., 2020b, Geothermal play fairway analysis of the Sou Hills, northern Nevada: A major Quaternary accommodation zone in the Great Basin region: Geothermal Resources Council, v. 44, 15 p.

Forson, C., Czajkowski, J. L., Norman, D. K., Swyer, M. W., Cladouhos, T.T. and Davatzes N., 2016, Summary of phase 1 and plans for phase 2 of the Washington state geothermal play fairway analysis: Geothermal Resources Council Transactions, v. 40, p. 541-550.

Goodfellow, I., Bengio, Y., and Courville, A., 2018, Deep Learning: MIT Press, e-book, http://www.deeplearningbook.org, p. 96-116.

Granek, J., 2016, Application of Machine Learning Algorithms to Mineral Prospectively Mapping [Ph.D.Thesis]: University of British Columbia, p. 40-62.

Heinz, N.H., Faulds, J.E., Coolbaugh, M.F., Hardwick, C., Gwynn, M., Queen, J., Ayling, B., 2020, Play fairway analysis of Steptoe Valley, Nevada: Integrating geology,

geochemistry, geophysics, and heatflow modeling in the search for blind resources: Geothermal Resources Council, v. 44, 20 p.

Hartigan, J.A., Wong, M.A., 1979, A K-means clustering algorithm: Applied Statistics, v. 28, p.100-108.

Hastie, T., Tibshirani, R., Friedman, J., 2001, The elements of statistical learning: Springer New York Inc., p. 485-586.

Heilweil, V.M., and Brooks, L.E., 2011, Conceptual model of the Great Basin carbonate and alluvial aquifer system: U.S. Geological Survey Scientific Investigations Report 2010-5193, 191 p.

Hess, R.H., Henson, M.A., Davis, D.A., Limerick, S.H., Siewe, S.S., and Niles, M., 2011, Oil and gas well information for Nevada, 2011, update: Nevada Bureau of Mines and Geology Open-File Report, p. 11-16.

Jolie, E., Samuel, S., Faulds, J.E., Chambefort, I., Axelsso, G., Gutiérrez-Negrín, L., Regenspurg, S., Ziegler, M., Ayling, B., Richter, A., Zemedkun, M., 2021, Geological controls on geothermal resources for power generation: Nature Reviews Earth and Environment, v. 2 p. 1-16.

Karpatne, A., Watkins, W., Read, J. S., & Kumar, V., 2017, Physics-guided neural networks (PGNN): An application in lake temperature modeling: ArXiv Preprint ArXiv:1710.11431, 11 p.

Koenig, J.B. and McNitt, J.R., 1983, Controls on the location and intensity of magmatic and non-magmatic geothermal systems in the Basin and Range province. The role of heat in the development of energy and mineral resources in the northern Basin and Range province: Geothermal Resources Council, v. 13, p. 93.

Lautze, N., Thomas, D., Hinz, N., Apuzen-Ito, G., Frazer, N., and Waller, D., 2017, Play fairway analysis of geothermal resources across the State of Hawaii: Geothermics, v. 70, p. 376-392.

Lee, D., and Seung, H., 1999, Learning the parts of objects by non-negative matrix factorization: Nature v. 401, p. 775-788.

Martín A., Agarwal and A., Barham, P., 2015, TensorFlow: Large-scale machine learning on heterogeneous systems: tensorflow.org.

McConville, E.G., Faulds, J.E., Hinz, N.H., Ramelli, A.R., Coolbaugh, M.F., Shevenell, L., Siler, D.L., and Bourdeau-Hernikl, J., 2017, A play fairway approach to geothermal exploration in Crescent Valley, Nevada: Geothermal Resources Council Transactions, v. 41, p. 1213-1221.

Mitchell, T.M., 1997, Machine Learning: McGraw-Hill Series in Computer Science, 414 p.

Nordquist, J., and Delwiche, B., 2013, The McGinness Hills geothermal project: Geothermal Resources Council Transactions, v. 37, 8 p.

Nurindrawati, F., Sun, J., 2019, Estimating total magnetization directions using convolutional neural networks: Society of Exploration Geophysicists International Exposition and 89th Annual Meeting, p. 2163- 2167.

Paszke, A., Gross.S., and Chintala, S., 2019, PyTorch: An imperative style, high-performance Deep Learning Library: Advances in Neural Information Processing Systems 32, p. 8024–8035.

Pedregosa, C., 2011, Scikit-learn: Machine Learning in Python: Journal of Machine Learning Research, v. 12, p. 2825-2830.

Pepin, J. D., 2019, New approaches and insights to geothermal resource exploration and characterization, [Ph.D. Dissertation]: New Mexico Institute of Mining and Technology, Socorro, New Mexico, 186 p.

Perol, T., Gharbi, M., and Denolle, M., 2018, Convolutional neural network for earthquake detection and location: Science Advances, v.4, no.2, 12 p.

Richards, M., and Blackwell, D., 2002, A difficult search, Why Basin and Range systems are hard to find: Geothermal Resources Council Bulletin, v. 31, p. 143-146.

Rodriguez-Galiano, V., Sanchez-Castillo, M., Chica-Olmo, M., and Chica-Rivas, M., 2015, Machine learning predictive models for mineral perspectivity- an evaluation of neural networks, random forest, regression trees and support vector machines: Ore Geology Reviews, v. 71, p. 804– 818.

Rowland, J.V., and Sibson, R.H., 2004, Structural controls on hydrothermal flow in a segmented rift system, Taupo Volcanic Zone, New Zealand: Geofluids v.4, p. 259–283.

Sadowski, J.A. 2015, Structural controls of the Black Warrior blind geothermal system, northwestern Nevada, USA: Geothermal Resources Council Transactions, v. 36, p. 897-902.

Shervais, J.S., Glen, J.M., Nielson, D., Garg, S., Dobson, P., Gasperikova, E., Sonnenthal, E., Visser, C., Liberty, L.M., DeAngelo, J., Siler, D., Varriale, J., and Evans, J.P., 2016, Geothermal play fairway analysis of the Snake River Plain Phase 1: Proceedings, 41st Workshop on Geothermal Reservoir Engineering, Stanford University, SGP-TR-209, 7 p.

Siler, D.L., Zhang, Y., Spycher, NF., Dobson, P.F., McClain, J.S., and Gasperikova, E., 2017, Play-fairway analysis for geothermal resources and exploration risk in the Modoc Plateau region: Geothermics, v. 69, p. 15-33.

Siler, D.L. Pepin, J.D., 2021,3-D Geologic controls of hydrothermal fluid flow at Brady geothermal field, Nevada, USA: Geothermics, v. 94, 13 p.

Smith, C.M., Faulds, J.E., Brown, S., Coolbaugh, M., Lindsey, C., Treitel, S., Ayling, B., Fehler, M., Gu, C., Mlawsky, E., 2021, Characterizing signatures of geothermal exploration data with machine learning techniques: An application to the Nevada

play fairway analysis: Proceedings: 46th Workshop on Geothermal Reservoir Engineering, Stanford University, SGP-TR-218, 13 p.

Stewart, J.H., 1998, Tectonics of the Walker Lane belt, western Great Basin: Mesozoic and Cenozoic deformation in a zone of shear: in Ernst, W. G., ed., Metamorphism and crustal evolution of the western United States, Prentice Hall, Englewood Cliffs, New Jersey, p. 681-713.

van der Maaten, L.J.P., Hinton, G.E., 2008, Visualizing high-dimensional data using t-SNE: Journal of Machine Learning Research v.9, p. 2579-2605.

Vesselinov, V.V., Mudunuru, M.K., Ahmmed, B., Karra, S., and Middleton, R.S., 2020, Discovering signatures of hidden geothermal resources based on unsupervised learning: 45th Workshop on Geothermal Reservoir Engineering, Stanford University, Stanford, SGR-TR-216, 11 p.

Wannamaker. P.E., Moore, J.N., Pankow, K.L., Simmons, S.F., Nash, G.D., Maris, V., Trow, A., and Hardwick, C.L., 2017, Phase II of play fairway analysis for the eastern Great Basin extensional regime, Utah: Status of indications: Geothermal Resources Council Transactions, v. 41, p. 2368-2382.

Williams, C.F., Reed, M.J., DeAngelo, J., and Galanis, S.P. Jr., 2009, Quantifying the undiscovered geothermal resources of the United States: Geothermal Resources Council Transactions, v. 33, p. 995-1002.

Wold, S., Esbensen, K., and Geladi, P., 1987, Principal component analysis: Chemometrics and intelligent laboratory systems, v. 2 p. 37–52.